

**A sub-GeV charged-current quasi-elastic  
 $\nu_\mu$  cross-section on carbon at SciBooNE**

Joseph James Walding

High Energy Physics  
Blackett Laboratory  
Imperial College London  
London, UK

A thesis submitted for the degree of  
Doctor of Philosophy  
of the University of London  
and the Diploma of Imperial College.

December 2009

Dedicated to my parents.

# Declaration

Throughout this thesis where the work of others is presented references to the originating work are shown. Where my own work has been published references are also listed for completeness. The areas of my thesis that are my own work are given below.

I was involved in the construction of the Muon Range Detector, the prototype construction and testing presented in section 4.3.1 was done by myself in May and June 2006. All studies presented in chapter 7 and methods developed there were done by myself including the construction of the stopped cosmic Monte-Carlo.

All analysis methods presented in Chapter 8 excluding the Muon Confidence Level were developed by myself. The minimisation method using MINUIT presented in chapter 9 was modified from the code developed by Jose Alcaraz-Union from University de Barcelona.

## Abstract

Neutrino-nucleus charged-current quasi-elastic scattering is the signal interaction used by many neutrino oscillation experiments. For muon disappearance studies the signal mode is  $\nu_\mu n \rightarrow \mu p$ . Modern oscillation experiments, such as T2K, produce neutrino beams with peak beam energies of order a few-GeV. It is therefore vitally important to have accurate measurements of the charged-current quasi-elastic cross-section for future neutrino oscillation experiments. Neutrino-nucleus cross-sections in the few-GeV region are not well understood, with the main uncertainties coming from understanding of the neutrino beam flux and the final state interactions within nuclei.

SciBooNE is a sub-GeV neutrino-nucleus cross-section experiment based at Fermilab, Batavia, USA, with the goal to measure neutrino cross-sections with precision of order 5%. SciBooNE took data from June 2007 until August 2008, in total  $0.99 \times 10^{20}$  and  $1.53 \times 10^{20}$  protons on target were collected in neutrino and anti-neutrino mode, respectively.

In this thesis a  $\nu_\mu$  charged-current quasi-elastic (CCQE) cross-section contained within the SciBar sub-detector is presented. A method to tag muons in SciBar was developed and three samples were isolated. An excess in backwards tracks in the one-track sample is observed. A Poisson maximum likelihood is used to extract the CCQE cross-section. The fit was applied using a basic fit parameter model, successfully used to obtain the cross-section in the SciBar-MRD matched CCQE analysis. This method was found to be insufficient in describing the data for the SciBar-contained CCQE analysis. By adding two migration parameters the cross-section was calculated to be  $1.004 \pm 0.031$  (stat) $_{-0.150}^{+0.101}$ (sys)  $\times 10^{-38}$  cm<sup>2</sup>/neutron, excluding backwards tracks with a  $\chi^2 = 203.8/76$  d.o.f. and  $1.083 \pm 0.030$ (stat) $_{-0.177}^{+0.115}$ (sys)  $\times 10^{-38}$  cm<sup>2</sup>/neutron, including backwards tracks with a  $\chi^2 = 659.8/133$  d.o.f. Only neutrino beam and detector systematics have been considered.

Further study of the SciBar-contained sample is suggested, introducing additional fit parameters and considering the remaining systematics. The end goal is to extract a SciBooNE CCQE cross-section using the SciBar-contained and SciBar-MRD matched samples.

---

## Acknowledgements

There are a great number of people I would like to thank, without whom I wouldn't have completed this thesis. Firstly, I would like to thank my supervisor Dr. Morgan Wascko. In the summer of my first year I was offered the possibility of working on a four week hardware project based at Fermilab for Imperial College's new T2K staff member. This project would entail the construction and testing of some muon range detector scintillator paddles for the SciBooNE experiment. At the time this was seen as a good opportunity for me to get some hardware experience before sinking my teeth into years of MC simulations and studies. I had only been a T2K collaborator for a few months and had yet to really achieve anything productive for the collaboration. After learning the joys of epoxy, finding light-leaks using the always reliable electric shock method, and sitting for days in front of a test-stand taking cosmic data, I knew that I wanted to work on SciBooNE full-time! It is amazing now to look back and realise that I was able to work on an experiment from conception, through the entire data run and to complete an analysis all within the time-frame of my Ph.D. I think this is a rare opportunity in particle physics today and one that I feel very fortunate to have had. For this, and for all the conversations, ideas, guidance and support I am truly grateful to Morgan, I owe you a great many beers. However, you are very wrong about the greatest Bond movie of all time; it is, 'The Spy Who Loved Me' and that's the end of it!

I would also like to thank my Imperial T2K colleagues. Dr. Yoshi Uchida and Professor Dave Wark, who persuaded me to join T2K in the first place, enticing me with neutrino oscillations and Kobe beef; not a bad combination! I'm sorry you lost me to the dark side of neutrino cross-sections! I will remember Dave offering to get me an extension on my transfer report a few hours before the deadline so that I could accompany him to Lords; it's good to have friends in high places! I will remember Yoshi.... actually it's best I don't open myself up to libel. What I will say is all incidents with Yoshi contained at least one if not all of the following: Beer, Eagles songs (not the band), karaoke and chicken sashimi! I owe a great deal to Professor Peter Dornan, my personal tutor whilst an undergraduate at Imperial, who inexplicably let me join the HEP Ph.D program! It was a real honour to be invited to your 70<sup>th</sup> Birthday. Thank you for all your guidance and advice over the last eight years.

Dr. Antonin Vacheret and Dr. Matthew Malek; your advice, especially during the final weeks of writing, was invaluable and your broad physics knowledge is something

---

---

I aspire to attain. It was a pleasure to work with you both. If I am half as good a post-doc I will be more than satisfied. Ian Taylor was my predecessor on T2K, he taught me the beauty of Linux and spent countless hours explaining the T2K framework to me only for me to join SciBooNE! Ian, in your acknowledgements you say, “I would also like to thank Joe Walding, for taking time out of his own studies to help me with mine; I hope that he found it equally beneficial.” I think we both know you spent far more time explaining things to me than I ever did for you. I certainly found this arrangement beneficial! In seriousness, I learnt a great deal and I owe you a huge debt of gratitude. To Francois, Jim, Pavel, Patrick, Sarah and Gil thank you for putting up with my invasion of your office space during the final months and good luck with your analyses. I recommend not writing up in six weeks!

I would like to thank my SciBooNE collaborators: The co-spokespersons, Professor Tsuyoshi Nakaya and Morgan, thank you for leading the experiment, for organising two fantastic overseas collaboration meetings, and, most importantly, preparing two superb pub-crawls! Dr. Michel Sorel, Dr. Hide Tanaka and Dr. Masashi Yokoyama; it was a real pleasure to work with you guys and I know that I am a better physicist for it.

I worked on the Muon Range Detector closely with Dr. Rob Napora and Yasuhiro ‘Nakaji’ Nakajima. Rob, thank you for leading the MRD construction, I think we did a good job!<sup>1</sup> Also thank you for the Box-o-Joe’s and donuts on the Saturday morning install shifts followed by many a card discussion. I am excited that we will be working together on Minerva. Nakaji: You rock! I think that is all I need say, from the endless help with physics and code, to the extraordinary feats of eating, it was awesome to share an office with you. Thank you also to my fellow SciBooNE grad students: Katsuki ‘Bancho’ Hiraide, Yoshi Kurimoto, Hide Takei, Jose Alcaraz, Joan Catala, Kendall Mahn, Aaron Hanson, Gary Cheng and of course Teppei Katori for all the help and advice, not forgetting the SciBooNE social-clubs. Two Brothers wont be the same without you guys.

I would also like to thank Dr. Sam Zeller, Professor Rex Tayloe, Dr. Steve Brice and Professor Lucio Ludovici for their feedback and ideas concerning this anaylsis. If it weren’t for your questions, suggestions and discussions this thesis would be a whole lot poorer.

---

<sup>1</sup>notice how my analysis is on a SciBar-contained sample!

---

Joey, you were always there for me and you put up with my stubbornness, I know that I would not have achieved this if it hadn't been for you. I had an amazing three years living in Chicago working on SciBooNE, and that was largely because of you.

Thank you Chivas for feeding me for three years. The Users Center is the best bar in Chicagoland!

Thank you to my flat-mates; Boydie, Lisa, Nick and Sarah who put up with the mess in my office (their kitchen). It was an awesome time living with you guys, shame that I spent most of it in an analysis-finishing/thesis-writing cocoon. Thank you for offering me so many different ways to procrastinate.... Fabio! Rob and Eva, thank you for contributing to my procrastination; I am that little bit saner because of it, though you might both disagree. Thank you to all my friends especially John, Lance, Netia and Sonia, you guys deserve more than a sentence but you know what you mean to me.

Finally I would like to thank my family; my brother and sister who are awesome, and my parents; I could not have achieved this without your support and I don't have the words to fully describe my gratitude but to say thank you.

---

# Contents

<b>Declaration</b>	<b>2</b>
<b>Abstract</b>	<b>1</b>
<b>Acknowledgements</b>	<b>1</b>
<b>Contents</b>	<b>4</b>
<b>List of Figures</b>	<b>9</b>
<b>List of Tables</b>	<b>20</b>
<b>Chapter 1. Introduction</b>	<b>23</b>
1.1 A History of the Neutrino	24
1.1.1 Prediction	24
1.1.2 Observation	25
1.2 Neutrino Physics and the Standard Model	26
1.2.1 Neutrinos in the Standard Model	26
1.2.2 Neutrino Oscillations	28
1.2.3 Neutrino-Nucleus Interactions	32

---

---

<b>Contents</b>	<b>5</b>
<b>Chapter 2. The SciBooNE Experiment</b>	<b>40</b>
2.1 Motivation for the SciBooNE Experiment	41
2.1.1 Precise Neutrino Cross-Section Measurements	41
2.1.2 Anti-Neutrino Cross-section Measurements	42
2.1.3 Oscillation Searches	42
2.2 SciBooNE Timeline	43
<b>Chapter 3. The Booster Neutrino Beam</b>	<b>45</b>
3.1 The Booster	45
3.2 The Magnetic Focusing Horn and Beam Target	47
3.3 The Decay Volume	48
<b>Chapter 4. The SciBooNE Detector</b>	<b>49</b>
4.1 Scintillator Bar Detector (SciBar)	49
4.1.1 Scintillator Bars	51
4.1.2 Wavelength-Shifting Fibres	53
4.1.3 Multi-Anode Photo-Multiplier Tubes	55
4.1.4 Readout Electronics	55
4.1.5 Gain Monitoring	56
4.1.6 Energy Calibration	56
4.2 The Electron-Catcher	57
4.3 The Muon Range Detector	58
4.3.1 Scintillator Paddle Prototype: Construction and Testing	61
4.4 Data Acquisition	64

---

---

<b>Contents</b>	<b>6</b>
<b>Chapter 5. Simulation</b>	<b>66</b>
5.1 Beam Simulation	66
5.1.1 Meson Production Simulation	66
5.1.2 Meson Decay Simulation	68
5.1.3 Neutrino Flux Prediction	68
5.1.4 Beam Flux Systematic Uncertainties	69
5.2 Neutrino-Nucleus Interactions	71
5.2.1 Quasi-Elastic Scattering	73
5.2.2 Single Meson Production	74
5.2.3 Coherent Pion Production	75
5.2.4 Intra-Nuclear Interactions	75
5.2.5 Pion Interactions and Nucleon Rescattering	76
5.3 Detector Simulation	77
5.3.1 Particle Simulation in the Detectors	77
5.3.2 Detector Response	77
5.3.3 Dirt and EC-MRD Interaction Simulations	78
<b>Chapter 6. The Data Summary</b>	<b>81</b>
6.1 Data Quality Cuts	81
6.1.1 Beam	81
6.1.2 Detector	83
6.2 Data Summary	83

---

---

<b>Contents</b>	<b>7</b>
<b>Chapter 7. Muon Tagging</b>	<b>88</b>
7.1 Muon Tagging Methods	88
7.1.1 Muon Double-Coincidence Method (MDC)	88
7.1.2 Method Limitations	92
7.1.3 The Michel Temporal Tag (MTT)	94
7.2 Muon Tagging Performance Studies	95
7.2.1 Cuts and Filters	95
7.2.2 Monte-Carlo Studies	96
7.3 Two Single Coincidences Method (TSC)	102
7.4 Stopped Cosmic Ray Data and Monte-Carlo Studies	103
7.5 Summary	109
<b>Chapter 8. CCQE Event Selection</b>	<b>111</b>
8.1 Analysis Overview	111
8.2 Event Selection	113
8.2.1 Event Classification	127
8.2.2 Event Selection Summary	139
8.3 Backwards Track Anomaly	142
<b>Chapter 9. CCQE Cross Section Measurement</b>	<b>144</b>
9.1 Cross-Section Extraction	144
9.1.1 Cross-Section Extraction Overview	144
9.1.2 Poisson Maximum Likelihood	144

---

---

<b>Contents</b>	<b>8</b>
9.2 Systematic Uncertainties	148
9.2.1 Detector Effects	148
9.2.2 Neutrino Beam	149
9.2.3 Nuclear Effects	150
9.2.4 Neutrino Interaction Models	150
9.3 Results	150
9.3.1 Introducing Additional Fit Parameters	154
<b>Chapter 10. Conclusions</b>	<b>159</b>
10.1 Summary	159
10.2 Future Prospects	161
<b>Appendix A. Calculations</b>	<b>163</b>
A.1 Neutrino Kinematics	163
A.1.1 Neutrino Energy Calculation	163
A.1.2 $Q^2$ Calculation	165
A.2 Poisson Maximum Likelihood Derivation	166
<b>References</b>	<b>167</b>

---

---

# List of Figures

- 1.1 The twelve fermions and four bosons of the Standard Model. The fermions are separated into three generations of leptons and quarks. The leptons interact via the Weak force with the charged leptons also interacting via the electromagnetic force. The quarks interact via all three forces. Of the four bosons, the photon propagates the electromagnetic force, the gluon the Strong force and the  $Z^0$  and  $W^\pm$  the Weak force. 27
- 1.2 The Pion Decay Feynman Diagram 28
- 1.3 Current allowed and excluded regions in  $\tan^2 \theta - \Delta m^2$  space 33
- 1.4 Types of Charged Current Neutrino Interactions 34
- 1.5 Expected T2K Neutrino Energy Reconstruction 35
- 1.6 Size in the measurement errors of the oscillation parameters,  $\sin^2 \theta_{23}$  and  $\Delta m_{23}^2$  as a function of true  $\Delta m_{23}^2$  for a systematic error on the non-QE/CCQE cross-section ratio of 5% (red dashed), and 20% (blue dotted). The solid line shows the expected statistical error. 36
- 1.7 Charged-Current Muon Neutrino Cross-Sections with Selected Experimental Data 37
- 1.8 Types of Neutral Current Neutrino Interactions 39
- 2.1 Schematic of Booster Neutrino Beamline. The SciBooNE and Mini-BooNE detectors are also pictured. 41
-

- 
- 2.2 Comparison of the proposed off-axis T2K neutrino beam flux (blue) with the Booster neutrino beam flux (red) and the K2K beam flux (pink). The K2K neutrino beam has a higher peak beam flux than T2K. Consequently cross-section measurements made by K2K are in a different energy region to T2K. All curves are normalised to unit area. 42
- 3.1 An aerial view of the Booster Neutrino Beamline. The red line plots the route of the protons from the Booster and where they are syphoned into the Neutrino Beam Target Hall (green box). The yellow box represents the decay volume beyond the target and the blue box shows the location of the SciBooNE detector hall (not shown). MiniBooNE is located 440 m further down stream from SciBooNE. 46
- 4.1 SciBooNE Detector Schematic 50
- 4.2 A schematic of the SciBar detector. SciBar consists of 14,336 extruded scintillator bars readout by 224 multi-anode photo-multiplier tubes. Each photo-multiplier tube reads out an  $8 \times 8$  array of channels in either the horizontal or vertical view. 51
- 4.3 Typical scintillator bar emission spectrum. 53
- 4.4 Ratio of visible energy loss to expected energy loss as a function of expected  $\frac{dE}{dx}$ . Measured using a prototype SciBar detector at KEK. The red line shows the best fit to the data. 54
- 4.5 Absorption and emission spectra for a typical WLS fibre. 54
- 4.6 Cross-sectional schematic of a Scintillating bar and WLS fibre. 55
- 4.7 Schematic of the SciBar LED gain monitoring system. 56
- 4.8 (a) The LED intensity stability during the SciBooNE data run. The relative changes seen in the LED are corrected in the MA-PMT calibration.(b) A typical MA-PMT gain stability during the SciBooNE data run. 57
-

- 
- 4.9 A schematic of the EC detector. The EC is a ‘spaghetti’ calorimeter consisting of two layers, one vertical and one horizontal, of 32 modules. With a thickness of  $11X_0$  the EC is used to measure EM showers. 58
- 4.10 Cross-section schematic of EC module. 59
- 4.11 A schematic of the MRD detector. The MRD consists of 362 scintillator paddles arranged in thirteen alternating horizontal and vertical layers separated by 12, 2 inch thick, iron plates. The detector is able to range out muons with momenta less than 1.2 GeV/c. 60
- 4.12 Hit finding efficiency for a typical MRD half-plane using cosmic data. Both the individual counter and summed efficiencies are shown. The typical efficiency is around 99%. 61
- 4.13 Schematic of the cosmic test stand. 63
- 4.14 Plateau curves for two prototype counters (red and blue) determined using cosmic ray data. The red counter has a higher operating voltage. Both counters have hit-finding efficiencies above 99% once on the plateau. 63
- 4.15 Plateau curves for three positions on the prototype counter determined using cosmic ray data. The least efficient point on the counter is at 65 cm. Once the counter is on the plateau the position has no effect on the hit-finding efficiency. 64
- 5.1 Neutrino flux predictions at the SciBooNE detector as a function of neutrino energy,  $E_\nu$ , normalised per unit area, protons on target and neutrino energy bin width, in neutrino mode (left) and antineutrino mode (right). The spectra are averaged within 2.12 m from the beam centre. The total flux and contributions from individual neutrino flavours are shown. 69
- 5.2 (left) Systematic uncertainty in the neutrino energy distribution for muon neutrino interactions. (right) The fractional uncertainty as a function of neutrino energy. 70
-

5.3	NEUT simulated cross-sections normalised by neutrino energy for each interaction mode for $M_A = 1.2$ GeV.	72
5.4	Fate of charged pions from $\nu_\mu$ -carbon interactions inside the nucleus as simulated by NEUT. All pions simulated (black line), pion absorption (red line), inelastic scattering (blue line), charge exchange (green line).	76
5.5	Schematic of the simulated dirt region showing the top (top left), side (bottom left), and front (bottom right) views of the detector and the detector hall.	79
5.6	Interaction vertices for dirt events that produce a single track in SciBar. The solid line represents the detector hall walls, the dashed line represents the location of the SciBar detector.	80
6.1	Distributions of the beam quality variables for a typical SciBooNE run. a) The proton beam intensity, b) the toroid agreement, c) the peak horn current, d) the targeting efficiency, e) the GPS time difference between the beam and detector. The red lines represent the cut value required for a good spill.	85
6.2	The accumulated POT during the SciBooNE run. The vertical dashed lines correspond to horn polarity switches.	86
6.3	The charged-current candidate event rate stability in SciBar.	86
6.4	The charged-current candidate event rate stability in the MRD.	87
7.1	Time difference between views for all TDC hits (SciBooNE $\nu$ data). The coincidence cut is set at 20 ns.	89
7.2	ADC hits in a ‘typical’ event, the horizontal view is shown on the left and the vertical view is shown on the right. Red hits are the muon, green hits are the Michel electron and magenta hits are random noise hits in the event.	90

---

- 
- 7.3 The track reconstruction of the hits, showing mis-reconstruction of the muon track in both views. The muon stops in TDC block 2 in the horizontal view (left) and TDC block 8 in the vertical view (right). The muon track is mis-reconstructed into TDC block 5 in both views (yellow arrow). The blue arrow is the reconstructed Michel electron. 90
- 7.4 The TDC hits associated with the event schematic shown in figure 7.2. To find a double coincidence between two TDC blocks all combinations of TDC blocks are considered. Clearly TDC block 2 (horizontal) and TDC block 8 (vertical) have a double coincidence and so can successfully tag the event as containing a muon. 91
- 7.5 Energy deposited by all hits (SciBooNE  $\nu$  data). A 1 MeV cut is applied to remove noise hits. 92
- 7.6 A schematic of a SciBar TDC block and its surrounding neighbours. The TDC block corners are highlighted in purple, the edges in light blue, the internal cells in dark blue. The white blocks belong to neighbouring TDC blocks. For the ‘non-stopping’ view the Michel electron has a probability of not leaving a time hit in the same TDC block as the final muon hit. 93
- 7.7 GEANT4 display of 1000 isotropically distributed muons within SciBar. 96
- 7.8 Event display of a reconstructed one-track event that passed the Michel tagging method. The red dots represent ADC hits in SciBar; the dot size is proportional to the energy deposited. The green line represents the reconstructed track. 97
- 7.9 Event display of a reconstructed two-track event that failed the Michel tagging method. This is likely due to the muon stopping at the edge of a TDC block resulting in the ‘non-stopping’ view failure outlined in Method Limitations. The blue line represents the true muon track, the red line represents the true electron track. 98
-

- 
- 7.10 one-track sample reconstructed muon lifetime. A lifetime of  $2.093 \pm 0.045\mu s$  is calculated, in good agreement with experiment when accounting for muon capture. 98
- 7.11 Event display of a reconstructed one-track proton event that passed the Michel tagging method. The proton (pink track), interacts in the detector creating a pion (light blue track) which decays to an electron (red track). 99
- 7.12 Event display of a reconstructed one-track  $\pi^+$  event that passed the Michel tagging method. The  $\pi^+$  (light blue track) decays to a  $\mu^+$  (not visible due to very short track) which decays to an electron (red track). 100
- 7.13 one-track sample reconstructed muon lifetime. A lifetime of  $2.230 \pm 0.050\mu s$  is calculated.  $\pi^+$  decay to  $\mu^+$  which don't undergo capture, therefore the lifetime is higher than observed in the isotropic  $\mu^-$  sample. 101
- 7.14 Event display of a reconstructed one-track  $\pi^-$  decay event that passed the Michel tagging method. The  $\pi^-$  (light blue track) decays in flight to a  $\mu^-$  (dark blue track), which decays to an electron (red track). 102
- 7.15 Schematic showing the TDC information required to successfully tag a muon using the MDC method (left) and the TSC method (right). In the TSC schematic the muon stops in a vertical TDC block, in the horizontal view two TDC blocks are needed to tag the muon and the Michel electron. 103
- 7.16 A schematic showing a stopped cosmic-ray (left) and a through passing cosmic-ray (right). The blue rows represent the 4 TDC rows used for cosmic triggering. To trigger a stopped cosmic event one of the outer TDC rows must not trigger. 104
- 7.17 An event display of a cosmic ray stopping in the SciBar detector. The event was recorded during the special stopped cosmic data run. 104
-

- 
- 7.18 Stopped cosmic angular distributions in data and MC.  $\tan \theta_{xz}$ , (left) and  $\tan \theta_{yz}$  (right). The  $\tan \theta_{yz}$  is asymmetric due to the geometry of the detector hall. Positive  $\tan \theta_{yz}$  values correspond to cosmic rays entering SciBar from the downstream side of the detector hall. Negative  $\tan \theta_{yz}$  values correspond to cosmic rays entering SciBar from the upstream side of the detector hall. 107
- 7.19 An event display of a through passing cosmic ray which is reconstructed within the fiducial volume. 109
- 7.20 Left: The number of hits per event for the data (black line) and MC (red line) stopped cosmic samples. Right: The difference between the number of data and MC hits normalised to the total number of hits. Data events have a higher number of hits per event, due in part to through-passing cosmics. The MC is normalised to the number of data events. 110
- 8.1 Schematic of the nine TDC blocks surrounding the muon track (blue dashed box) and the proton track (pink dashed box). One decay electron can be matched to both tracks, this is a fake signal for a CC- $\pi$  event. As such SciBooNE is unable to distinguish CCQE and CC- $\pi$  events using timing information alone. 112
- 8.2 Typical event signatures for the four samples. (a-c) CCQE events, (d) CC- $\pi$  event (dominant background). 113
- 8.3 Difference between the true vertex and reconstructed vertex estimated with the MC simulation for (a) The  $x$  projection, (b) the  $y$  projection, (c) the  $z$  projection assuming an upstream vertex and (d) the  $z$  projection using track timing information. 116
- 8.4 Back-to-back track events can be mis-reconstructed as single track events. This can result in the reconstructed interaction vertex being upstream of the true interaction vertex. 117
-

- 
- 8.5 The reconstructed vertex distributions in SciBar for all three projections after the zero MRD tracks and 1<sup>st</sup> layer veto cuts. The MC is separated into two SciBar generated events (white histogram), and dirt generated events (hatched histogram). The MC is normalised to the SciBar-MRD matched sample. Dashed lines indicated the fiducial volume limits. 118
- 8.6 Event timing distribution of the SciBar-contained sample. Dashed lines indicated the 2  $\mu$ s beam window. 119
- 8.7 The SciBar-contained reconstructed vertex distributions in SciBar for all three projections after applying all pre-cuts. The MC is separated into two event types; SciBar generated events (white histogram), and dirt generated events (hatched histogram). The MC is normalised to the SciBar-MRD matched sample. Dashed lines indicated the fiducial volume limits. 121
- 8.8 Muon momentum (top left) and angular (top right) distributions in MC before (white histogram) and after (hatched histogram) the SciBar-contained sample selection. The selection efficiencies are also shown (bottom left and right). The selected sample contains muons with momentum up to 600 MeV, with a median momentum of  $\sim 250$  MeV. 122
- 8.9 Neutrino energy (top left) and momentum transfer (top right) distributions in MC before (white histogram) and after (hatched histogram) the SciBar-contained sample selection. The selection efficiencies are also shown (bottom left and right). The selected sample contains neutrinos with energies up to 1 GeV, with a median energy of 400 MeV. 122
- 8.10 The reconstructed muon lifetime using the muon tagging timing information. The lifetime is measured to be  $2.003 \pm 0.047^{stat}$   $\mu$ s, in good agreement with experimental data. 123
-

- 
- 8.11 Difference between, (a) the reconstructed and true muon momentum, (b) the reconstructed and true muon angle, with respect to the beam direction ( $z$  axis), estimated using the MC simulation. The hatched histogram shows the CCQE contribution, the white histogram shows the background contribution. 125
- 8.12 Difference between, (a) the reconstructed and true neutrino energy,  $E_\nu^{rec}$ , (b) the reconstructed and true momentum transfer,  $Q^2$ , estimated using the MC simulation. The hatched histogram shows the CCQE contribution, the white histogram shows the background contribution. 126
- 8.13 Schematic of the event classification. 127
- 8.14 The vertex separation for the two-track sample for data (data points) and MC (histogram). The dashed line represents the vertex separation cut. The MC is normalised to the SciBar-MRD matched sample. 128
- 8.15 Event display showing the Michel electron track in the same TDC block as the muon track in the top view (left). The Michel electron time will be mis-reconstructed to be identical to the muon time. 129
- 8.16 There are six possible event topologies for  $\mu+p$  and  $\mu+e$  events. Numbers 1 and 4 are  $\mu+p$  topologies, numbers 2,3,5 and 6 are  $\mu+e$  topologies. 130
- 8.17 (a) Expected  $dE/dx$  distribution for a cosmic ray muon. (b) The confidence level as a function of  $dE/dx$  observed in a scintillator plane. 131
- 8.18 (a) The MuCL distribution for different particle types for the one-track sample, estimated using the MC simulation. (b) The MuCL distribution for data and MC, the MC is separated into interaction types. Events with  $MuCL > 0.05$  are retained. 133
- 8.19 The MuCL distribution for different particle types for the proton candidate track in the two-track sample, estimated using the MC simulation. 133
-

- 
- 8.20 (a) The data and MC MuCL distributions for proton candidate tracks; the MC is separated into interaction types. Events with  $\text{MuCL} < 0.05$  are retained. (b) The data and MC MuCL distributions for muon candidate tracks; the MC is separated into interaction types. Events with  $\text{MuCL} > 0.9$  are retained. 134
- 8.21 The vertex activity for the muon sample. CCQE events are shown in red, CC- $\pi$  events are shown in green. NC- $\pi$  events are shown in yellow. The red dashed line represents the optimised cut value. The MC is POT normalised. 135
- 8.22 The  $\epsilon$  distribution in data and MC. Events with  $\epsilon > -0.6$  are retained. The MC is POT normalised. 136
- 8.23 The difference between the true proton kinetic energy,  $T_p^{\text{true}}$ , and the reconstructed proton kinetic energy,  $T_p^{\text{rec}}$ , estimated using the MC simulation. A Gaussian is fitted to the distribution to estimate the resolution. 137
- 8.24 The  $\epsilon$  distributions when the proton kinetic energy,  $T_p$ , is, (a) increased and (b) decreased, by the proton kinetic energy resolution,  $T_p^{\text{res}}$ . 138
- 8.25 The  $E_\nu^{\text{rec}}$  (left) and  $Q_{\text{rec}}^2$  (right) data and MC distributions for (a)  $\mu$  sample, (b)  $\mu + p$  sample, (c)  $\mu + \pi$  sample. The MC is POT normalised. 140
- 8.26 The  $p_\mu$  (left) and  $\cos\theta_\mu$  (right) data and MC distributions for (a)  $\mu$  sample, (b)  $\mu + p$  sample, (c)  $\mu + \pi$  sample. The MC is POT normalised. 141
- 8.27 Backwards one-track data (data points) and MC (hatched histogram) distributions. (Top left) track length, (bottom left) data/MC track length ratio, (top right) track  $\cos(\theta)$ , (bottom right) data/MC track  $\cos(\theta)$  ratio. The MC is normalised to POT. 453 events are seen in data, 236 events are expected according to MC. 142
- 8.28 Difference in the muon coincidence time and the 1<sup>st</sup> track hit time for data (data points) and MC (hatched histogram). The excess of data is predominantly for positive time differences suggesting that the excess is not due to track direction mis-reconstruction. 143
-

- 
- 9.1  $P_\mu$  vs.  $\theta_\mu$  distributions for (a) data events, (b) CCQE events in MC, (c) background events in MC. The  $\mu$ ,  $\mu + p$ , and  $\mu + \pi$  distributions are shown from left to right, respectively. 147
- 9.2  $E_\nu^{rec}$  distributions in for NEUT (left) and NUANCE (right) MC for (a)  $\mu$  sample, (b)  $\mu + p$  sample, (c)  $\mu + \pi$  sample. 151
- 9.3  $E_\nu^{rec}$  distributions excluding backwards tracks before (blue) and after (red) the fit for (a)  $\mu$  sample, (b)  $\mu + p$  sample and (c)  $\mu + \pi$  sample. 153
- 9.4  $E_\nu^{rec}$  (left) and  $Q^2$  (right) distributions excluding backwards tracks before (blue) and after (red) the fit for (a)  $\mu$  sample, (b)  $\mu + p$  sample and (c)  $\mu + \pi$  sample. 156
- 10.1 Flux-unfolded MiniBooNE  $\nu_\mu$  CCQE cross section per neutron as a function of neutrino energy. In (a) shape errors are shown as shaded boxes along with the total errors as bars. In (b) a larger energy range is shown along with results from the LSND and NOMAD experiments. Also shown are predictions from the NUANCE simulation for the Relativistic Fermi Gas model with two different parameter variations and for scattering from free nucleons with the world average  $M_A$  value. The SciBar-contained CCQE cross-section is in agreement with the MiniBooNE measurement. 161
- 10.2 The extracted cross-section for the SciBar-MRD matched sample. An  $M_A$  value of  $1.21 \text{ GeV}/c^2$  is used in the NEUT MC. The flux error is shown by the shaded region. 162
- A.1 A CCQE interaction. 163
-

---

# List of Tables

1.1	World averages for the 7 neutrino mixing parameters. The sign of $\Delta m_{32}^2$ and $\Delta m_{31}^2$ is unknown.	32
2.1	SciBooNE Milestones	44
4.1	Specifications of the SciBar Detector	52
4.2	Specifications of the EC Detector.	59
4.3	Specifications of the Muon Range Detector	62
4.4	Scintillator paddle PMT inventory.	64
5.1	Sanford-Wang parameters for $\pi^+$ , $\pi^-$ and $K_S^0$ production.	67
5.2	$K^+$ Feynman scaling parameters.	67
5.3	Meson and muon neutrino producing decay modes considered in the simulation. The corresponding anti-particle decays are also considered.	68
5.4	Number of $\nu_\mu$ interactions in SciBooNE for the NEUT MC.	72
6.1	Breakdown of all data quality cuts with fraction of POT that fail each cut. (ppp: protons per pulse)	82

---

---

6.2	Breakdown of detector failure modes and fraction of POT lost to each mode.	83
6.3	SciBooNE data run summary. The POT shown is after data quality cuts are applied.	84
7.1	The estimated probability that the Michel electron records a hit in the same TDC block as the muon in the non-stopping view.	94
7.2	Tagging efficiencies for the isotropic muon distribution.	97
7.3	Tagging Efficiencies for the isotropic proton distribution.	99
7.4	Tagging Efficiencies for the isotropic $\pi^+$ distribution.	100
7.5	Tagging Efficiencies for the isotropic $\pi^-$ distribution.	101
7.6	Tagging Efficiencies for the stopped cosmic study with a TDC deadtime of 100 ns. Not adjusting the ratio of $\mu^+$ s to $\mu^-$ s does not significantly affect the tagging efficiencies.	106
7.7	Tagging Efficiencies for different TDC deadtimes. The $\mu^+$ to $\mu^-$ ratio is set to 1.2 : 1.	108
8.1	Data and MC summary before and after applying all the pre-cuts. The dirt background is greatly reduced by applying the first layer veto and fiducial volume cuts.	120
8.2	Effect of $T_p$ resolution on the CCQE kinematic cut. The purity of CCQE events is unaffected by the resolution. The number of events in data varies by +14 and -30 for an decrease and increase in $T_p$ by $T_p^{res}$ , respectively. For a sample of 349 events the statistical uncertainty, is $\sqrt{439} = 18.6$ . The variations are within the uncertainty.	137
8.3	A summary of the two SciBar-contained CCQE samples and one SciBar-contained background sample after all cuts are applied.	139

---

9.1	The best fit values and errors for the fit parameters $a_{ccqe}$ and $a_{bkgd}$ .	150
9.2	The best fit values and errors for the fit parameters: $a_{ccqe}$ , $a_{bkgd}$ , $R_{p/\pi}$ and $R_{2trk/1trk}$ .	154
9.3	The neutrino beam systematic errors.	157
9.4	The detector systematic errors.	157
9.5	The cross-talk fit parameter values.	157

---

---

# Chapter 1

## Introduction

SciBooNE is a neutrino experiment based at the Fermi National Accelerator Laboratory in Batavia, Illinois, USA. SciBooNE's principal goal is to measure sub-GeV  $\nu_\mu$  and  $\bar{\nu}_\mu$  cross-sections, of interest to future neutrino oscillation experiments [1] where the largest two uncertainties are the neutrino beam flux and neutrino cross-sections. SciBooNE's name is a convolution of SciBar, a detector originally used in the K2K [2] experiment as a near detector, and BooNE, short for Booster Neutrino Experiment.

Below is a summary of the contents of this thesis.

- Chapter one outlines the goals of this thesis along with the history of the neutrino and some relevant neutrino physics.
  - An overview of the SciBooNE experiment with the major physics goals and milestones can be found in chapter two.
  - The Booster Neutrino Beam is explained in chapter three.
  - The SciBooNE detector is outlined in chapter four.
  - The beam, neutrino interaction (NEUT), and detector simulations are explained in chapter five.
-

- A summary of the data taken during SciBooNE's three runs is explained in chapter six.
- The muon tagging method for SciBar-contained events is explained in chapter seven.
- The analysis event selection cuts are presented in chapter eight.
- The method of cross-section extraction and systematic error analyses are presented in chapter nine.
- Conclusions and future prospects for the analysis can be found in chapter ten.

## **1.1 A History of the Neutrino**

The neutrino is the lightest of the elementary particles with mass, interacting only under the weak force. Neutrinos are the second most abundant known particle in the universe after the photon but despite their abundance they are very difficult to observe.

### **1.1.1 Prediction**

In 1914 Chadwick observed the continuous spectrum of beta rays [3]; this led to two different conjectures. Either energy and spin conservation does not hold within the nucleus (Bohr [4]) or a third particle with spin = 1/2 is produced which is not observed that carries the missing energy from the reaction. This second interpretation which was proposed by Pauli [5]. This missing particle was required to be electrically neutral. After the discovery of the neutron in 1932 [6], Enrico Fermi suggested this missing particle be called the neutrino.

---

### 1.1.2 Observation

In 1953 the neutrino was detected by the Cowan and Reines neutrino experiment [7, 8]. Anti-neutrinos produced by a nuclear reactor were identified from the products of inverse beta-decay.

$$\bar{\nu}_e + p \rightarrow n + e^+ \quad (1.1)$$

The events were identified from the delayed coincidence between the prompt electron-positron annihilation and the delayed neutron spallation. In 1955 Davis [9] set up an experiment to look for anti-neutrino capture on  $^{37}\text{Cl}$  placing the detector next to a nuclear reactor and looking for the following signal.

$$\bar{\nu}_e + {}^{37}\text{Cl} \rightarrow {}^{37}\text{Ar} + e^- \quad (1.2)$$

No signal was observed suggesting no lepton number violation in equation 1.2. This was the first evidence that neutrinos and anti-neutrinos were different particles.

The muon neutrino was discovered in 1962 in the Alternating Gradient Synchrotron (AGS) at the Brookhaven National Laboratory [10]- the first accelerator neutrino beam experiment. In 1975 the tau lepton was discovered at SLAC [11] suggesting the existence of a 3rd generation neutrino. This was finally observed by the DONUT collaboration at Fermilab in 2000 [12]. It should be noted that missing energy had been measured from tau decays, in essence indirectly observing the tau neutrino.

The LEP experiments showed that there are three interacting light neutrinos, i.e. with masses less than half the  $Z^0$  mass. This was determined from the measurement of the  $Z^0$  width [13].

---

---

## 1.2 Neutrino Physics and the Standard Model

### 1.2.1 Neutrinos in the Standard Model

The theory that describes particle physics is called the Standard Model (SM). Though the SM is the most successful particle physics model to date with hundreds of measurements confirming its predictions, it is known to be incomplete. The SM is only able to describe three of the four forces; the strong force, the weak force, and the electro-magnetic (EM) force. Gravity is not part of the SM. In the SM neutrinos are massless particles, however the confirmation of neutrino oscillations requires each neutrino mass eigenstate to be non-zero and different. Neutrino oscillations are the only confirmed physics beyond the SM.

The SM describes the interactions of the twelve matter particles (fermions) and four mediator particles (bosons), which can be seen in figure 1.1. The bosons propagate the strong and electro-weak forces; they are integer spin particles that obey Bose-Einstein statistics. Fermions account for the matter observed in the universe and are half-integer spin particles that obey Fermi-Dirac statistics.

The strong force is mediated by the gluon and the EM force by the photon. The weak force is mediated by the  $W^\pm$  and  $Z^0$  bosons. Unlike the photon which is massless the  $W^\pm$  and  $Z^0$  have masses of  $80.4 \text{ GeV}/c$  and  $91.2 \text{ GeV}/c$  respectively [15], causing the weak force to be short-ranged. The strong force is also short-ranged because the massless gluon is able to self-interact.

There are twelve fermions and twelve fermion anti-particles; identical to the fermions but with opposite charge. Within the fermions there are two distinct groups, quarks and leptons. There are six quarks, each able to interact via all three forces. Their masses range from  $2.55 \text{ MeV}/c^2$  (u) to  $171.3 \text{ GeV}/c^2$  (t) [15]. The lightest quarks combine via the strong force to make baryonic matter. Protons and neutrons are the most stable baryons and make up the majority of baryonic matter in the universe.

There are three negatively charged leptons, the electron, the muon and the tau, and three neutral neutrinos:  $\nu_e$ ,  $\nu_\mu$  and  $\nu_\tau$ . The charged leptons interact via the EM and weak forces whilst the neutrinos only interact via the weak force.

---

Three Generations  
of Matter (Fermions)

	I	II	III	
Quarks	1.5 - 3.3 MeV $\frac{2}{3}$ <b>u</b> up	1.27 GeV $\frac{2}{3}$ <b>c</b> charm	171.2 GeV $\frac{2}{3}$ <b>t</b> top	0 0 0 1 <b><math>\gamma</math></b> photon
	3.5 - 6.0 MeV $-\frac{1}{3}$ <b>d</b> down	104 MeV $-\frac{1}{3}$ <b>s</b> strange	4.2 GeV $-\frac{1}{3}$ <b>b</b> bottom	0 0 0 1 <b>g</b> gluon
	< 2.2 eV 0 $\frac{1}{2}$ <b><math>\nu_e</math></b> electron neutrino	< 0.17 MeV 0 $\frac{1}{2}$ <b><math>\nu_\mu</math></b> muon neutrino	< 15.5 MeV 0 $\frac{1}{2}$ <b><math>\nu_\tau</math></b> tau neutrino	91.2 GeV 0 0 1 <b><math>Z^0</math></b> Z Boson
Leptons	0.511 MeV -1 $\frac{1}{2}$ <b>e</b> electron	105.7 MeV -1 $\frac{1}{2}$ <b><math>\mu</math></b> muon	1.776 GeV -1 $\frac{1}{2}$ <b><math>\tau</math></b> tau	Bosons (Forces) 80.4 GeV $\pm 1$ 1 <b><math>W^\pm</math></b> W Boson

**Figure 1.1:** The twelve fermions and four bosons of the Standard Model. The fermions are separated into three generations of leptons and quarks. The leptons interact via the Weak force with the charged leptons also interacting via the electromagnetic force. The quarks interact via all three forces. Of the four bosons, the photon propagates the electromagnetic force, the gluon the Strong force and the  $Z^0$  and  $W^\pm$  the Weak force. Schematic courtesy of I. Taylor [14].

Because the weak force is propagated by massive bosons, weak cross-sections are typically  $10^{-11}$  times smaller than EM cross-sections, however the strength of the gauge coupling constants are comparable. Charge-parity symmetry is the idea that reversing the charge and spin of a particle, i.e switching particle for antiparticle with opposite spin, does not affect the physics. The weak force is however very important as it is the only force to violate charge-parity (CP) symmetry, one of the three Sakharov conditions to explain the matter-antimatter asymmetry in the universe [16]. The weak force interacts with left-handed leptons and quarks via the  $W^+$  boson and right-hand leptons and quarks via the  $W^-$  boson. The neutrino only interacts via the weak force therefore neutrino interaction cross-sections are very small.

### 1.2.2 Neutrino Oscillations

#### Theory

Neutrino oscillation is a quantum mechanical phenomenon. If neutrinos aren't massless then their mass eigenstates can be written down. There is no reason why the neutrinos mass eigenstates,  $|\nu_i\rangle$ , have to be the same as their flavour eigenstates,  $|\nu_\alpha\rangle$ ,

$$|\nu_\alpha\rangle \neq |\nu_i\rangle, \quad (1.3)$$

where  $\alpha = e, \mu, \tau$  and  $i = 1, 2, 3$ . A neutrino produced from a weak interaction exists

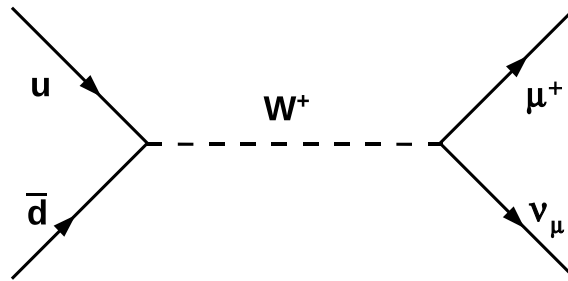


**Figure 1.2:** The pion decay Feynman diagram.

as a definite flavour eigenstate, for example,  $\pi^+$  decay produces a muon and muon neutrino, see figure 1.2, however neutrinos propagate through space as a mass eigenstate. If the neutrino does not oscillate the flavour eigenstates and mass eigenstates would be identical; in the above example the  $\nu_\mu$  would propagate unchanged. In the instance that the flavour and mass eigenstates are not equal each flavour eigenstate can be written as a sum of the mass eigenstates (equation 1.4).

$$|\nu_\alpha\rangle = \sum_i U_{\alpha i} |\nu_i\rangle \quad (1.4)$$

$U_{\alpha i}$  is the mixing matrix.

If a neutrino interacts some time later, as in a neutrino oscillation experiment, it is possible to observe a neutrino of a different flavour. This mixing process is described by a matrix,  $U$ , known as the Maki-Nakagawa-Sakata-Pontecorvo (MNSP) mixing

matrix [17, 18]. Currently there are believed to be three neutrino generations [13].  $U$  is a  $3 \times 3$  unitary matrix,

$$U = \begin{pmatrix} U_{e1} & U_{e2} & U_{e3} \\ U_{\mu1} & U_{\mu2} & U_{\mu3} \\ U_{\tau1} & U_{\tau2} & U_{\tau3} \end{pmatrix}. \quad (1.5)$$

This matrix can be written in terms of three mixing angles,  $\theta_{ij}$ , and a complex phase,  $\delta$ , related to the CP asymmetry in the lepton sector.

$$U = \begin{pmatrix} 1 & 0 & 0 \\ 0 & c_{23} & s_{23} \\ 0 & -s_{23} & c_{23} \end{pmatrix} \begin{pmatrix} c_{13} & 0 & s_{13}e^{i\delta} \\ 0 & 1 & 0 \\ -s_{13}e^{i\delta} & 0 & c_{13} \end{pmatrix} \begin{pmatrix} c_{12} & s_{12} & 0 \\ -s_{12} & c_{12} & 0 \\ 0 & 0 & 1 \end{pmatrix}, \quad (1.6)$$

where  $c_{ij}$  and  $s_{ij}$  are abbreviations for  $\cos \theta_{ij}$  and  $\sin \theta_{ij}$ , respectively.

To determine the amplitude of mixing from one flavour eigenstate to another,  $Amp(\nu_\alpha \rightarrow \nu_\beta)$ , the contributions from each mass eigenstate and the propagation of the mass eigenstates through space must be considered.

$$Amp(\nu_\alpha \rightarrow \nu_\beta) = \sum_i U_{\alpha i}^* \times \Psi(\nu_i) \times U_{\beta i} \quad (1.7)$$

Where  $\Psi(\nu_i)$  represents the propagation of mass eigenstate  $i$ .

To determine the propagation term,  $\Psi(\nu_i)$ , we can apply the time-dependent Schrödinger equation (with  $\hbar = c = 1$ ).

$$|\nu_i(t)\rangle = e^{-i(E_i t - p_i \cdot x)} |\nu_i(0)\rangle \quad (1.8)$$

Where  $E_i$  and  $p_i$  are the energy and momentum of mass eigenstate  $\nu_i$  in the laboratory frame. The neutrino is highly relativistic such that  $t \approx x$ , therefore equation 1.8 simplifies to

$$|\nu_i(x)\rangle = e^{-i(E_i - p_i)x} |\nu_i(0)\rangle \quad (1.9)$$

If we assume that the flavour eigenstate,  $\nu_\alpha$ , has a definite momentum,  $p$ , then we can say that all the mass eigenstate components of  $\nu_\alpha$  have momentum's  $p_i = p$ . Additionally if we assume that the neutrino masses are tiny in comparison to

their energies then we can make the approximation  $E_i = \sqrt{p^2 + m_i^2} \approx p + \frac{m_i^2}{2p}$ . Equation 1.9 becomes:

$$|\nu_i(x)\rangle = e^{-im_i^2 x/2p} |\nu_i(0)\rangle. \quad (1.10)$$

If  $E$  is the average energy of the mass eigenstates we can let  $E \simeq p$  and therefore

$$|\nu_i(x)\rangle = e^{-im_i^2 x/2E} |\nu_i(0)\rangle, \quad (1.11)$$

and therefore a  $\nu_\alpha$  is described a distance  $x$  from its production by the state vector

$$|\nu_\alpha(x)\rangle = \sum_i U_{\alpha i}^* e^{-im_i^2 x/2E} |\nu_i\rangle. \quad (1.12)$$

The probability of measuring a flavour eigenstate  $\nu_\beta$  given a source of  $\nu_\alpha$  a distance  $L$  from the source is

$$\begin{aligned} P(\nu_\alpha \rightarrow \nu_\beta) &= |Amp(\nu_\alpha \rightarrow \nu_\beta)|^2 = |\langle \nu_\beta | \nu_\alpha(L) \rangle|^2 = \left| \sum_i U_{\alpha i}^* e^{-im_i^2 L/2E} U_{\beta i} \right|^2 \\ &= \delta_{\alpha\beta} - 4 \sum_{i>j} Re(U_{\alpha i}^* U_{\beta i} U_{\alpha j} U_{\beta j}^*) \sin^2 \left( \frac{\Delta m_{ij}^2 L}{4E} \right) \\ &\quad + 2 \sum_{i>j} Im(U_{\alpha i}^* U_{\beta i} U_{\alpha j} U_{\beta j}^*) \sin \left( \frac{\Delta m_{ij}^2 L}{2E} \right). \end{aligned} \quad (1.13)$$

From experiment we know that  $\Delta m_{13}^2 \simeq \Delta m_{23}^2 \gg \Delta m_{12}^2$  [15], and therefore we can approximate equation 1.13 using two flavour and two mass eigenstates. In this instance  $U$  can be described as a simple rotational matrix

$$U = \begin{pmatrix} \cos \theta & \sin \theta \\ -\sin \theta & \cos \theta \end{pmatrix}, \quad (1.14)$$

where  $\theta$  is the mixing angle.

Making this approximation simplifies equation 1.13 to

$$P(\nu_\alpha \rightarrow \nu_\beta) = \sin^2 2\theta \sin^2 \frac{\Delta m^2 L}{4E} = \sin^2 2\theta \sin^2 \frac{1.27 \Delta m^2 L}{E} \quad (1.15)$$

Where  $\Delta m^2 = m_2^2 - m_1^2$  is measured in  $(eV/c^2)^2$ ,  $L$  in km and  $E$  in GeV. Reintroducing  $\hbar$  and  $c$  gives the factor of 1.27.

## Experiment

In 1968, Ray Davis’s Homestake neutrino experiment measured a deficit in the neutrino flux from the sun. The standard solar model (SSM) predicted a rate of between 6.6 and 8.1 electron neutrinos per SNU, where 1 SNU = one neutrino interaction per  $10^{36}$  target atoms/second. The Homestake experiment measured the electron neutrino flux to be  $2.56 \pm 0.16(\text{stat}) \pm 0.16(\text{sys})\text{SNU}$  [19]. In 1990 the Kamioka Nucleon Decay Experiment (Kamiokande) confirmed the findings of Homestake by measuring the solar neutrino flux. The flux was measured to be  $2.35 \pm 0.02(\text{stat}) \pm 0.08(\text{sys}) \times 10^6 \text{ cm}^2\text{s}^{-1}$ . This is half the rate expected from the SSM. Only the most energetic neutrinos produce electrons above the Čerenkov threshold in Kamiokande with sufficient momentum for the neutrino direction to be reconstructed. Kamiokande was the first experiment to have clear evidence of neutrinos coming from the direction of the sun [20]. A series of models to explain the deficit were proposed including neutrino oscillations and neutrino decay.

The SNO collaboration confirmed the deficit was due to “direct evidence of neutrino flavour transformation”<sup>1</sup> [21] in 2002 by measuring both the charged-current (CC) and neutral current (NC) fluxes. A deficit was seen for CC interactions in agreement with Kamiokande, whilst for NC interactions a flux in agreement with the SSM was observed. This ruled out neutrino decay models as NC interactions are independent of neutrino flavour, therefore the deficit could only be explained by flavour transformation.

The current neutrino oscillation model is described by three mixing angles, three mass differences and one CP violating phase. In 1996 the LSND experiment saw a signal for  $\bar{\nu}_\mu \rightarrow \bar{\nu}_e$  oscillations with a  $\Delta m^2 \sim 1 \text{ eV}^2$  [22]. This  $\Delta m^2$  is too large to fit with the other neutrino oscillation measurements given three neutrino flavours. This measurement can be explained by introducing sterile neutrinos; these neutrinos don’t interact via the weak force, however it is possible for neutrinos to oscillate into these sterile flavours. In 2007 MiniBooNE demonstrated that neutrinos do not oscillate with  $\Delta m^2 \sim 1 \text{ eV}^2$  when looking at  $\nu_\mu \rightarrow \nu_e$  oscillations [23].

---

<sup>1</sup>Though not a confirmation of oscillations, taken with all other measurements it is widely accepted as such

---

The current world's best values can be seen in table 1.1 [15, 24, 25]; all experimental data can be seen in figure 1.3 [26].

Parameter	Value
$\theta_{12}$	$33.9^{+2.4}_{-2.2}{}^\circ$
$\theta_{13}$	$<3.2{}^\circ$
$\theta_{23}$	$45 \pm 7{}^\circ$
$\Delta m_{21}^2$	$+8.0^{+0.6}_{-0.4} \times 10^{-5} \text{eV}^2$
$\Delta m_{32}^2$	$2.4^{+0.6}_{-0.5} \times 10^{-3} \text{eV}^2$
$\Delta m_{31}^2$	$\approx \Delta m_{32}^2$
$\delta$	no measurement

**Table 1.1:** World averages for the 7 neutrino mixing parameters. The sign of  $\Delta m_{32}^2$  and  $\Delta m_{31}^2$  is unknown.

### 1.2.3 Neutrino-Nucleus Interactions

#### Motivation

In neutrino oscillation experiments the neutrino is detected via neutrino-nucleus interactions. For neutrino energies around 1 GeV, of interest to neutrino oscillations experiments such as T2K, there is no dominant interaction mode; instead there are three interaction modes of interest. The neutrinos can interact via neutral current (NC) and charged current (CC) processes:

- Quasi-elastic scattering:  $\nu_\alpha N \rightarrow l_\alpha N'$ ;
- Single pion production:  $\nu_\alpha N \rightarrow l_\alpha N' \pi$  (resonant), or  $\nu_\alpha A \rightarrow l_\alpha A \pi$  (coherent);
- Deep inelastic scattering:  $\nu_\alpha N \rightarrow l_\alpha N' + \text{hadrons}$ .

Figure 1.4 shows the CC interaction Feynman diagrams.

For neutrino interactions on nuclear targets there are effects that have to be considered that don't apply to interactions with free, or quasi-free, nucleons. These include

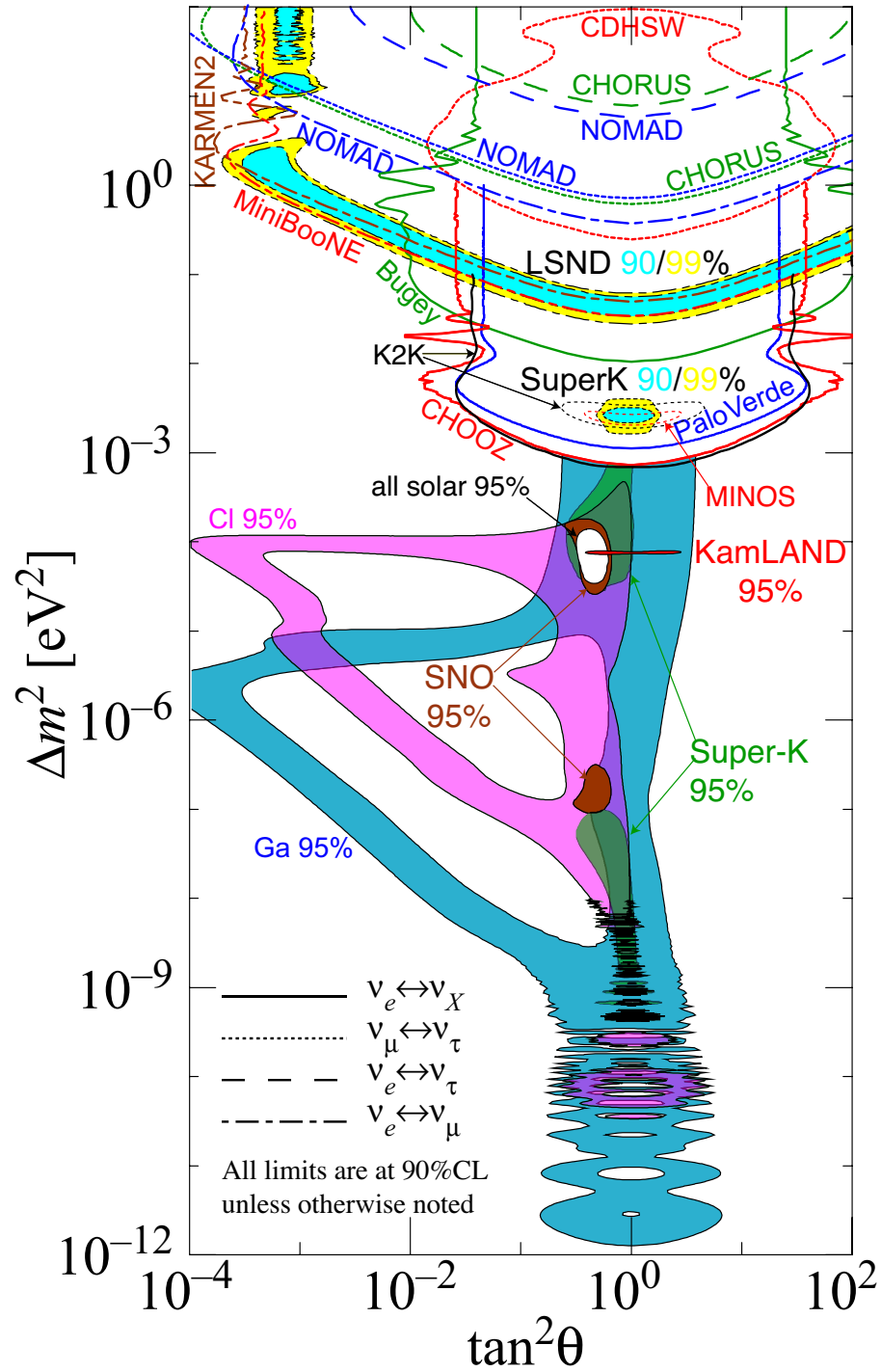


**Figure 1.3:** Current allowed and excluded regions in  $\tan^2 \theta - \Delta m^2$  space. The best measurement of  $\nu_e \rightarrow \nu_X$  oscillations is from KamLAND for a  $\Delta m^2 \sim 8.0 \times 10^{-5} \text{ eV}^2$ . The best measurements for  $\nu_\mu \rightarrow \nu_\tau$  oscillations come from the MINOS, K2K and SuperK experiments for a  $\Delta m^2 \sim 2.4 \times 10^{-3} \text{ eV}^2$ .  $\Delta m^2$ 's larger than  $1 \text{ eV}^2$  are largely excluded across the full angular space. The LSND experiment saw a signal corresponding to a  $\Delta m^2 \sim 1 \text{ eV}^2$  for  $\bar{\nu}_\mu \rightarrow \bar{\nu}_e$ , this was not seen by the MiniBooNE collaboration when studying the same oscillation signature in neutrino mode.

This plot is courtesy of M. Hitoshi [26].

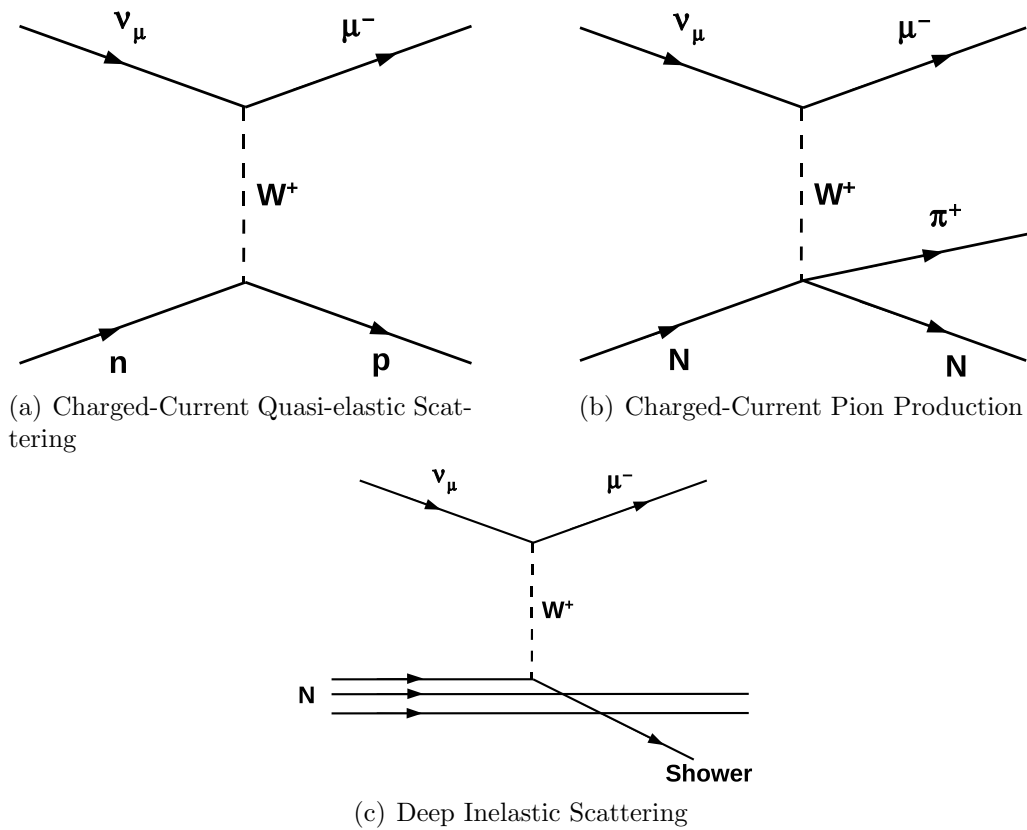


**Figure 1.4:** Charged-current neutrino-nucleus interaction Feynman diagrams for (a) quasi-elastic scattering, (b) pion production and (c) deep inelastic scattering.

the Fermi-motion of the initial state nucleon in the nucleus; the Pauli exclusion principle, which suppresses the cross-sections of interactions with small momentum transfer; and the intra-nuclear interactions of produced mesons or nucleons within the nucleus.

T2K's far detector is the Super-Kamiokande water Čerenkov detector. At T2K energies neutrino interactions in water tend to produce only one particle above the Čerenkov threshold; for charged-current interactions this is typically the neutrino lepton partner. Therefore reconstruction of the neutrino energy is achieved using only the lepton kinematics and direction of the incoming neutrino, assumed to be the direction of the neutrino source (a valid assumption in long baseline experiments). Charged-current quasi-elastic (CCQE) and charged-current pion production (CC- $\pi$ ) are the two major interaction modes at T2K. If the pion for a CC- $\pi$  interaction is absorbed in the nucleus the event is indistinguishable from a CCQE event. Since

CCQE events are two-body interactions it is possible to reconstruct the neutrino energy,  $E_\nu^{rec}$ , from only the lepton kinematics,

$$E_\nu^{rec} = \frac{1}{2} \frac{(m_p^2 - m_\mu^2) - (m_n - V)^2 + 2E_\mu(m_n - V)}{(m_n - V) - E_\mu + p_\mu \cos \theta_\mu}, \quad (1.16)$$

where  $E_\mu$  is the muon energy,  $p_\mu$  the muon momentum,  $\theta_\mu$  the muon angle relative to the neutrino beam;  $m_\mu$ ,  $m_p$  and  $m_n$  are the muon, proton and neutron masses respectively.  $V$  is the nuclear potential. This is not true for a CC- $\pi$  event where the reconstructed neutrino energy given the lepton kinematics will be lower than the true neutrino energy. The CCQE interaction is the signal mode for oscillation analyses at T2K. This is because CCQE events are the dominant interaction mode and the neutrino energy can be easily reconstructed given only the lepton kinematics. CC- $\pi$  interactions are the dominant background for  $\nu_\mu$  disappearance measurements. Figure 1.5 shows the expected reconstructed neutrino energy for signal and background events at T2K. It is crucial for an oscillation experiment to understand the

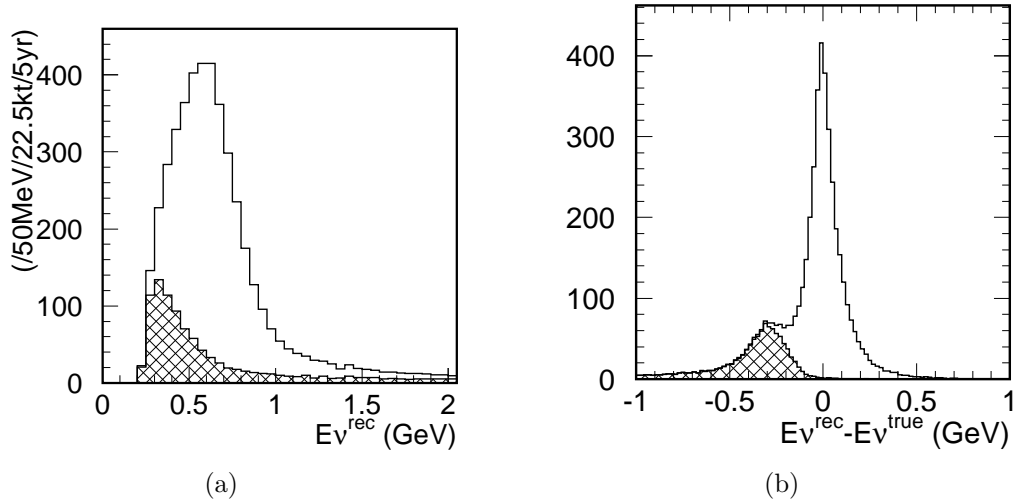


**Figure 1.5:** (a) Expected reconstructed neutrino energy,  $E_\nu^{rec}$ , distribution for T2K using lepton kinematics, (b)  $E_\nu^{rec} - E_\nu^{true}$ . The hatched histogram shows the background contribution

signal and background rates. Given the lack of cross-section measurements around a few-GeV for both CCQE and background processes, and the mis-reconstruction of neutrino energies for background events, it is important to have accurate measurements of each process. The uncertainty on the non-QE background processes and their effect on the oscillation parameters for T2K was studied [27]. Figure 1.6

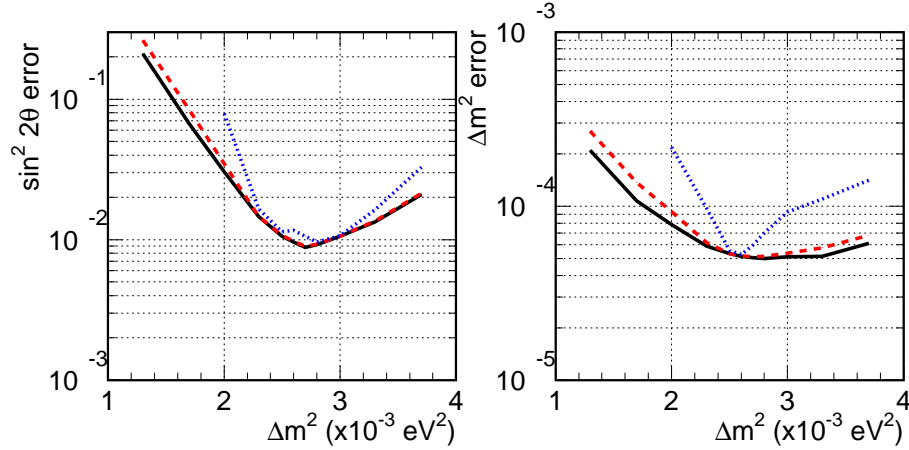


**Figure 1.6:** Size in the measurement errors of the oscillation parameters,  $\sin^2 \theta_{23}$  and  $\Delta m_{23}^2$  as a function of true  $\Delta m_{23}^2$  for a systematic error on the non-QE/CCQE cross-section ratio of 5% (red dashed), and 20% (blue dotted). The solid line shows the expected statistical error. courtesy of K. Hiraide [27]

shows the effect a 5% and 20% systematic uncertainty on the non-QE background has on the measurement bias for the oscillation parameters,  $\sin^2 \theta_{23}$  and  $\Delta m_{23}^2$  as a function of true  $\Delta m_{23}^2$ . As such, a 5% uncertainty on the backgrounds is desired.

This requires accurate neutrino-nucleus cross-sections for all interaction modes. Figure 1.7 shows the charged-current  $\nu_\mu$  cross-sections for a compilation of previous experiments. Currently there are few measurements of cross-sections below one GeV.

SciBooNE is a  $\nu_\mu$  and  $\bar{\nu}_\mu$  cross-section experiment with the aim to measure  $\nu_\mu$  and  $\bar{\nu}_\mu$  cross-sections applicable to  $\nu_\mu$  disappearance and  $\nu_e$  appearance studies, principally for T2K.

### Charged-Current Interactions

Charged-current (CC) interactions are weak interactions via the  $W^\pm$  gauge bosons. As highlighted in section 1.2.3 there are three prominent interaction modes, CCQE scattering, CC- $\pi$  production and deep inelastic scattering (DIS) (see figure 1.4). DIS is a negligible cross-section at SciBooNE energies and so will not be considered here. Additionally CC- $\pi$  production can be sub-divided into resonant  $\pi^\pm$  production,

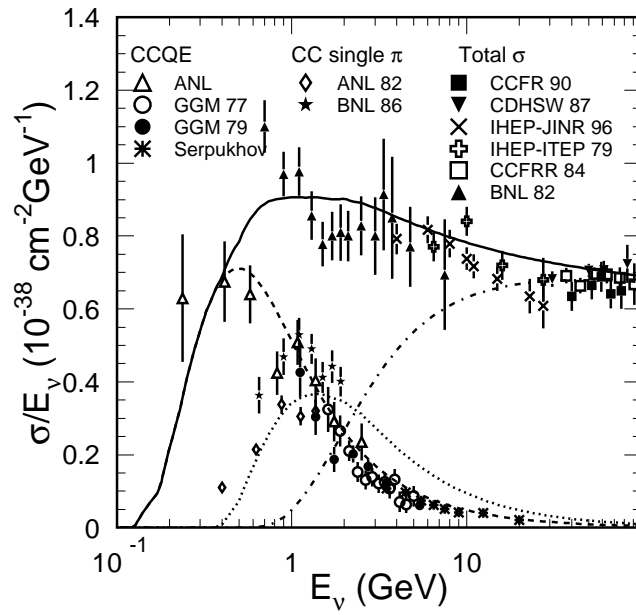


**Figure 1.7:** Charged-current total cross-section interactions normalised by  $E_\nu$ . The dashed, dotted and dash-dotted lines show the calculated quasi-elastic, single meson and deep inelastic scatterings, respectively. The data points are taken from the following experiments: ( $\triangle$ )ANL [28], ( $\circ$ )GGM77 [29], ( $\bullet$ )GGM79(a) [30],(b) [31], ( $\ast$ )Serpukhov [32], ( $\diamond$ )ANL82 [33], ( $\star$ )BNL86 [34], ( $\blacksquare$ )CCFR90 [35], ( $\blacktriangledown$ )CDHSW87 [36], ( $\times$ )IHEP-JINR96 [37], ( $\oplus$ )IHEP-ITEP79 [38], ( $\square$ )CCFRR84 [39], and ( $\blacktriangle$ )BNL82 [40]. Plot courtesy of the K2K collaboration [41].

coherent  $\pi^\pm$  production and  $\pi^0$  production. Here I will describe CCQE and CC- $\pi$  production for neutrino interactions.

### CCQE Scattering

The CCQE scattering process converts a target neutron into a proton via a charged current interaction (Note: For anti-neutrinos the CCQE scattering process is a target proton into a neutron). The Llewellyn-Smith formalism [42] is used to model quasi-elastic scattering. In SciBooNE the event signature for a CCQE interaction is a two-track event with a reconstructed muon and proton. SciBooNE also has the capability to reconstruct the decay electron from the muon if the muon stops in the SciBar detector.

### CC- $\pi$ Production

There are two types of pion production interaction, resonant and coherent. Resonant pion production is due to baryonic resonance off a bound nucleon within the nucleus, this is the dominant single pion production process. The resonance state decays to produce a nucleon and pion. In the case of CC resonant pion production:



Where  $N$  and  $N'$  are the nucleons.

Coherent pion production occurs when the neutrino interacts with a target nucleon coherently, with a small momentum transfer such that final state lepton and pion travel forward in the laboratory frame and there is no target nucleus break-up. The pion from CC- $\pi$  events can be absorbed in the nucleus, resulting in only the muon and proton tracks being observed in the detector. Because CC- $\pi$  events can look like CCQE events they are the dominant background to a CCQE analysis.

### Neutral-Current Interactions

Neutral-current (NC) interactions are weak interactions via the  $Z^0$  gauge boson. Because there is no flow of charge it is not possible to know the flavour of the neutrino that interacted. These events can still be a background in an oscillation experiment with  $\gamma$ 's from  $\pi^0$  production acting as a background to  $\nu_e$  appearance, and  $\pi^\pm$  production being a major background to  $\nu_\mu$  disappearance studies. Figure 1.8 shows some examples of NC interactions. The major NC interaction background to a CCQE analysis is NC- $\pi$  production, with the pion being mis-reconstructed as a muon.

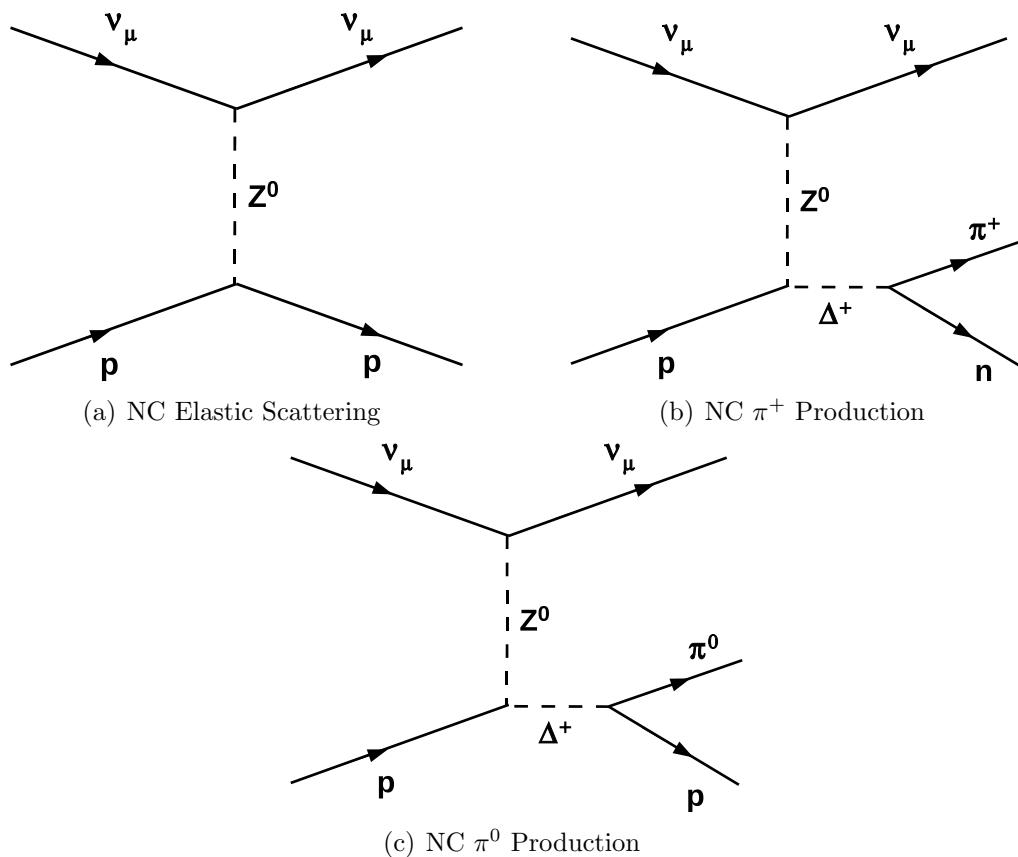


**Figure 1.8:** Neutral-current neutrino-nucleus interaction Feynman diagrams for (a) elastic scattering, (b)  $\pi^+$  production, and (c)  $\pi^0$  production.

The neutrino-nucleon interaction models used by SciBooNE are explained in more detail in chapter 5.

---

# Chapter 2

## The SciBooNE Experiment

The SciBar Booster Neutrino Experiment (SciBooNE) [1] measures neutrino cross-sections with energies around 1 GeV. The experiment is based at the Fermi National Accelerator Laboratory (FNAL) in Batavia, Illinois, USA.

The experimental layout consists of:

- **The Booster Neutrino Beam**

The BNB, originally constructed for use by the MiniBooNE [43] collaboration, takes 8 GeV protons from the proton booster and collides them on to a beryllium target. The subsequent meson decays result in a high intensity, low energy, neutrino beam.

- **The SciBooNE Detector**

The SciBooNE detector consists of 3 sub-detectors; SciBar, the Electron-Catcher (EC) and the Muon Range Detector (MRD). The SciBar detector is a fully-active scintillator detector acting as both target and detector of neutrino interactions. It has a fiducial mass of 10 tonnes.

SciBooNE consists of a pre-existing, high intensity, neutrino beam, a fine-grained, fully active detector in SciBar, an electromagnetic calorimeter, and a muon range detector. Both the beam and SciBar are well understood from previous experiments

---

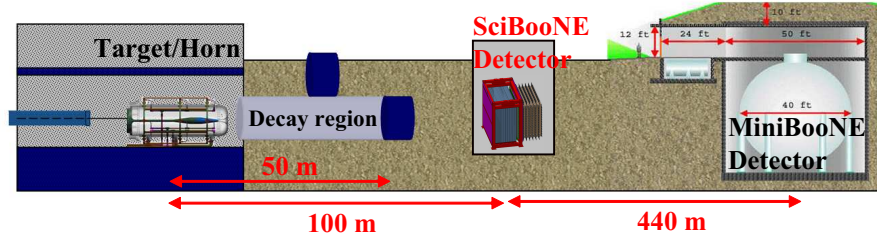


**Figure 2.1:** Schematic of Booster Neutrino Beamline. The SciBooNE and MiniBooNE detectors are also pictured. Courtesy of K. Hiraide [46].

allowing us the unique opportunity to measure precise cross-sections with them [2, 44, 45].

Figure 2.1 shows a schematic of the SciBooNE beamline. SciBooNE is situated on-axis, 100 m downstream of the proton target, 50 m from the beam absorber. MiniBooNE is located a further 440 m downstream of SciBooNE. A detailed description of the BNB can be found in chapter 3. A detailed description of the SciBooNE detector can be found in chapter 4.

## 2.1 Motivation for the SciBooNE Experiment

SciBooNE has three primary physics motivations: Precise measurements of neutrino-nucleus cross-sections, measurements of antineutrino-nucleus cross-sections and to collaborate with MiniBooNE’s neutrino oscillation analyses.

### 2.1.1 Precise Neutrino Cross-Section Measurements

As mentioned in section 1.2.3 there are few precise measurements of neutrino cross-sections below 1 GeV on carbon.

SciBooNE is able to make precise cross-section measurements in an energy region of interest to the T2K experiment [47], one of the next generation neutrino oscillation experiments. As can be seen in figure 2.2, SciBooNE has a similar peak neutrino energy flux to the expected T2K beam flux. These measurements will provide an independent data set and will be implemented into the T2K MC. It is to this sub-set of measurements that the work in this thesis belongs.

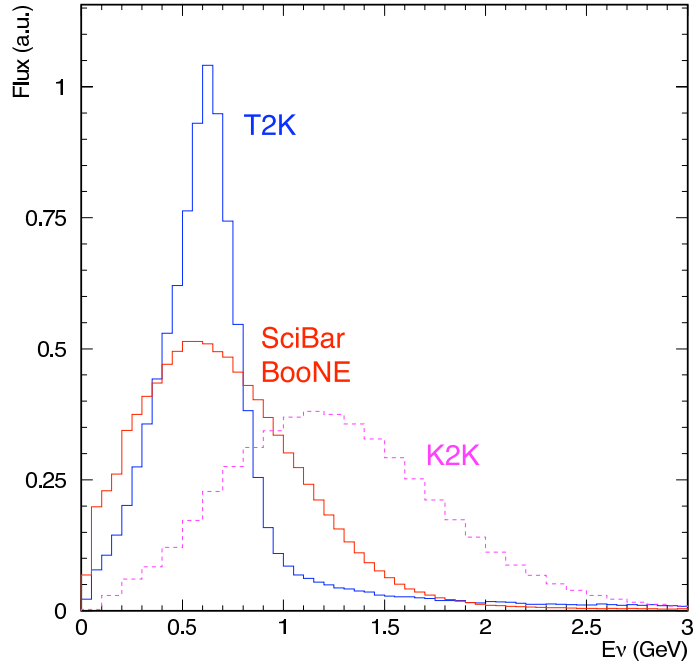


**Figure 2.2:** Comparison of the proposed off-axis T2K neutrino beam flux (blue) with the Booster neutrino beam flux (red) and the K2K beam flux (pink). The K2K neutrino beam has a higher peak beam flux than T2K. Consequently cross-section measurements made by K2K are in a different energy region to T2K. All curves are normalised to unit area. [1]

### 2.1.2 Anti-Neutrino Cross-section Measurements

Currently there are no anti-neutrino cross-section measurements below 1 GeV. If  $\theta_{13}$  is finite then CP violation in the neutrino sector can be studied. To measure the CP violating phase,  $\delta$  (see section 1.2.2), neutrino oscillations with neutrinos and antineutrinos need to be measured. For this to be possible precise measurements are needed in both the neutrino and anti-neutrino sector.

### 2.1.3 Oscillation Searches

SciBooNE is also able to act as a near detector to MiniBooNE in its  $\nu_e$  appearance search and its  $\nu_\mu$  disappearance search. Having a near detector in an oscillation search allows flux measurements to be made before oscillation, the largest uncertainty in most neutrino experiments. In the case of  $\nu_e$  appearance the intrinsic  $\nu_e$  background can be measured in SciBooNE. In the case of  $\nu_\mu$  disappearance, the  $\nu_\mu$  rate can be measured.

## 2.2 SciBooNE Timeline

The SciBooNE collaboration was formed in the summer of 2005. A series of physics case studies were undertaken [48] before the SciBooNE proposal [1] was presented to the FNAL Physics Advisory Committee (PAC). SciBooNE was approved in December 2005. The SciBar and EC detectors were disassembled at KEK between November 2005 and February 2006. Once disassembled the detectors were shipped to FNAL arriving in July 2006. In May 2006 the first MRD counter prototypes were built and tested at FNAL with design approval in June 2006. The MRD counter production ran from July 2006 until November 2006.<sup>1</sup> Civil construction began in September 2006 and was completed in March 2007. The MRD and SciBar/EC detectors were assembled in separate facilities. Construction for both sub-detectors began in November 2006 and was completed in March 2007 including commissioning with cosmic data. The detectors were moved to the detector hall in April 2007, followed by the implementation of all DAQ and computing systems. Commissioning of the detector was completed in June 2007 with first data taken in anti-neutrino mode on June 8<sup>th</sup> 2007. Run-I ran in anti-neutrino mode until the FNAL summer shutdown in August 2007. During the summer shutdown the horn polarity was switched allowing SciBooNE to run in neutrino mode from October 2007 until April 2008 (Run-II). Once our proton on target requirements were met in neutrino mode, the horn polarity was switched again, returning SciBooNE to anti-neutrino running (Run-III). Run-III ran from April 2008 until 18<sup>th</sup> August 2008 after which SciBooNE was switched off and decommissioned. The first result from SciBooNE was published in January 2009 [49]. Table 2.1 highlights the major milestones for the SciBooNE experiment.

---

<sup>1</sup>A description of this work can be found in section 4.3.1

---

Date	Milestone
Summer 2005	SciBooNE Collaboration formed
Nov. 2005 - Feb. 2006	SciBar/EC disassembly at KEK
Dec. 2005	FNAL PAC Approval- SciBooNE, E954
June 2006	MRD Prototype Counter Design Approval
June 2006 - Dec. 2006	MRD Counter Construction
July 2006	SciBar and EC arrive at FNAL
Sept. 2006	Civil construction begins
Nov. 2006 - Mar. 2007	Sub-detector's assembled
Apr. 2007	Detector Installation
May 2007	Detector Commissioning
June 2007 - Aug. 2007	Run I ( $\bar{\nu}_\mu$ mode)
Oct. 2007 - Apr. 2008	Run II ( $\nu_\mu$ mode)
Apr. 2008 - Aug. 2008	Run III ( $\bar{\nu}_\mu$ mode)
Jan. 2009	1 <sup>st</sup> SciBooNE Publication [49]

**Table 2.1:** SciBooNE Milestones

---

# Chapter 3

## The Booster Neutrino Beam

In this chapter the production apparatus of the Booster Neutrino Beam (BNB) is described. A full description of the BNB can be found in the BooNE technical design reports [44, 45, 50].

### 3.1 The Booster

The Booster is the primary proton accelerator used by the Tevatron; from this protons are syphoned off to the Booster Neutrino Beam Target to produce a neutrino beam. The Booster accelerates batches of protons up to 8 GeV with  $4.2 \times 10^{12}$  protons per batch. Selected batches for the BNB are called spills. Each spill is made up of 81 bunches, approximately 6 ns wide and 19 ns apart. This gives a total spill width of 1.6  $\mu$ s. The Booster cycle rate is defined by the accelerator timing and is approximately 2 seconds long. During each cycle the BNB will take a single stream of spills from the Booster with a maximum of 10 spills at 15 Hz. An aerial view of the Booster Neutrino Beamline can be seen in figure 3.1. To syphon these protons from the beamline requires the use of dipole magnets which deflect the spills into the Neutrino Beam Target Hall.

Each spill is monitored by two pairs of wire array beam position monitors located along the beamline. These pairs of beam monitors record the horizontal and vertical

---

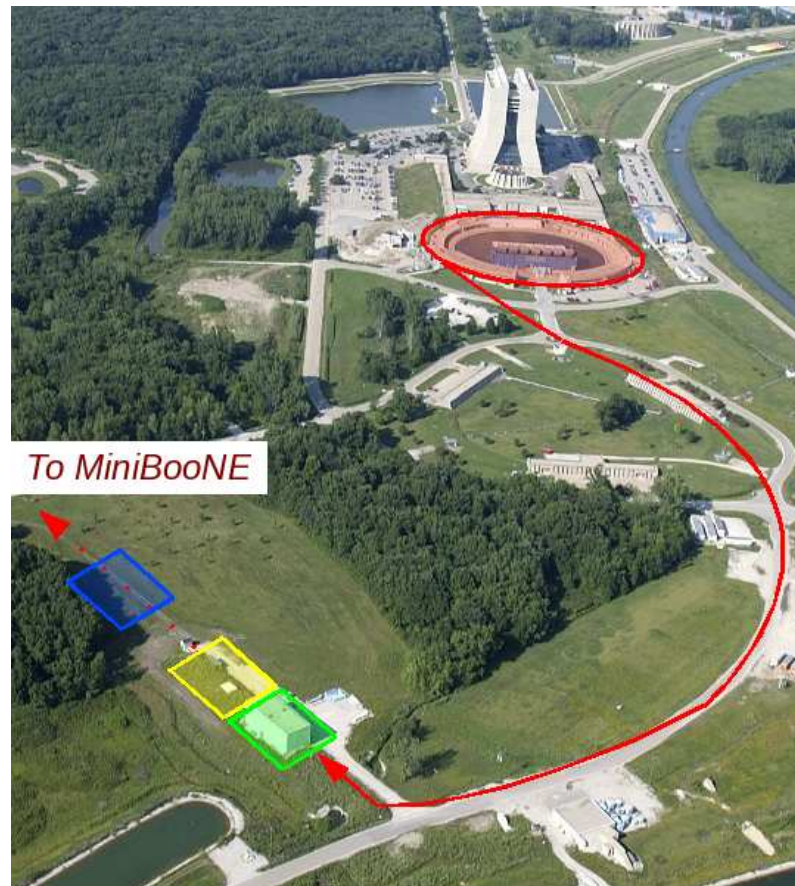


**Figure 3.1:** An aerial view of the Booster Neutrino Beamline. The red line plots the route of the protons from the Booster and where they are syphoned into the Neutrino Beam Target Hall (green box). The yellow box represents the decay volume beyond the target and the blue box shows the location of the SciBooNE detector hall (not shown). MiniBooNE is located 440 m further down stream from SciBooNE.

positions of each spill. This allows calculation of the position and angle of the beam when it hits the target for each event. Typical values for the beam position and divergence are 1 mm and 1 mrad from the target centre and axis respectively. The beam profile is also measured with typical horizontal and vertical profiles of 2 mm (RMS), this is within SciBooNE's experimental requirements.

Additionally to these monitors the number of protons on target (POT) is also calculated. This is done using a pair of toroidal current transformers (toroids) located in front of the target. Gain and pedestal calibration is achieved using test current pulses, these are done on a spill-by-spill basis. The toroids record a measurement of the POT with a 2% uncertainty.

## **3.2 The Magnetic Focusing Horn and Beam Target**

Modern neutrino beams are produced using hadronic decays. In the case of the BNB this is achieved by colliding a beam of protons on to a beryllium target and focusing the resultant mesons produced. The beryllium target is made up of 7 cylindrical slugs each with a radius of 0.51 cm. The total length of the target is 71.1cm. The reason for using multiple rods rather than one long rod is to minimise damage to the target from the shock-wave and subsequent heating produced by the beam. The beryllium target is housed within an aluminium magnetic horn. The magnetic horn is used to focus and sign select the resultant mesons in the direction of the neutrino detectors. By changing the polarity of the horn allows the BNB to run in either neutrino or anti-neutrino mode. The focusing is achieved with a toroidal magnetic field produced between the 2 aluminium co-axial conductors. The horn field is produced by pulsing a 174 kA current through the alloy structures. Each pulse is a half-sinusoid 143  $\mu$ s long, synchronised to each beam spill. The pulsed nature of the current results in a residual field within the inner conductor (skin depth effect). The high current required to produce the field would melt the aluminium structures if run constantly.

---

### 3.3 The Decay Volume

An evacuated 50 m (length)  $\times$  1.8 m (diameter) cylindrical volume sits downstream of the horn providing low angle mesons a space to decay. This greatly reduces neutrinos produced from high angle mesons since they are absorbed by the surrounding dirt, increasing the sign-selected purity. Additionally to this the 50 m length allows the mesons to decay in flight, boosting the neutrino direction towards SciBooNE. The majority of mesons produced are pions with the following decay chain:

$$\pi^+ \rightarrow \mu^+ + \nu_\mu \quad (3.1)$$

$$\mu^+ \rightarrow e^+ + \bar{\nu}_\mu + \nu_e \quad (3.2)$$

The 50 m decay length optimises the number of primary pion decays (equation 3.1) resulting in a high  $\nu_\mu$  flux, whilst absorbing the majority of muons before decay, minimising the  $\nu_e$  contamination (equation 3.2) in the neutrino beam.

---

# Chapter 4

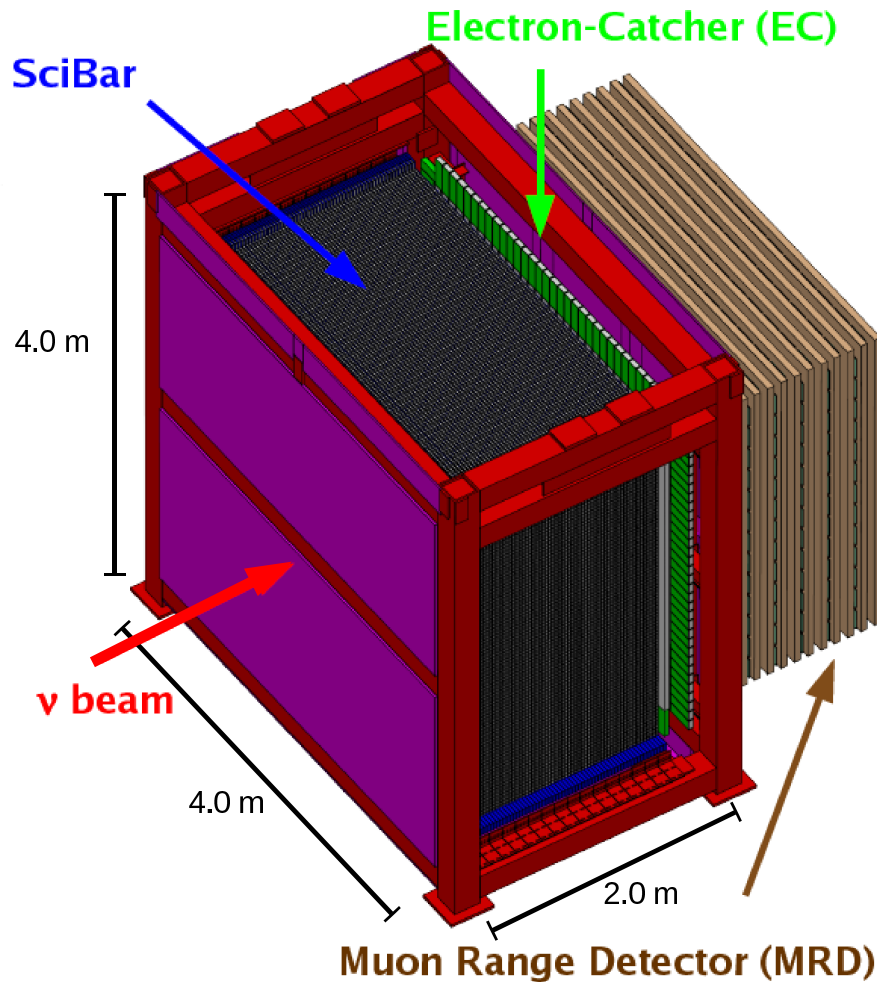
## The SciBooNE Detector

Figure 4.1 shows the SciBooNE detector. The SciBooNE detector consists of three sub-detectors: SciBar, the Electron-Catcher (EC), and the Muon Range Detector (MRD). The furthest upstream detector is SciBar, a fully active scintillator detector, acting as both the neutrino target and tracking detector. The EC is downstream of SciBar and acts as an electromagnetic shower absorber, ideal for identifying  $\pi^0$  and  $\nu_e$  candidate events. Both SciBar and the EC are enclosed inside a dark box, used to shield the detector from outside light contamination. The MRD sits behind the EC and consists of alternating iron plates and scintillator paddles, used to range out muons with momentum  $<1.2$  GeV/c from CC interactions. Given the large mass of the MRD there are a significant number of neutrino interactions on iron which can be observed. In the following sections, sub-detectors and data-acquisition systems will be described; detector alignment and coordinate systems will also be described.

### 4.1 Scintillator Bar Detector (SciBar)

SciBar was originally used in the K2K experiment as an upgrade to the lead-glass calorimeter near detector [2]. A schematic of the SciBar detector can be seen in figure 4.2. In SciBooNE, SciBar is positioned upstream from the other sub-detectors,

---



**Figure 4.1:** A schematic of the SciBooNE detector. The SciBooNE detector consists of three sub-detectors; SciBar, the Electron-Catcher (EC) and the Muon Range Detector (MRD). SciBar and the EC are contained within a darkbox (red framed structure in schematic).

acting as the primary neutrino target. The major role of SciBar is to accurately reconstruct neutrino-nucleus interactions by reconstructing the interaction vertex and all charged particle tracks. In addition to track reconstruction, SciBar is capable of particle identification by using  $\frac{dE}{dx}$  information. After dismantling, SciBar was shipped from Japan to Fermilab in July 2006 where it was reconstructed for use by SciBooNE.

SciBar consists of 14,336 scintillator bars with dimensions  $1.3 \times 2.5 \times 300 \text{ cm}^3$ . These bars act as neutrino target and detective medium. Each bar is read out at one end by a wavelength-shifting (WLS) fibre attached to a 64-channel multi-anode photo-multiplier tube (MA-PMT). A front-end electronics board (FEB), attached

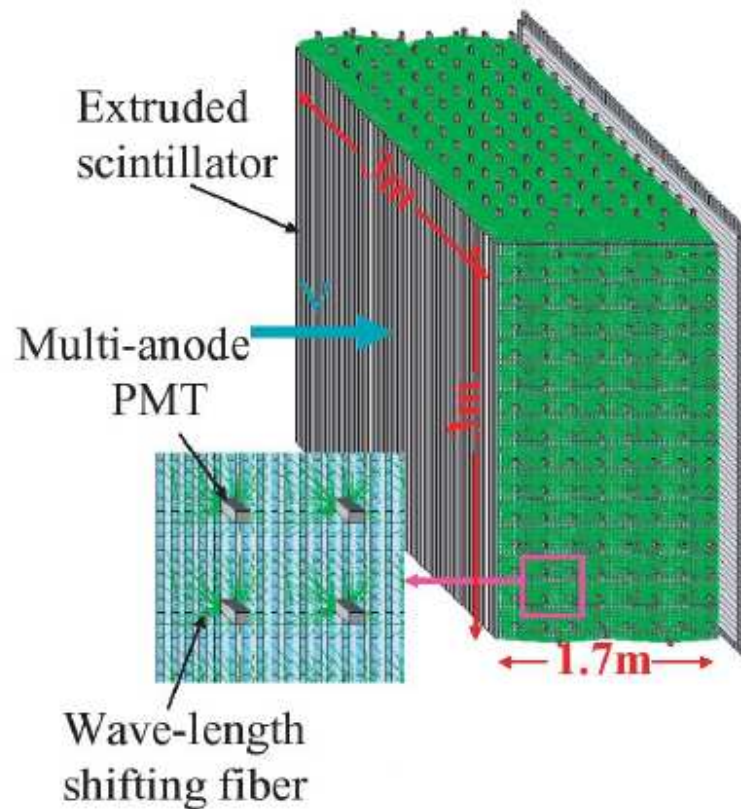


**Figure 4.2:** A schematic of the SciBar detector. SciBar consists of 14,336 extruded scintillator bars readout by 224 multi-anode photo-multiplier tubes. Each photo-multiplier tube reads out an  $8 \times 8$  array of channels in either the horizontal or vertical view.

to the MA-PMT and back-end VME module, records timing and charge information for each channel. A light-emitting diode (LED) system is used to monitor the gain of the MA-PMTs. Cosmic data is used to do energy and timing calibrations.

A summary of SciBar's specifications can be seen in table 4.1.

#### 4.1.1 Scintillator Bars

Each bar is composed of polystyrene ( $C_8H_8$ ), PPO (1%) and POPOP (0.03%). Each bar is  $1.3 \times 2.5 \times 300 \text{ cm}^3$  with a 0.25 mm thick  $TiO_2$  reflective coating isolating the light in each bar. The peak of the emission spectrum is 420 nm as shown in figure 4.3. A 1.8 mm diameter hole runs the length of each scintillator bar for the wavelength-shifting fibre. The scintillator was developed and produced at FNAL. SciBar consists of 64 horizontal-vertical modules, each module has one horizontal

<b>Structure</b>	
Dimensions	3.0 m × 3.0 m × 1.7 m
Weight	15 tons
Number of Channels	14,336
<b>Scintillator Bars</b>	
Scintillator Material	Polystyrene, PPO(1%), POPOP(0.03%)
Dimensions	1.3 cm × 2.5 cm × 300 cm
Weight	1 kg
Emission Peak Wavelength	420 nm
Density	1.021 g/cm <sup>3</sup>
Bar Reflector Material	TiO <sub>2</sub> (15%) infused in polystyrene
<b>Wavelength Shifting Fibres</b>	
Type	Kuraray Y11(200)MS, multi-clad
Material	core - polystyrene, inner - acrylic outer - polyfluor
Refractive Index	core - 1.56, inner - 1.49, outer - 1.42
Absorption Peak Wavelength	430 nm
Emission Peak Wavelength	476 nm
Diameter	1.5 mm
Attenuation Length	350 cm
<b>MA-PMT</b>	
Model	Hamamatsu H8804
Anode	8×8 (2×2 mm <sup>2</sup> /pixel)
Cathode	Bialkali (Sb-K-Cs)
Sensitive wavelength	300-650 nm (peak at 420 nm)
Quantum efficiency	12% at 500 nm
Dynode	Metal Channel Structure, 12 stages
Gain	6×10 <sup>5</sup> at 800 V (typical)
Response Linearity	within 10% for 200 p.e. with gain~6×10 <sup>5</sup>
Cross-talk	3.15% (adjacent pixel)
<b>Readout Electronics</b>	
Number of ADC Channels	14,336
ADC Pedestal Width	below 0.3 photo-electrons
ADC Response Linearity	within 5% for 300 p.e. with gain~5×10 <sup>5</sup>
Number of TDC Channels	448
TDC Resolution	0.78 ns
TDC Full Range	50 μs

Table 4.1: Specifications of the SciBar Detector

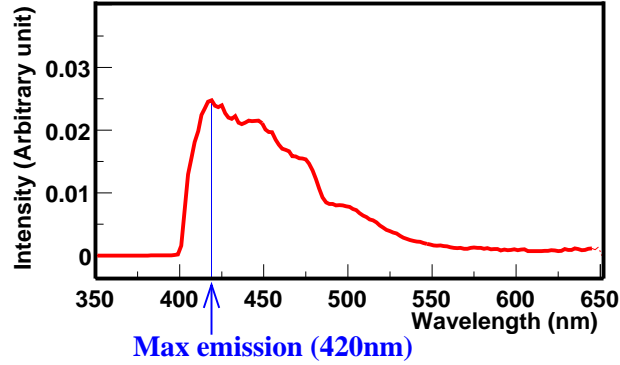


Figure 4.3: Typical scintillator bar emission spectrum.

and one vertical layer of 112 bars; modules are glued together with epoxy and held in place with an aluminium support frame. There are 64 modules in SciBar giving a total volume of  $3.0 \times 3.0 \times 1.7 \text{ m}^3$  and mass of 15 tonnes.

The light yield from scintillation is not proportional to the ionisation energy. There is a plateau in light yield as the ionisation energy increases. This is called scintillator quenching and is well described by Birk's Law [51].

$$\frac{\Delta E_{vis}}{\Delta E} \propto \frac{1}{1 + c \frac{dE}{dx}|_{exp}} \quad (4.1)$$

Where  $\frac{dE}{dx}|_{exp}$  is the expected energy loss per unit distance and  $c$  is Birk's constant.

Birk's constant is particular to each material. For SciBar it was measured by K2K using a small prototype detector in a proton beam. Figure 4.4 shows the K2K measurement with an extracted value for Birk's constant of  $0.0208 \pm 0.0003(\text{stat}) \pm 0.0023(\text{sys}) \text{ cm/MeV}$  [52].

### 4.1.2 Wavelength-Shifting Fibres

A 1.5 mm diameter Kuraray Y11(200)MS WLS fibre array sends the scintillation light to the MA-PMTs. The peak absorption wavelength for the WLS fibres is 430 nm, a good match to the peak scintillator bar emission wavelength of 420 nm. The WLS fibres re-emit the light with a peak wavelength of 476 nm, see figure 4.5. The vertical and horizontal fibre lengths are 335 cm and 360 cm respectively. The

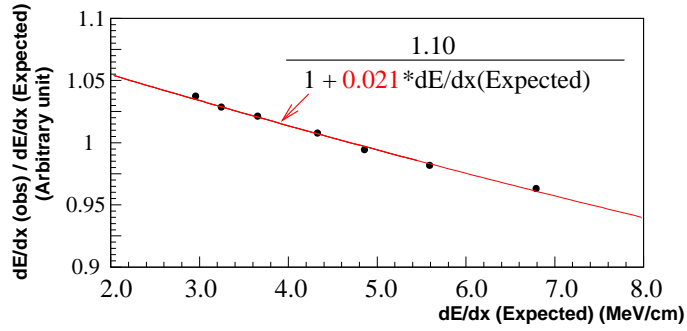


**Figure 4.4:** Ratio of visible energy loss to expected energy loss as a function of expected  $\frac{dE}{dx}$ . Measured using a prototype SciBar detector at KEK. The red line shows the best fit to the data.

average attenuation length of the fibres was measured to be 350 cm, compared with 10 cm for the scintillator bars, by the K2K group [53]. The attenuation lengths of a 4% sample of fibres were remeasured by SciBooNE. A 2% decrease in the attenuation length [46] was found compared to the K2K measurements. Each fibre has a polystyrene core (refractive index  $n = 1.56$ ) doped with a 220ppm concentration of wavelength-shifting fluor, an acrylic inner cladding ( $n = 1.49$ ) and an outer cladding of polyfluor ( $n = 1.42$ ). The fibres are bundled in groups of 64 and aligned with the MA-PMT pixels with a precision of 0.2 mm. SciBar has a total of 224 bundles.

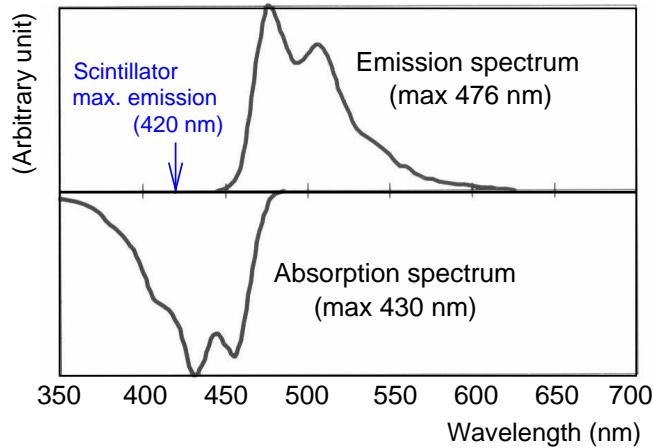


**Figure 4.5:** Absorption and emission spectra for a typical WLS fibre.

A cross-sectional schematic of the scintillator bar and WLS fibre is shown in figure 4.6.

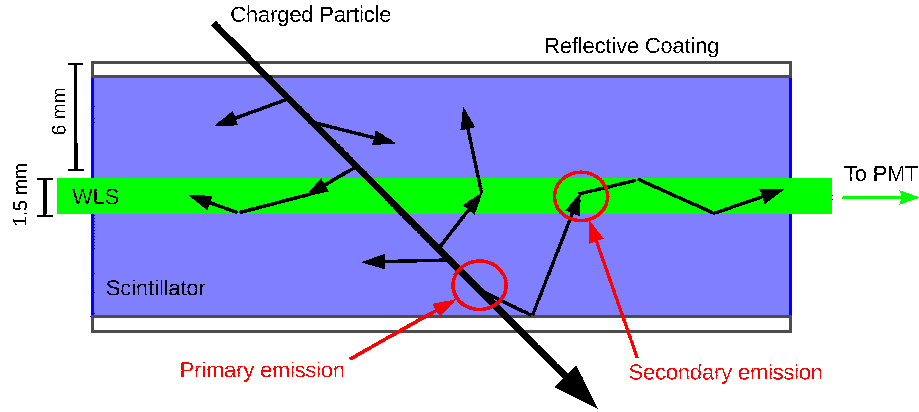


Figure 4.6: Cross-sectional schematic of a Scintillating bar and WLS fibre.

### 4.1.3 Multi-Anode Photo-Multiplier Tubes

The scintillation light is detected using Hamamatsu H8804 MA-PMTs. Each MA-PMT has 64 channels arranged in an  $8 \times 8$  array, with an individual pixel area of  $2 \times 2 \text{ mm}^2$ . The PMT cathode is bialkali with a 12% quantum efficiency at a wavelength of 500 nm. The gains of each MA-PMT channel were measured by the K2K experiment [54], with pixel-to-pixel gain variations of 20%. A high voltage of  $\sim 800 \text{ V}$  is required to achieve a gain of  $6 \times 10^5$  averaged over all 64 pixels for each MA-PMT. The gain stability is measured using the single photo-electron peak. The single photo-electron resolution is measured to be  $50 \pm 20\%$  determined from cosmic ray data [46]. This resolution is used in the MC simulation. The temperature dependence on the gain is 0.3% per degree Celsius, with the response linearity within 10% up to 200 photo-electrons with a gain of  $6 \times 10^5$ . The cross-talk between pixels on an MA-PMT is measured to be  $3.15 \pm 0.4\%$  for neighbouring channels [46]. The major source of cross-talk comes from light incident to the photo-cathode spreading amongst channels.

### 4.1.4 Readout Electronics

The readout electronics were developed by the K2K collaboration [55]. The electronics consist of a front-end board (FEB) attached to the MA-PMT and a back-end VME module attached to the FEB. The FEB electronics use VA/TA ASICs. The

VA is a 32-channel pre-amplifier chip with a shaper and multiplexer, and each TA provides multi-hit timing information using a 32-channel logical OR gate. Each FEB uses two VA/TA packages to read the 64-channel information and two timing signals for each MA-PMT. Each back-end VME module, originally developed for the ATLAS experiment [56], controls the readout from eight FEBs; there are 28 VME modules in total for SciBar. Flash ADCs are used to digitise the charge information with TDCs used to process the timing information. The readout system has low noise with a typical pedestal width of 0.3 photo-electrons. The TDC timing resolution and full range are 0.78 ns and 50  $\mu$ s, respectively.

#### 4.1.5 Gain Monitoring

An LED gain monitoring system is used in SciBar to monitor gain drifts on a channel-by-channel basis. A schematic of the gain monitoring system is shown in figure 4.7. Four blue light-emitting diodes (LEDs), monitored using PIN photodiodes, are used to produce the light signal. Each LED delivers light to 56 MA-PMTs through a clear fibre, with each MA-PMT having a light injection module attached to the WLS fibre bundle located in front of the MA-PMT cathode. The signal produced from the LED light mimics the scintillation signal well. The gain is monitored by comparing the signal measured by the MA-PMT with the signal measured by the PIN photodiode. The LED light stability and MA-PMT gain stability (see figure 4.8) were measured to be better than 2% with a measurement precision of 0.1%.

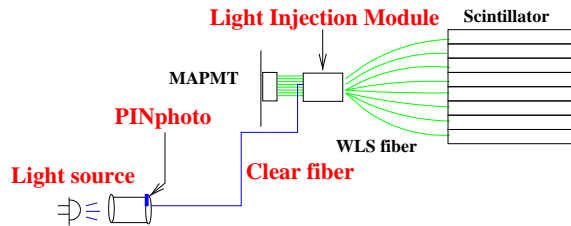
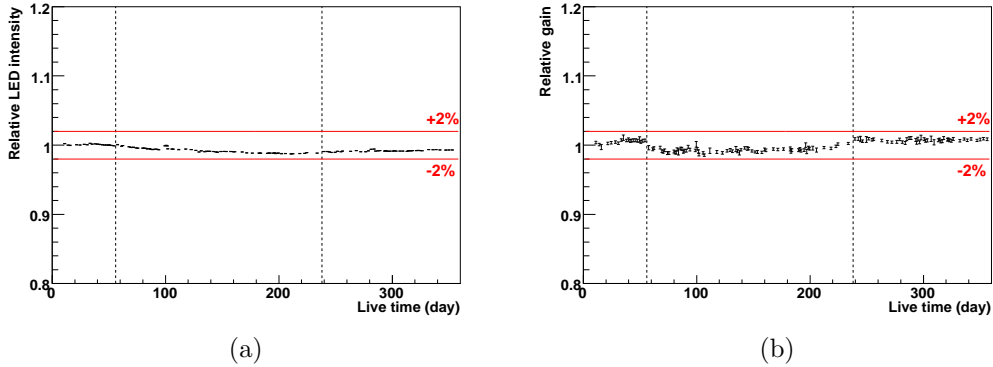


Figure 4.7: Schematic of the SciBar LED gain monitoring system.

#### 4.1.6 Energy Calibration

Cosmic muons are used to calibrate the energy scale in SciBar. The averaged light yield for a minimum ionising particle (MIP) is measured to be 20 photo-electrons per



**Figure 4.8:** (a) The LED intensity stability during the SciBooNE data run. The relative changes seen in the LED are corrected in the MA-PMT calibration. (b) A typical MA-PMT gain stability during the SciBooNE data run [46].

1.3 cm (the bar width) path length. Energy calibration constants, used to convert photo-electrons into visible energy are recorded for each channel with an average value of 8.1 p.e./MeV and a channel-to-channel variation of 20% [46].

## 4.2 The Electron-Catcher

Figure 4.9 shows a schematic of the EC detector. The EC is sandwiched between SciBar and the MRD and also enclosed within the SciBar dark-box. The detector is a ‘spaghetti’ calorimeter used to measure EM showers. The EC is principally used to identify EM showers from  $\nu_e$  interactions in SciBar, intrinsic in the neutrino beam, and a source of background to the MiniBooNE  $\nu_e$  appearance search, and tag photons produced from  $\pi^0$  decay. The EC was originally built for the  $\nu_\mu \rightarrow \nu_\tau$  CHORUS experiment at CERN [57, 58] before being used by the HARP experiment (CERN) and K2K experiment. Each ‘spaghetti’ module is comprised 21 lead foils and 740 scintillating fibres held together in a light-tight steel case. Each module is read out at both ends by two 1 inch Hamamatsu R1335/SM PMTs. Each module has dimensions  $262.0 \times 8.4 \times 4.2$  cm<sup>3</sup>. The EC consists of two layers, one horizontal and one vertical, of 32 modules for a surface area of  $2.7 \times 2.6$  m<sup>2</sup> and a total depth in the beam direction of 8.4 cm, equivalent to 11 radiation lengths (SciBar is 4 radiation lengths). An EC module cross-section can be seen in figure 4.10.

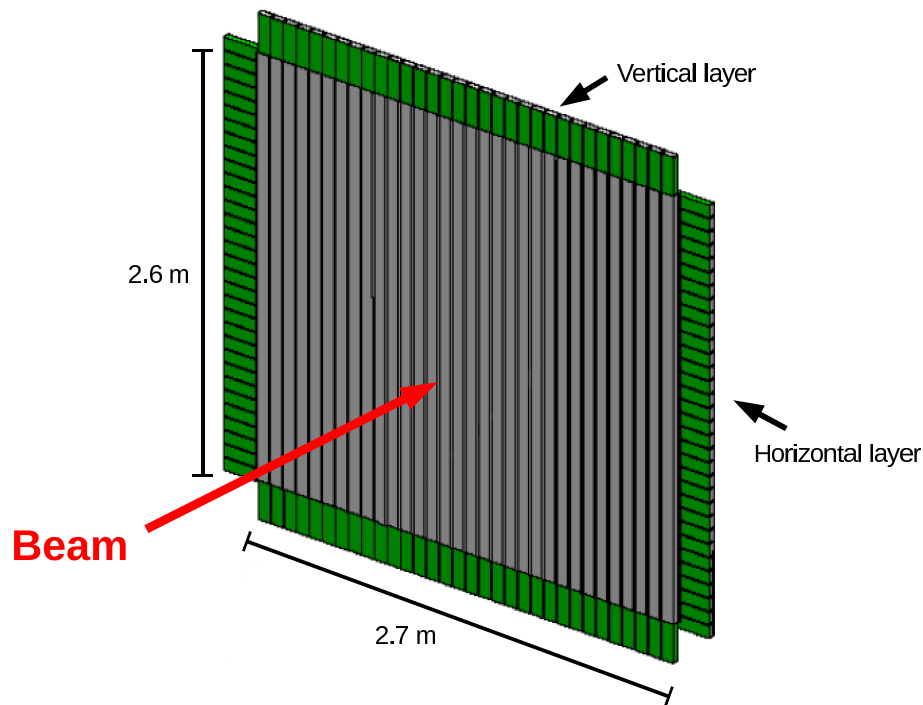


**Figure 4.9:** A schematic of the EC detector. The EC is a ‘spaghetti’ calorimeter consisting of two layers, one vertical and one horizontal, of 32 modules. With a thickness of  $11X_0$  the EC is used to measure EM showers.

The energy resolution for electrons is  $14\%/\sqrt{E(\text{GeV})}$  measured by the CHORUS experiment [59].

A summary of the EC’s specifications can be seen in table 4.2.

### 4.3 The Muon Range Detector

Figure 4.11 shows a schematic of the MRD detector. The MRD is the furthest downstream sub-detector in SciBooNE. The role of the MRD is to identify and reconstruct muon tracks and can stop muons with momenta up to  $1.2 \text{ GeV}/c$ . The MRD is the only new sub-detector in SciBooNE, though it is constructed from recycled materials used in past experiments. The MRD consists of 13, alternating X and Y, planes of scintillator paddles sandwiched between 12, 2 inch thick, iron plates, with dimensions  $274.0 \times 305.0 \times 5.1 \text{ cm}^3$ . The total mass of the MRD iron is approximately 48 tonnes. An additional iron plate, not used in the detector, was used to calculate the iron density by taking a series of measurements from multiple

Structure	
Dimensions	270 cm × 260 cm × 8.4 cm
Number of Channels/Plane	32
Number of Planes	2
'Spaghetti' Modules	
Absorber	1.9 mm Pb foils (21/module)
Scintillating Fibres	Kuraray SCSF81 (740/module)
Dimensions	262.0 cm × 8.4 cm × 4.2 cm
PMTs	
Type	1 inch Hamamatsu R1335/SM (4/module)
Number of PMTs	256
Cathode	Bialkali
Quantum Efficiency	27% at 350-450 nm
Gain	$2 \times 10^6$ at 1600 V (typical)

Table 4.2: Specifications of the EC Detector.

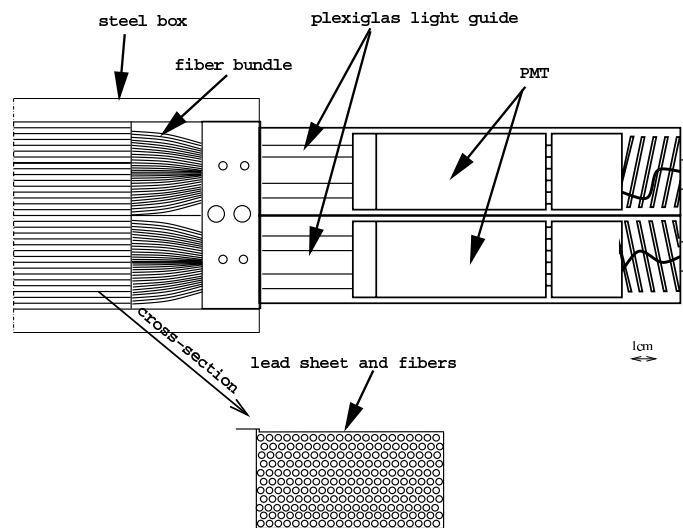
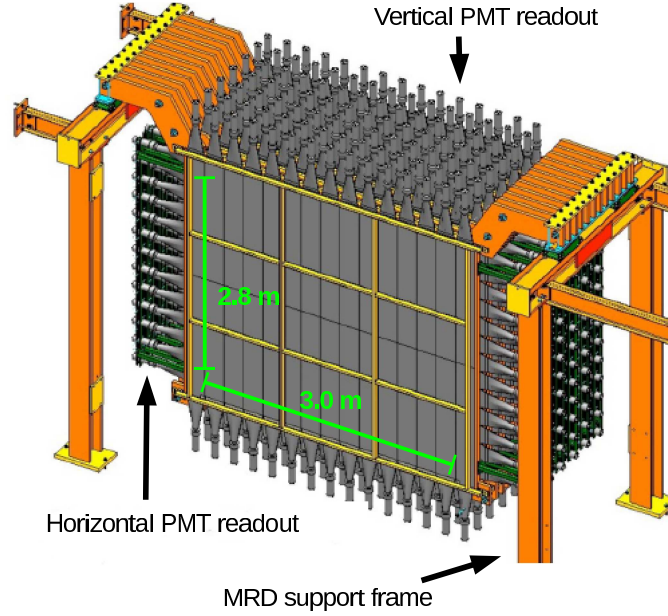


Figure 4.10: Cross-section schematic of EC module.



**Figure 4.11:** A schematic of the MRD detector. The MRD consists of 362 scintillator paddles arranged in thirteen alternating horizontal and vertical layers separated by 12, 2 inch thick, iron plates. The detector is able to range out muons with momenta less than 1.2 GeV/c.

locations on the sheet. The density was measured to be  $7.841 \pm 0.002 \text{ g/cm}^3$ . The thickness of the iron plates was found to be uniform to a precision of 1%. There are 362 scintillator paddles in the MRD. The scintillator was originally used in the E605 experiment at Fermilab [60]. One horizontal scintillator layer consists of 26 scintillator paddles, arranged in a  $2 \times 13$  array, with an active area of  $260 \times 300 \text{ cm}^2$ . For a vertical layer 30 scintillator paddles are used, arranged in a  $2 \times 15$  array, with an active area of  $276 \times 300 \text{ cm}^2$ . Each horizontal scintillator paddle is  $155 \times 20 \times 0.6 \text{ cm}^3$ , each vertical paddle is  $138 \times 20 \times 0.6 \text{ cm}^3$ .

Five different types of 2" PMTs are used in the MRD. 10-stage Hamamatsu 2154-05 and RCA 6342A PMTs are used for the vertical planes. The Hamamatsu PMTs were originally used in the NuTeV experiment. 14-stage EMI 9954KB, 9839b, and 9939b PMTs are used for the horizontal planes. The EMI 9954KB PMTs were originally used in the KTeV experiment. All planes were powered with negative high-voltage except the 9939b plane which was powered with positive high voltage. Charge and timing information for each channel are recorded, using LeCroy 4300B ADCs and LeCroy 3377 TDCs. The timing resolution and full range are 0.5 ns and 32  $\mu\text{s}$ , respectively. The energy threshold for TDC hits is approximately 250 keV,

corresponding to 20% of the signal from a minimum ionising particle passing through a paddle. The single noise rate is typically 100 Hz for the horizontal planes and less than 10,000 Hz (RCA PMTs) for the vertical planes.

The MRD uses an independent cosmic ray trigger from the SciBar and EC detectors. These cosmic data were used to monitor the hit-finding efficiencies for all paddles in the detector. Figure 4.12 shows a typical hit finding efficiency plot for a half-plane in the MRD; the average hit-finding efficiency is 99%. The main source of inefficiency comes from the gaps between counters which are typically 0.5 cm.

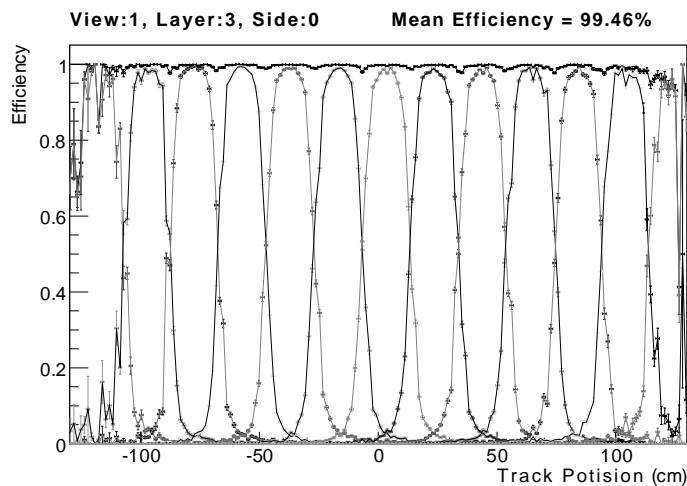


**Figure 4.12:** Hit finding efficiency for a typical MRD half-plane using cosmic data. Both the individual counter and summed efficiencies are shown. The typical efficiency is around 99% [61].

A summary of the MRD's specifications can be seen in table 4.3.

### 4.3.1 Scintillator Paddle Prototype: Construction and Testing

Studies done during the proposal period of SciBooNE concluded that the hit-finding efficiency for all scintillator paddles in the MRD had to be greater than 95%. Since each paddle was to be constructed from used materials, including the scintillator and PMTs, the hit-finding efficiency had to be determined. Two prototype paddles, one vertical and one horizontal, were built and tested using cosmic data and a 3-fold to 4-fold coincidence, using 4" thick iron blocks to remove cosmic ray muons

<b>Iron Plates</b>	
Number of Plates	12
Dimensions	$274.0 \times 305.0 \times 5.1 \text{ cm}^3$
Density	$7.841 \text{ g/cm}^3$
<b>Scintillator Panels</b>	
Number of Planes	13 (7 horizontal, 6 vertical)
Number of Paddles/Plane	$2 \times 13$ (horizontal), $2 \times 15$ (vertical)
Dimensions (Scintillator)	thickness: 0.6 cm, width: 20 cm length: 155 cm (horizontal) length: 138 cm (vertical)
Light-Guide Dimensions (trapezoid)	max. (min.) width: 17.1 cm (5.1 cm) thickness: 0.5 cm, length: 33.3 cm
Electro-Static Shielding	outer: Marvelguard, inner: mylar
<b>2" PMTs</b>	
Vertical Models	Hamamatsu 2154-05, RCA 6342A
Horizontal Models	EMI 9954KB, 9839b and 9939b
Dynode	14 stage (horizontal) 10 stage (vertical)
Gain	$\sim 1 \times 10^6$ at 2000 V (horizontal) $\sim 1 \times 10^6$ at 1200 V (vertical)
<b>Readout Electronics</b>	
Number of Channels	362
ADC	LeCroy 4300B
TDC	LeCroy 3377
TDC resolution	0.5 ns
TDC Full Range	32 $\mu\text{s}$

**Table 4.3:** Specifications of the Muon Range Detector

with energies below  $\sim 100$  MeV. A schematic of the cosmic stand can be seen in figure 4.13. Before the counters were constructed the dark rate and 1 p.e. response

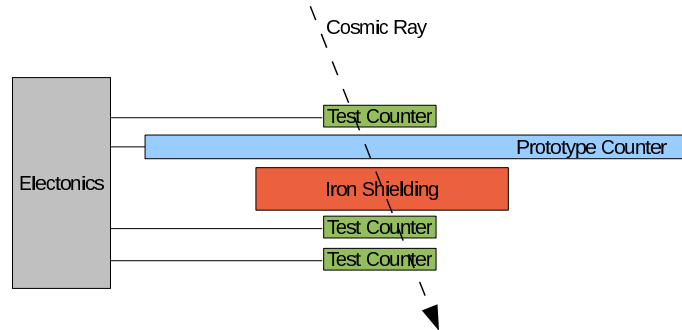


**Figure 4.13:** Schematic of the cosmic test stand.

for each PMT was tested. Both prototype counters were found to have efficiencies greater than 99% once operating at their plateau voltage (see figure 4.14). The

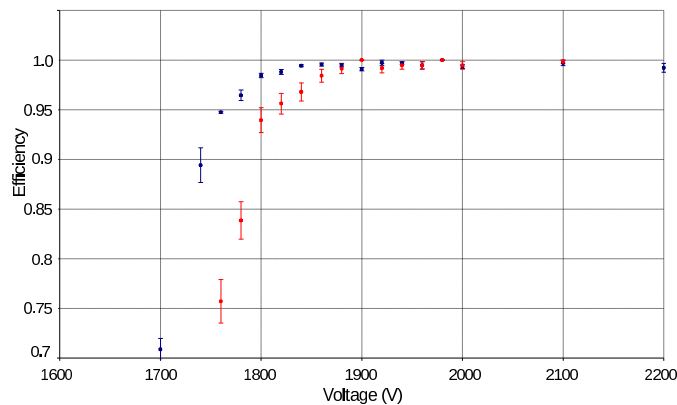


**Figure 4.14:** Plateau curves for two prototype counters (red and blue) determined using cosmic ray data. The red counter has a higher operating voltage. Both counters have hit-finding efficiencies above 99% once on the plateau.

efficiency as a function of position was measured at three positions, (12 cm, 65 cm, and 96 cm from the non-PMT end), using cosmic ray data. The efficiency of each counter was found to be independent of position when operating at their plateau voltage (see figure 4.15). With the prototype counters operating at their plateau voltage, a current reading was taken when exposed to the Cs-137 source positioned at 65 cm from the non-PMT end of the paddle. During full-scale production of the MRD counters each counter was exposed to the Cs-137 source and the voltage increased until the corresponding current readout was achieved. If the operating

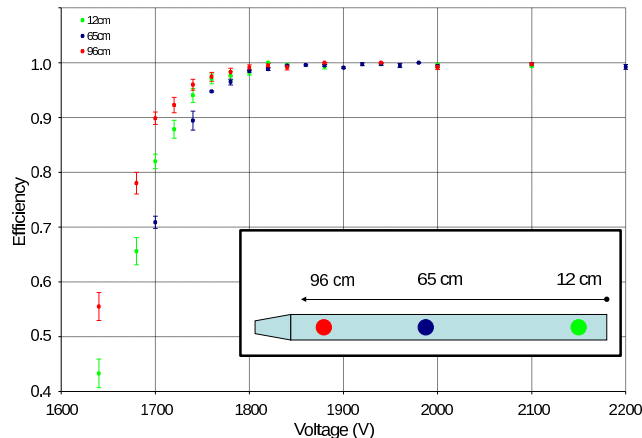


**Figure 4.15:** Plateau curves for three positions on the prototype counter determined using cosmic ray data. The least efficient point on the counter is at 65 cm. Once the counter is on the plateau the position has no effect on the hit-finding efficiency.

voltage exceeded the specifications for the PMT, the counter was rejected. Table 4.4 shows the quantity and operating voltages for the five PMT flavours used in the SciBooNE detector. All operating voltages were re-measured using cosmic data during the commissioning of the detector.

PMT	Max. Voltage	Number
EMI 9954KB	2400	134
EMI 9939B	2400	26
EMI 9839B	2400	22
RCA 6392A	1500	80
Hamamatsu R2154-05	1600	100

**Table 4.4:** Scintillator paddle PMT inventory.

## 4.4 Data Acquisition

SciBooNE has two triggers, an on-beam trigger and an off-beam trigger. The on-beam trigger records all events in the beam window, the off-beam trigger is used to record all calibration data. The trigger cycle is defined by the accelerator timing sequence. During the accelerator supercycle the BNB receives one train of proton pulses with a maximum of 10 pulses per cycle. A typical cycle lasts approximately 2 seconds. The on-beam trigger is started by a fast timing signal sent from the BNB

extraction magnet. The off-beam trigger immediately follows the on-beam trigger. During the off-beam trigger, each sub-detector takes pedestal and cosmic ray data. Additionally SciBar monitors the relative gains over all channels using the LED gain-monitoring system. Pedestal and LED data are recorded once per cycle. SciBar and the EC use a common cosmic trigger generated using a fast signal from the TA. The MRD has a separate cosmic trigger, using the discriminator outputs from selected layers in the MRD. Both SciBar and the MRD record 20 cosmic triggers per cycle.

---

# Chapter 5

## Simulation

In this chapter the beam simulation, neutrino-nucleon interactions and detector simulation and response are described.

### 5.1 Beam Simulation

The beam flux is modelled using a Monte-Carlo simulation developed by the Mini-BooNE collaboration [62], the simulation uses the GEANT4 framework [63].

#### 5.1.1 Meson Production Simulation

The geometry and materials present in the Booster neutrino beam (BNB) target hall and decay region are simulated. The proton beam is simulated according to the expected beam optic properties; these are based on measurements made by the BNB monitoring systems. The proton-beryllium interactions are simulated using hadronic interaction data. The products of these interactions, so-called secondary particles, such as protons, neutrons, charged pions, and kaons, are simulated as they travel through the target. Elastic and quasi-elastic scattering of the primary protons is also simulated. Of particular importance to the neutrino flux prediction is  $\pi^+$  production from p-Be interactions. Data from the HARP [64] and BNL E910 [65] experiments is used in the simulation of this process.

---

The Sanford-Wang parametrisation [66] is used to calculate the double differential cross-section for  $\pi^+$ ,  $\pi^-$  and  $K^0$  production.

$$\frac{d^2\sigma}{dpd\Omega} = C_1 p^{C_2} \left(1 - \frac{p}{p_B - C_9}\right) \exp\left(-C_3 \frac{p^{C_4}}{p_B^{C_5}} - C_6 \theta (p - C_7 p_B \cos^{C_8} \theta)\right) \quad (5.1)$$

Where  $p$  and  $p_B$  are the meson momentum and incident proton momentum, respectively.  $\theta$  is the meson angle with respect to the incident proton direction, and  $C_1 - C_9$  are parameters determined by the experimental data. The Sanford-Wang parameter values used in the simulation are summarised in table 5.1.

	$C_1$	$C_2$	$C_3$	$C_4$	$C_5$	$C_6$	$C_7$	$C_8$	$C_9$
$\pi^+$	220.7	1.080	1.000	1.978	1.320	5.572	0.0868	9.686	1
$\pi^-$	213.7	0.9379	5.454	1.210	1.284	4.781	0.07338	8.329	1
$K_S^0$	15.130	1.975	4.084	0.928	0.731	4.362	0.048	13.300	1.278

**Table 5.1:** Sanford-Wang parameters for  $\pi^+$ ,  $\pi^-$  and  $K_S^0$  production.

Since no measurements of  $K^+$  production has been made at BNB energies, Feynman scaling is employed to relate experimental data at higher energies to the BNB energy range. For the Feynman scaling hypothesis only two variables are needed to describe the double differential cross-section for  $K^+$  production. These are the transverse component of the kaon momentum,  $p_T$ , and the Feynman scaling factor,  $x_F = \frac{p_{||}}{p_{||}^{max}}$ , defined as the ratio of parallel component of the kaon momentum,  $p_{||}$ , and the maximum value of this quantity for a given reaction,  $p_{||}^{max}$ . Both are considered in the centre-of-mass frame. The double differential cross-section can then be written as

$$\frac{d^2\sigma}{dpd\Omega} = \frac{p^2}{E^2} C_1 (1 - |x_F|) \exp(-C_2 p_T - C_3 |x_F|^{C_4} - C_5 p_T^2 - C_7 |p_T \times x_F|^{C_6}) \quad (5.2)$$

Where  $p$  and  $E$  are the meson momentum and energy, respectively. The Feynman scaling parameter values used in the simulation are summarised in table 5.2.

	$C_1$	$C_2$	$C_3$	$C_4$	$C_5$	$C_6$	$C_7$
$K^+$	11.70	0.88	4.77	1.51	2.21	2.17	1.51

**Table 5.2:**  $K^+$  Feynman scaling parameters.

### 5.1.2 Meson Decay Simulation

A FORTRAN-based Monte-Carlo originally developed by the MiniBooNE collaboration uses the output from the GEANT4 program as the input to simulate meson decays producing the neutrino beam. The FORTRAN code simulates pion and muon decays to generate neutrino kinematic distributions which are used to obtain the final neutrino fluxes that are extrapolated to produce the SciBooNE flux prediction. Table 5.3 outlines the branching fractions for meson and muon decays.

Particle	Lifetime (nsec)	Decay Mode	Branching Ratio (%)
$\pi^+$	26.03	$\mu^+\nu_\mu$	99.9877
		$e^+\nu_e$	0.0123
$K^+$	12.39	$\mu^+\nu_\mu$	63.44
		$\pi^0 e^+\nu_e$	4.98
		$\pi^0 \mu^+\nu_\mu$	3.32
$K^0$	51.6	$\pi^- e^+\nu_e$	20.333
		$\pi^+ e^-\bar{\nu}_e$	20.197
		$\pi^- \mu^+\nu_\mu$	13.551
		$\pi^+ \mu^-\bar{\nu}_\mu$	13.469
$\mu^+$	2197.03	$e^+\nu_e\bar{\nu}_\mu$	100

**Table 5.3:** Meson and muon neutrino producing decay modes considered in the simulation. The corresponding anti-particle decays are also considered.

### 5.1.3 Neutrino Flux Prediction

The neutrinos produced from meson decay are propagated along straight lines into the SciBooNE detector. The neutrino production information, including parent type, neutrino flavour, kinematics and neutrino path across the SciBooNE detector are stored. The neutrino path across the detector is used to reconstruct the neutrino direction and interaction point. Each neutrino event within the detector is given a proper weight which is calculated given the above beam information as well as the neutrino interaction type and detector simulation, which includes the detector response and the specifics of the detector geometry. Figure 5.1 shows the flux predictions for neutrino (5.1(a)), and antineutrino (5.1(b)) running as a function of neutrino energy. In neutrino mode the total neutrino flux per proton on target

through the SciBooNE detector is  $2.2 \times 10^{-8} \text{ cm}^{-2}$ , with a 93% purity of muon neutrinos, a 6.4% muon antineutrino background, and a 0.6% electron neutrino and antineutrino background. In antineutrino mode the neutrino flux per proton on target is  $1.3 \times 10^{-8} \text{ cm}^{-2}$ , with 84% muon anti-neutrinos, 15.3% muon neutrinos and 0.7% electron neutrino and antineutrinos.

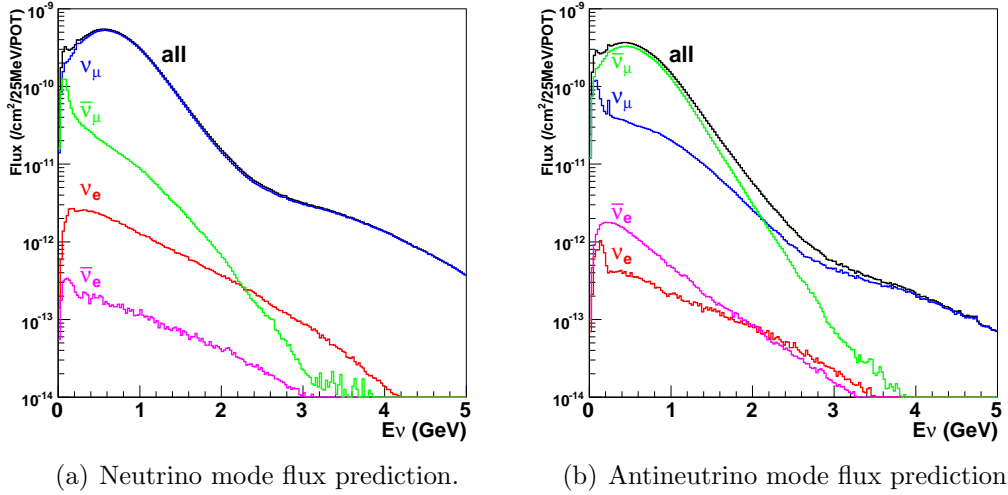


**Figure 5.1:** Neutrino flux predictions at the SciBooNE detector as a function of neutrino energy,  $E_\nu$ , normalised per unit area, protons on target and neutrino energy bin width, in neutrino mode (left) and antineutrino mode (right). The spectra are averaged within 2.12 m from the beam centre. The total flux and contributions from individual neutrino flavours are shown.

#### 5.1.4 Beam Flux Systematic Uncertainties

There are four major sources of systematic uncertainty in the beam production simulation, a detailed description of these uncertainties can be found in [62].

#### Proton Delivery

The number of neutrino events predicted in SciBooNE is directly proportional to the number of protons on target. The uncertainty in the proton beam intensity and the proton beam optics are 2% and 1%, respectively.

## Secondary Particle Production

The uncertainty in the cross-sections for p-Be interactions affect the rate and spectrum of the neutrinos. As highlighted in section 5.1.1 the Sanford-Wang parametrisation is used to model the  $\pi^\pm$  and  $K^0$  productions and Feynman scaling is used to model  $K^+$  production. The uncertainty in the secondary particle production is the major source of uncertainty in the neutrino flux.

## Hadronic Interactions in the Target and Horn

Uncertainties due to the rate of hadronic interactions affect both the rate and shape of the neutrino flux. Variations in the total hadronic cross-section, the quasi-elastic and inelastic cross-sections for nucleon, and pion, interactions on both beryllium and aluminium are accounted for.

## Horn Magnetic Field

Uncertainties in the horn magnetic field result in spectral distortions of the neutrino flux. The uncertainty in the horn current is  $\pm 1$  kA, and the uncertainty in modelling the current within the inner cylinder is also accounted for.

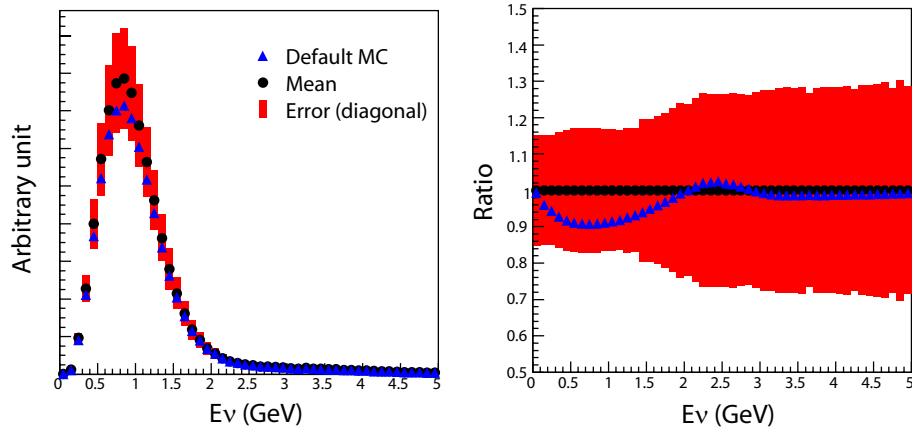


**Figure 5.2:** (left) Systematic uncertainty in the neutrino energy distribution for muon neutrino interactions. (right) The fractional uncertainty as a function of neutrino energy.

Figure 5.2 shows the muon neutrino energy distribution prediction for SciBooNE events, including the systematic error (red error band). The estimated error in the

number of neutrino interactions in SciBooNE is 15%, with the dominant source of error,  $\pi^+$  production, accounting for 14%.

## 5.2 Neutrino-Nucleus Interactions

SciBooNE uses NEUT [67, 68]; a neutrino interaction simulation software package. NEUT was originally developed for the Kamiokande experiment and is also used by Super-Kamiokande, K2K and T2K.

The NEUT program libraries handle the neutrino-nucleus interactions. NEUT has the capability to simulate neutrino interactions on hydrogen, carbon, oxygen and iron with energies from 100 MeV to 100 TeV, as well as re-interactions of the mesons and hadrons with the nuclear medium. The output of the beam simulation (see section 5.1) is used as the input to NEUT. NEUT models five different interactions for both charged current (CC) and neutral current (NC) events

- Quasi-elastic scattering -  $N\nu \rightarrow N'l$
- Single meson production -  $N\nu \rightarrow N'lm$
- Single photon production -  $N\nu \rightarrow N'l\gamma$
- Coherent pion production -  $^{12}C\nu \rightarrow ^{12}Cl\pi$
- Deep inelastic scattering -  $N\nu \rightarrow N'l + nH$

Where  $N$  and  $N'$  are nucleons (proton or neutron),  $l$  is the lepton,  $\nu$  the incident neutrino and  $m$  is the meson. Figure 5.3 show the cross-sections, normalised by neutrino energy, for each interaction mode as simulated by NEUT. Table 5.4 shows a breakdown of the expected number of  $\nu_\mu$  events for each interaction mode in NEUT.

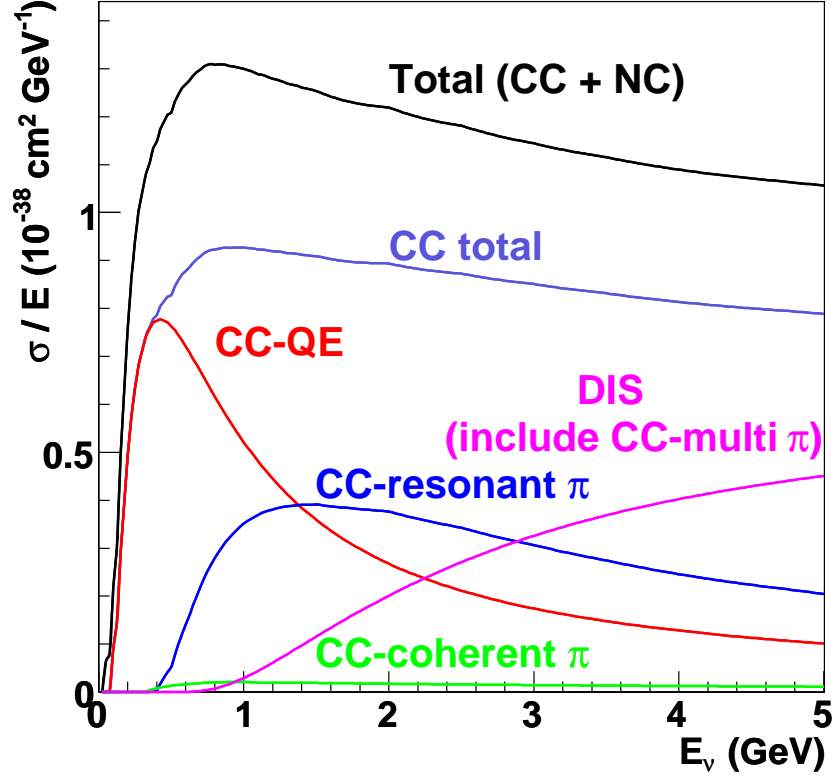


Figure 5.3: NEUT simulated cross-sections normalised by neutrino energy for each interaction mode for  $M_A = 1.2$  GeV. [46]

Mode	$\nu_\mu$ interactions (10 tons/ $10^{20}$ POT)
CCQE	50,800
CC $\pi_{res}$	26,200
CC DIS	6,300
CC $\pi_{coh}$	1,700
NC Elastic	21,400
NC $\pi_{res}$	10,400
NC DIS	2,000
NC $\pi_{coh}$	1,000

Table 5.4: Number of  $\nu_\mu$  interactions in SciBooNE for the NEUT MC.

### 5.2.1 Quasi-Elastic Scattering

Quasi-Elastic (QE) scattering is the dominant interaction mode for the neutrino energy range at SciBooNE. NEUT uses the Llewellyn-Smith formulation to model quasi-elastic interactions [42] with the hadronic current,  $J_\lambda$ , expressed as:

$$\langle p | J_\lambda | n \rangle = \cos \theta_c \bar{u}(p) \left[ \gamma_\lambda F_V^1(Q^2) + \frac{i\sigma_{\lambda\nu} q^\nu \xi F_V^2(Q^2)}{2m_N} + \gamma_\lambda \gamma_5 F_A(Q^2) \right] u(n) \quad (5.3)$$

Where  $\theta_c$  is the Cabibbo angle,  $m_N$  is the nucleon mass,  $Q^2$  is the lepton momentum transfer, and  $\xi = \mu_p - \mu_n = 3.71$ , is the difference in the proton and neutron magnetic moments.  $F_V^i$  are the vector form factors and  $F_A$  is the axial form factor.  $F_A$  assuming a dipole form (this can be modified if the data prefers it) is given by

$$F_A(Q^2) = \frac{g_A}{\left(1 - \frac{Q^2}{M_A^2}\right)^2} \quad (5.4)$$

where  $g_A = -1.23$  is determined from neutron decay measurements. In NEUT we set  $M_A$  to be  $1.21 \text{ GeV}/c^2$  as measured by recent experiments [69, 70].

The differential cross-section is

$$\frac{d\sigma}{dQ^2} = \frac{m_N^2 G_F^2 \cos^2 \theta_c}{8\pi E_\nu^2} \left[ A(Q^2) \mp B(Q^2) \frac{s-u}{m_N^2} + C(Q^2) \frac{(s-u)^2}{m_N^4} \right] \quad (5.5)$$

Where  $E_\nu$  is the incident neutrino energy;  $s$  and  $u$  are Mandelstam variables and  $s-u \equiv 4m_N E_\nu - Q^2 - m_l^2$ ;  $m_l$  is the mass of the outgoing lepton. The three terms  $A(Q^2)$ ,  $B(Q^2)$  and  $C(Q^2)$  are

$$\begin{aligned} A(Q^2) = & \frac{m_l^2 + Q^2}{4m_N^2} \left[ \left(4 + \frac{Q^2}{m_N^2}\right) |F_A|^2 - \left(4 - \frac{Q^2}{m_N^2}\right) |F_V^1|^2 \right. \\ & + \frac{Q^2}{m_N^2} |\xi F_V^2|^2 \left(1 - \frac{Q^2}{m_N^2}\right) + \frac{4Q^2 F_V^1 \xi F_V^2}{m_N^2} \\ & \left. - \frac{m_l^2}{m_N^2} (|F_V^1 + \xi F_V^2|^2 + |F_A|^2) \right] \end{aligned} \quad (5.6)$$

$$B(Q^2) = -\frac{Q^2}{m_N^2} F_A (F_V^1 - \xi F_V^2) \quad (5.7)$$

$$C(Q^2) = \frac{1}{4} \left[ |F_A|^2 + |F_V^1|^2 + \frac{Q^2}{m_N^2} \left| \frac{\xi F_V^2}{2} \right|^2 \right] \quad (5.8)$$

The neutral current cross-sections can be obtained from the charged-current cross-section using the following relations [71, 72].

- $\sigma(\nu p \rightarrow \nu p) = 0.153 \times \sigma(\nu n \rightarrow \mu^- p)$
- $\sigma(\bar{\nu} p \rightarrow \bar{\nu} p) = 0.208 \times \sigma(\bar{\nu} p \rightarrow \mu^+ p)$
- $\sigma(\nu n \rightarrow \nu n) = 1.5 \times \sigma(\nu p \rightarrow \nu p)$
- $\sigma(\bar{\nu} n \rightarrow \bar{\nu} n) = \sigma(\bar{\nu} p \rightarrow \bar{\nu} p)$

The relativistic Fermi gas model [73] is used to model nucleon rescattering in the nucleus. The Fermi motion and Pauli exclusion principle is also taken into account. The momentum of the target nucleon is assumed to be flat with a momentum of 217 MeV/c and 250 MeV/c for carbon and iron, respectively. The nuclear potential is 27 MeV and 32 MeV for carbon and iron, respectively.

### 5.2.2 Single Meson Production

Single meson production is the second most abundant process in SciBooNE after quasi-elastic scattering. Single meson production from baryonic resonances is simulated using the Rein and Sehgal model [74].

$$\begin{aligned} \nu N &\rightarrow l N^* \\ N^* &\rightarrow N' \pi \end{aligned} \quad (5.9)$$

Where  $N$  and  $N'$  are the nucleons and  $N^*$  is the baryonic resonant state.

Equation 5.10 is the double differential cross-section for single meson production. The cross-section is dependent on the amplitude of the baryonic resonance and the probability that the baryonic resonance will decay to a meson.

$$\frac{d^2\sigma}{dQ^2 dW} = \frac{1}{32\pi m_N E_\nu^2} \times \frac{1}{2} \sum_{spins} |T(\nu N \rightarrow l N^*)|^2 \times \delta(W^2 - M^2) \quad (5.10)$$

Where  $Q^2$  is the momentum transfer,  $W$  is the invariant mass of the baryon,  $m_N$  is the nucleon mass, and  $E_\nu$  is the incident neutrino energy.  $T(\nu N \rightarrow l N^*)$  is the amplitude of a given resonance. The vector and axial form factors are modelled using a dipole parametrisation, identical to that used for quasi-elastic scattering.

The  $\delta$ -function can be replaced by the Breit-Wigner factor for resonances with finite width.

$$\delta(W^2 - M^2) \rightarrow \frac{1}{2\pi} \frac{\Gamma}{(W - M)^2 + \Gamma^2/4} \quad (5.11)$$

Rein and Sehgal's method [75] is used to model the pion angular distribution in the final state for the  $P_{33}(1232)$  resonance. For all other resonances the pion angular distribution is isotropic in the resonance rest frame. The angular distribution for  $\nu p \rightarrow \mu^- p \pi^+$  has been measured by experiment [34], and agrees well with the NEUT prediction.

### 5.2.3 Coherent Pion Production

Coherent pion production is a neutrino interaction with a nucleus where the nucleus remains intact and a single pion exists in the final state, with the same charge as the boson involved in the interaction. The Rein and Sehgal model with the lepton mass correction included [76, 77], and the Paschos *et al.* model [78] are used to simulate coherent pion production. The SciBooNE measurement [49] set an 90% confidence limit on charged-current coherent pion production. This limit is a third of the NEUT default value, and is used in this analysis.

### 5.2.4 Intra-Nuclear Interactions

The intra-nuclear interactions are simulated in NEUT using a cascade model with the path of each particle tracked, until it escapes the nucleus. A Woods-Saxon type nucleon density is used to simulate the neutrino interaction position within the nucleus.

$$\rho(r) = \frac{Z}{A} \rho_0 \left[ 1 + e^{\frac{r-c}{a}} \right]^{-1} \quad (5.12)$$

where  $\rho_0 = 0.48m_\pi^3$  is a constant; A and Z are the mass number and atomic number of the nucleus, respectively. For a carbon nucleus  $a = 0.52$  fm and  $c = 2.36$  fm [79]. The Fermi motion of nucleons and the Pauli blocking effect are also taken into account. The Fermi surface momentum at the interaction point is

$$p_F(r) = \left( \frac{3}{2} \pi^2 \rho(r) \right)^{\frac{1}{3}} \quad (5.13)$$

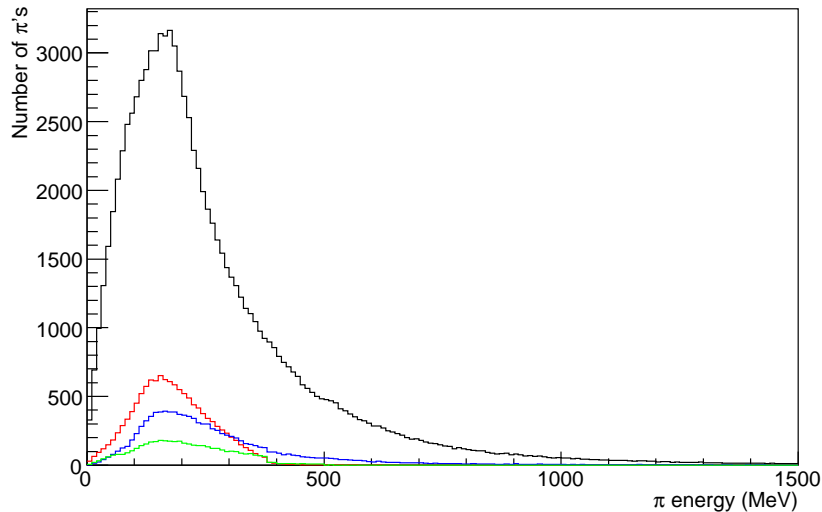


**Figure 5.4:** Fate of charged pions from  $\nu_\mu$ -carbon interactions inside the nucleus as simulated by NEUT. All pions simulated (black line), pion absorption (red line), inelastic scattering (blue line), charge exchange (green line).

### 5.2.5 Pion Interactions and Nucleon Rescattering

Pion interactions and nucleon rescattering inside the nucleus are important processes for this analysis. Pion absorption, inelastic scattering and charge exchange are simulated in NEUT, with the cross-sections derived from the Salcedo model [80]. An uncertainty on the cross-sections of 30% is estimated using experimental data [81]. Figure 5.4 shows all the events in the SciBooNE MC containing a pion. The fraction of events that are absorbed, inelastically scatter or undergo charge exchange are also highlighted. Approximately 15% of pions produced are absorbed, 20% inelastically scatter and 5% undergo charge exchange.

Re-interactions of the nucleons can also happen. Elastic scattering and pion production are simulated using the cascade model with the differential cross-sections taken from nucleon-nucleon scattering experiments [82]. Approximately 35% of protons from CCQE interactions rescatter in carbon.

---

## 5.3 Detector Simulation

The detector is simulated using the GEANT4 framework. Each sub-detector and support structures, detector hall and surrounding soil are simulated using data from survey measurements made during the construction phase of SciBooNE.

### 5.3.1 Particle Simulation in the Detectors

The Bertini cascade model in GEANT4 [83] is used to simulate hadronic interactions within the detectors. The motion of bound nucleons, the Pauli exclusion principle and a local potential for nucleons and pions are included in the model. Experimental data from several experiments are used to define the nucleon-nucleon and nucleon-pion cross-sections.

### 5.3.2 Detector Response

For SciBar the NEUT output is used as the input for the detector simulation. The energy lost by a particle in each scintillator bar is modelled by GEANT, with the energy scaling tuned using cosmic data taken during the SciBooNE run. Scintillator quenching is simulated using Birk's law [51] with a value for Birk's constant of  $0.0208 \pm 0.0035$  cm/MeV with the error considered in the systematics. The energy deposited in SciBar is converted into photo-electrons using conversion factors derived from cosmic ray data taken during the SciBooNE run. The average attenuation length of the WLS fibres is simulated with a value of 350 cm, determined from measurements made by the K2K collaboration [53]. The cross-talk between neighbouring channels on an MA-PMT is also simulated. The cross-talk was measured to be  $3.15 \pm 0.4\%$ . The number of photo-electrons is smeared using Poisson statistics and is then converted into ADC counts. The MA-PMT single photo-electron resolution is also simulated. Electronic noise and threshold effects of the TA are also simulated. Light propagation delays in the WLS fibres are accounted for in the TDC simulation. Additionally, a logical OR gate is included for the 32 channels on an MA-PMT, with multiple TDC hits also simulated.

---

For the EC, the true energy deposition is converted into photo-electrons using conversion factors derived from cosmic ray data and the measured average attenuation length for the fibres is also simulated. The number of photo-electron hits is smeared using Poisson statistics and is then converted into ADC counts. The time-dependent ADC gain due to overshoot of the PMT signal is simulated using cosmic ray data. The ADC window is centred on the beam window; therefore the same energy deposit at different times will produce different ADC values, this is also accounted for in the simulation. Finally electronic noise is also simulated.

The true energy deposition in each scintillator paddle for the MRD is converted into ADC counts using conversion factors derived from cosmic ray data; additionally the energy deposition time is digitised and converted into a TDC hit. Light attenuation in the scintillator paddles and electronic noise are also simulated. Gaps between each scintillator bar are also taken into account.

### 5.3.3 Dirt and EC-MRD Interaction Simulations

Neutrino interactions within the ground surrounding the detector hall occasionally produce particles which penetrate the SciBooNE detector depositing energy. These events are called ‘dirt events’ and are a background to all neutrino cross-section studies. In an NC elastic study these events are a prominent background because of dirt neutrons entering the detector and interacting producing a proton track; this is an irreducible background. Dirt events producing muons are the main dirt background to the CCQE analyses. A number of cuts can be applied to reduce this background; these are described in more detail in chapter 8. An MC simulation of dirt events is used to estimate the background using the beam simulation, NEUT MC and detector simulation. The beam simulation is extended to cover a  $10 \times 10 \times 10 \text{ m}^3$  cube, centred on the detector origin. Figure 5.5 shows a schematic of this region, with the grey areas representing the dirt. NEUT is used to simulate the neutrino interactions; carbon is used as the material for the dirt with a density  $\rho = 2.15 \text{ g/cm}^3$ . Particles are then propagated using GEANT4; concrete is used as

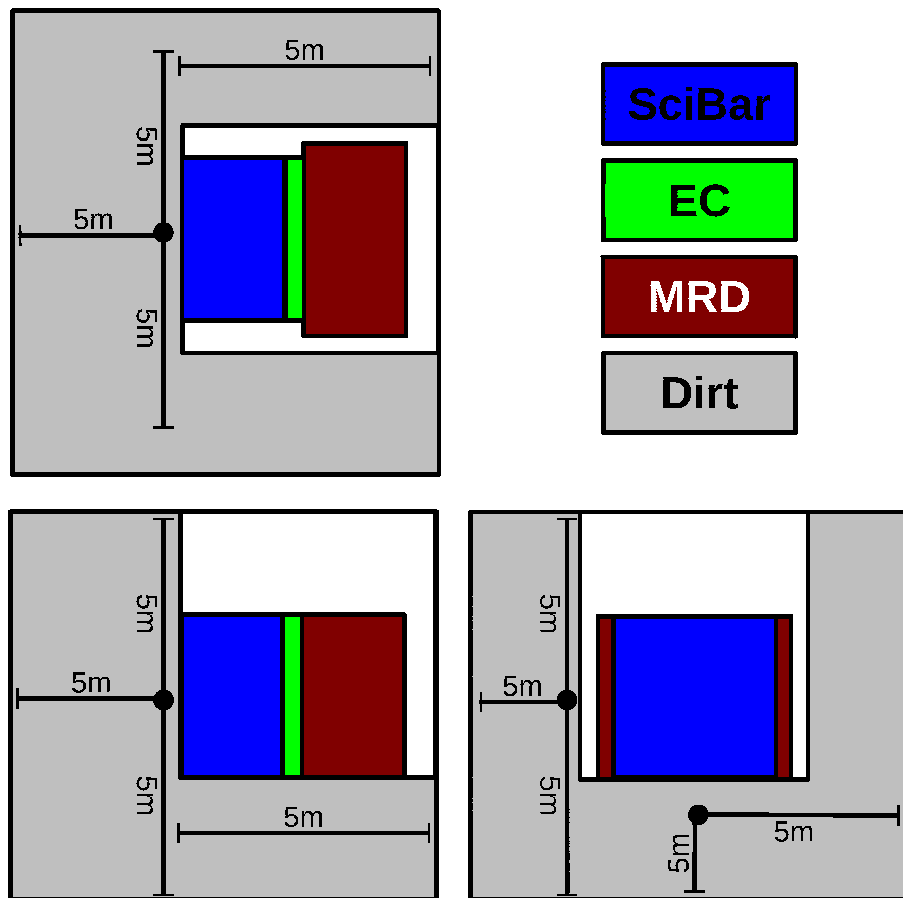


**Figure 5.5:** Schematic of the simulated dirt region showing the top (top left), side (bottom left), and front (bottom right) views of the detector and the detector hall.

the dirt material with a density  $\rho = 2.15 \text{ g/cm}^3$ . The density of the dirt is estimated from a survey done during the construction phase of SciBooNE.

The interaction vertices for dirt events that produce a single track in SciBar are shown in figure 5.6. Increasing the interaction volume did not appreciably increase the number of dirt events in SciBar, therefore the interaction volume chosen to simulate the dirt events is sufficient for SciBooNE analyses.

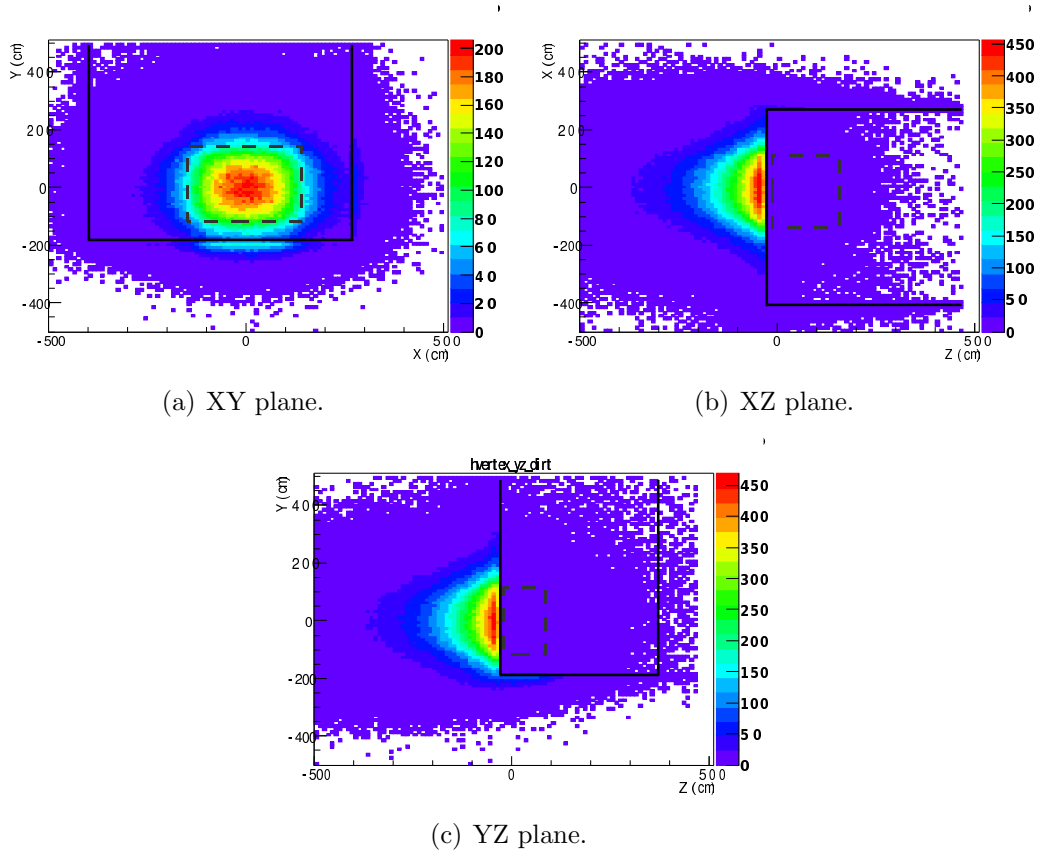


**Figure 5.6:** Interaction vertices for dirt events that produce a single track in SciBar. The solid line represents the detector hall walls, the dashed line represents the location of the SciBar detector.

Neutrino events are also generated in the EC and MRD sub-detectors. Both detectors are treated as iron structures for the purposes of the NEUT MC. There is a possibility of backwards scattered particles from an EC or MRD interaction to produce a track in SciBar. These events are also considered in this analysis.

# Chapter 6

## The Data Summary

The SciBooNE experiment took data from June 2007 to August 2008. SciBooNE had three data runs, Run I - in anti-neutrino mode, Run II, in neutrino mode, and Run III in anti-neutrino mode.

In the following sections the data quality cuts and a summary of the data-set will be described.

### 6.1 Data Quality Cuts

As mentioned in chapter 3 a number of systems are used to monitor the proton beam. Data selected for analysis has to pass certain quality control cuts to ensure both a well understood neutrino beam spectrum and that all beamline and detector systems are functioning correctly [46].

#### 6.1.1 Beam

##### Proton Beam Intensity

The proton beam intensity is monitored using 2 toroids, TOR860 and TOR875, located 200 m and 5 m upstream of the target along the beamline. These toroids

---

Cut Parameter	Cut Value	Fail Fraction
Targeting Efficiency	$\epsilon_{target} > 95\%$	0.15%
GPS Time Difference	$ t_{beam} - t_{detector}  < 10 \text{ ms}$	0.13%
Peak Horn Current	$ I_{peak}  > 170 \text{ kA}$	0.09%
Toroid Agreement	$2 \times \frac{ TOR875 - TOR860 }{(TOR875 + TOR860)} < 10\%$	0.07%
Proton Beam Intensity	$TOR875 > 0.1 \times 10^{12} \text{ ppp}$	0.06%

**Table 6.1:** Breakdown of all data quality cuts with fraction of POT that fail each cut. (ppp: protons per pulse)

monitor the protons-per-pulse (ppp) on a spill-by-spill basis. A typical spill has  $\sim 4 - 5 \times 10^{12}$  ppp. The beam quality cut requires a ppp greater than  $0.1 \times 10^{12}$  registered by the closest toroid to the target, TOR875. Figure 6.1(a) shows a typical TOR875 protons-per-pulse distribution for a SciBooNE data run.

### Toroid Agreement

Monitoring of the two toroids, TOR860 and TOR875, and any beam delivery losses between TOR860 and TOR875 is achieved by comparing the protons-per-pulse for each toroid. The beam quality cut requires agreement between the toroids to be better than 10%. Figure 6.1(b) shows a typical toroid agreement distribution for a SciBooNE data run.

### Peak Horn Current

The horn current is monitored for each spill; the nominal operating currents are 174 kA and -176 kA in neutrino and antineutrino mode respectively. The beam quality cut requires  $|I_{peak}| > 170 \text{ kA}$ . Figure 6.1(c) shows a typical peak horn current distribution for a SciBooNE data run.

### Targeting Efficiency

The beam position monitors described in chapter 3 are used to estimate the fraction,  $\epsilon_{target}$ , of beam that passes through the beryllium target. The beam quality cut requires  $\epsilon_{target} > 95\%$ . Figure 6.1(d) shows a typical targeting efficiency distribution for a SciBooNE data run.

### GPS Time Difference

The maximum BNB beam spill rate is 15 Hz; this gives a minimum spacing between spills of 67 ms. To ensure the correct matching of spills between the beam and detector the maximum separation between GPS time stamps,  $|t_{beam} - t_{detector}|$ , is required to be less than 10 ms. Figure 6.1(e) shows a typical GPS time difference distribution for a SciBooNE data run.

### 6.1.2 Detector

Additionally to failures in the beam delivery system, possible POT losses can occur due to detector downtime, summarised in table 6.2. The most frequent POT loss occurs during the DAQ deadtime at the end of a SciBooNE run whilst the run is switched. A run is switched approximately every 8 hours with a typical DAQ downtime of 3-5 minutes, this corresponds to a  $\sim 1-2\%$  loss in POT. Detector maintenance during a beam run accounts for a further  $\sim 2\%$  loss in POT. Finally sub-detector failures account for  $\sim 1\%$  of the POT losses. The high voltage, pedestals, response to cosmic muons and, in the case of SciBar, the LED gain monitoring system are monitored continuously; only when all systems are operating correctly is the data accepted.

Fail Mode	Fail Fraction
DAQ deadtime	1-2%
Detector Maintenance	2%
Sub-Detector Failures	1%

**Table 6.2:** Breakdown of detector failure modes and fraction of POT lost to each mode.

## 6.2 Data Summary

The total POT delivered to the BNB target was  $2.64 \times 10^{20}$  POT; of this  $2.52 \times 10^{20}$  POT passed all data quality cuts required for SciBooNE data analyses. This corresponds to a 95.5% POT efficiency. Figure 6.2 shows the accumulated POT

Run	Mode	Period	POT
Run I	$\bar{\nu}_\mu$	June 2007 - Aug. 2007	$0.52 \times 10^{20}$
Run II	$\nu_\mu$	Oct. 2007 - Apr. 2008	$0.99 \times 10^{20}$
Run III	$\bar{\nu}_\mu$	Apr. 2008 - Aug. 2008	$1.01 \times 10^{20}$

**Table 6.3:** SciBooNE data run summary. The POT shown is after data quality cuts are applied.

for SciBooNE during all three data runs. In this thesis the neutrino run data is considered, corresponding to  $0.99 \times 10^{20}$  POT. Between Run I and Run II a stopped cosmic muon run was recorded; this data is used in chapter 7. A full summary of the POT for each data run is presented in table 6.3.

The beam stability was monitored by measuring the number of charged-current candidate events in both SciBar and the MRD per POT. Figure 6.3 shows the event rate stability for SciBar events. The cosmic background is estimated to be 1% using a pre-beam-on timing window and is subtracted from figure 6.3. The event rate is typically 22 events for  $4 \times 10^{16}$  POT per hour in neutrino mode and can be seen to be stable over the entire data run. The event rate is  $\sim 4$  times higher in neutrino mode than in antineutrino mode; this is due to the differences in the p-Be meson production cross-sections and the difference between neutrino and antineutrino interaction cross-sections. The antineutrino event rates for the Run I and Run III agree. A similar technique is applied to MRD events; see figure 6.4. The event rate is stable over the duration of the SciBooNE run. The discrepancy between the SciBar and MRD event rate is due to the MRD's larger fiducial mass and differences in the event selection efficiencies.

Run011640 [ Sun Jan 20 12:14:00 2008 - Sun Jan 20 18:08:52 2008 ]

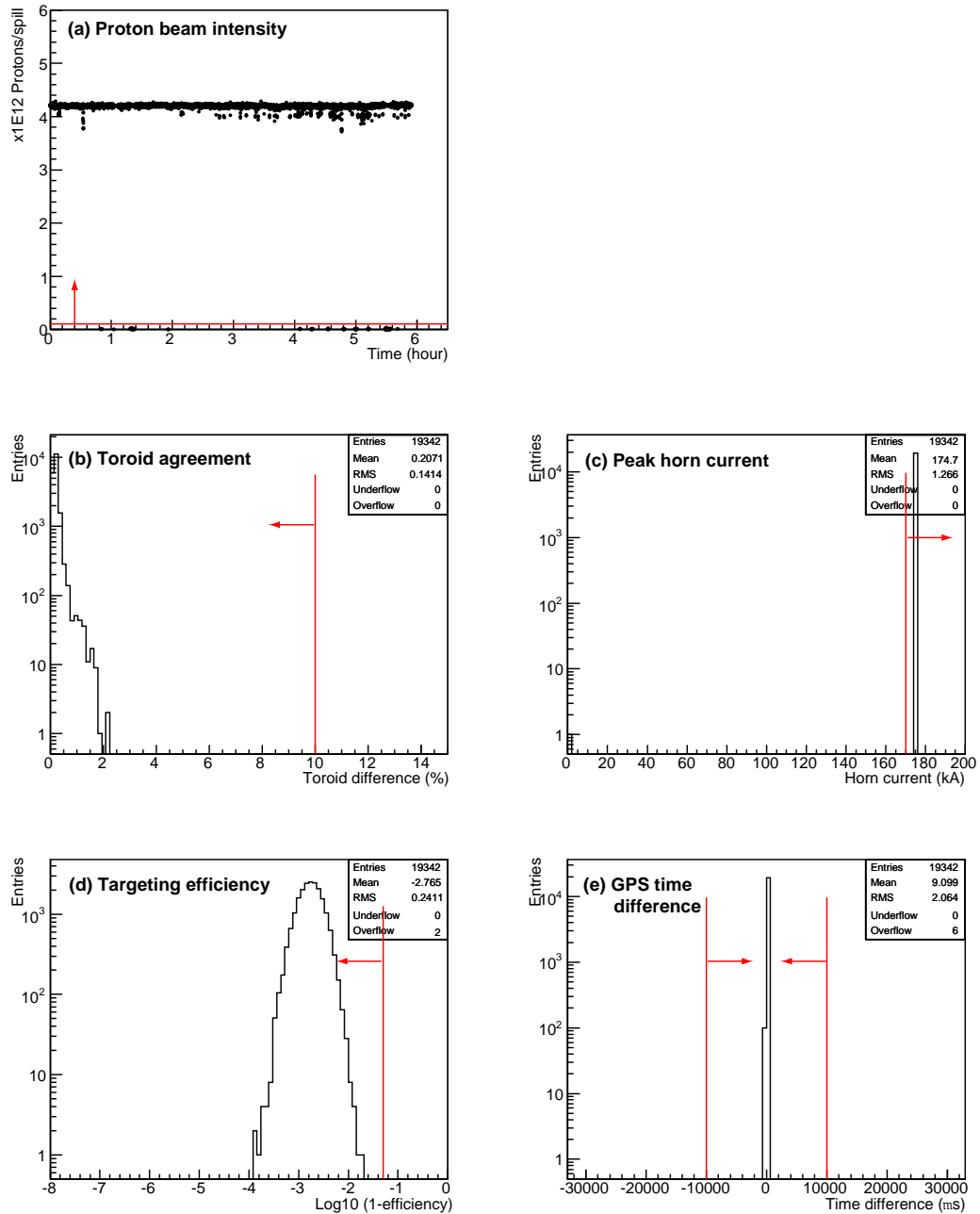


**Figure 6.1:** Distributions of the beam quality variables for a typical SciBooNE run. a) The proton beam intensity, b) the toroid agreement, c) the peak horn current, d) the targeting efficiency, e) the GPS time difference between the beam and detector. The red lines represent the cut value required for a good spill.

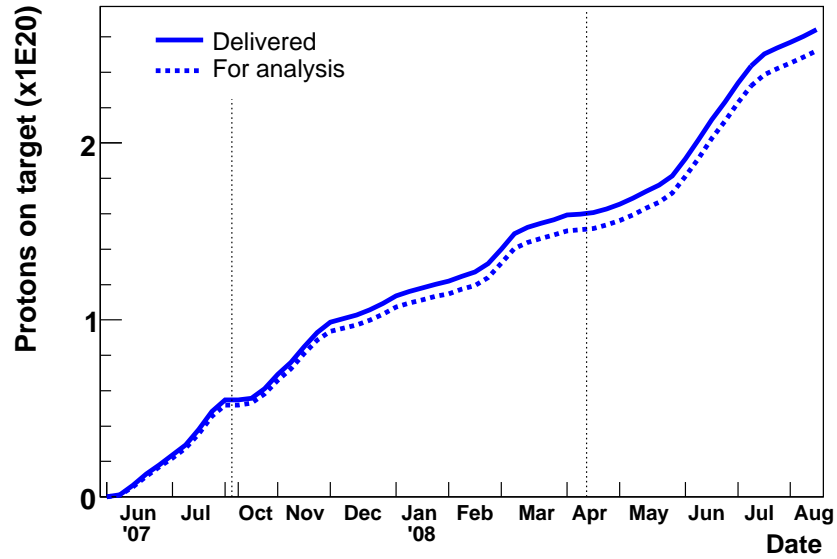


Figure 6.2: The accumulated POT during the SciBooNE run. The vertical dashed lines correspond to horn polarity switches.

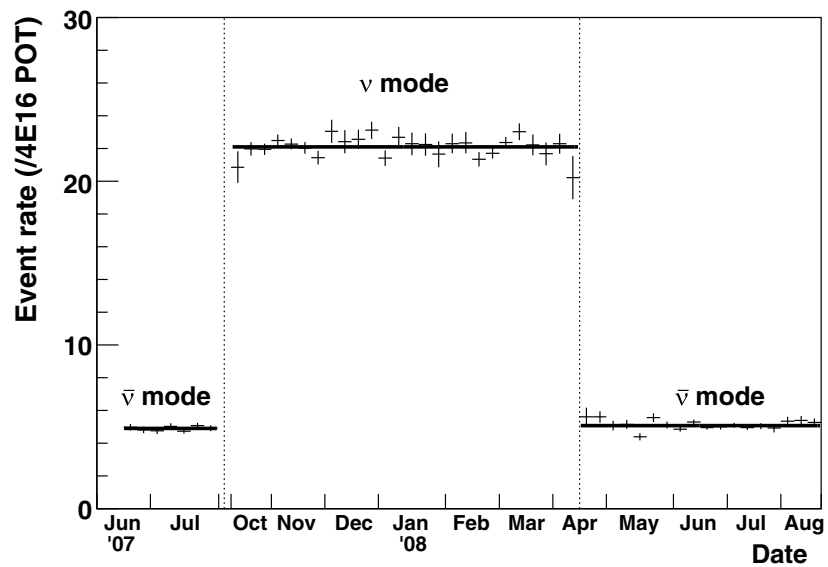


Figure 6.3: The charged-current candidate event rate stability in SciBar.

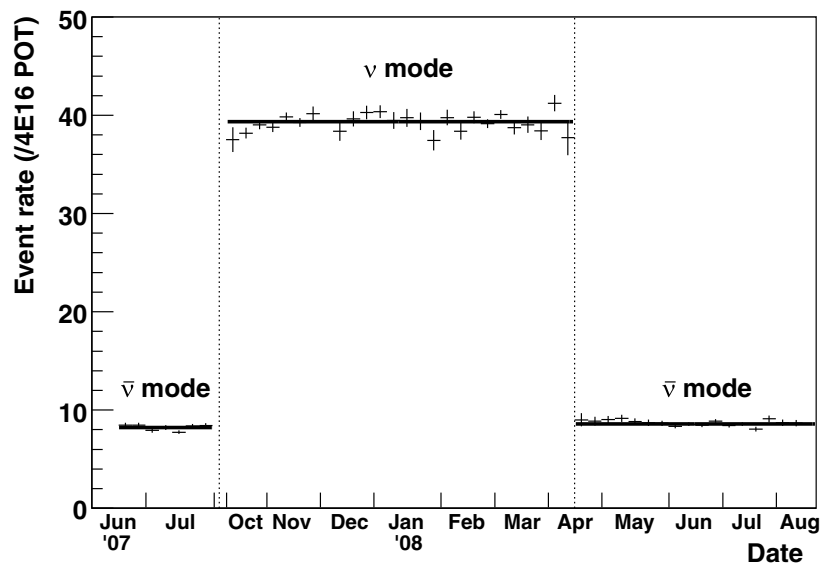


Figure 6.4: The charged-current candidate event rate stability in the MRD.

---

# Chapter 7

## Muon Tagging

### 7.1 Muon Tagging Methods

The MRD is used to identify muons in SciBooNE. For muons that don't penetrate the MRD another method to identify them is needed. Here I will describe three methods to identify muons using the SciBar timing information and the limitations of each method. Studies using specially prepared MC samples are presented and a comparison between data and MC using a stopped cosmic data-set is also described.

#### 7.1.1 Muon Double-Coincidence Method (MDC)

To tag a muon that stops in the SciBar requires the use of the multi-hit TDC information. Because of the TDC block structure it is not possible to look at the TDC information for an individual channel; instead you see the TDC hit information for all 32 channels within the TDC block. Therefore to identify a muon by looking for a second time hit from the decay (Michel) electron requires a different approach. The TDC block structure does allow for tagging by looking for a hit coincidence between two views. By looking at the last hit associated with a stopped muon candidate in both the horizontal (Y) and vertical (X) views and returning all TDC hits for these TDC blocks, a double coincidence should exist between both views if the track was produced by a stopped muon; the first coincidence for the muon

---

and a second coincidence for the Michel electron. This requirement of a double coincidence reduces the possibility of a second hit due to a source of noise being mistagged as the Michel time signature. Figure 7.1 shows a plot of  $\Delta t = |t_X - t_Y|$  taken from SciBooNE data. A cut  $<20$  ns is stipulated for TDC hits between views to be considered as a matched coincidence.

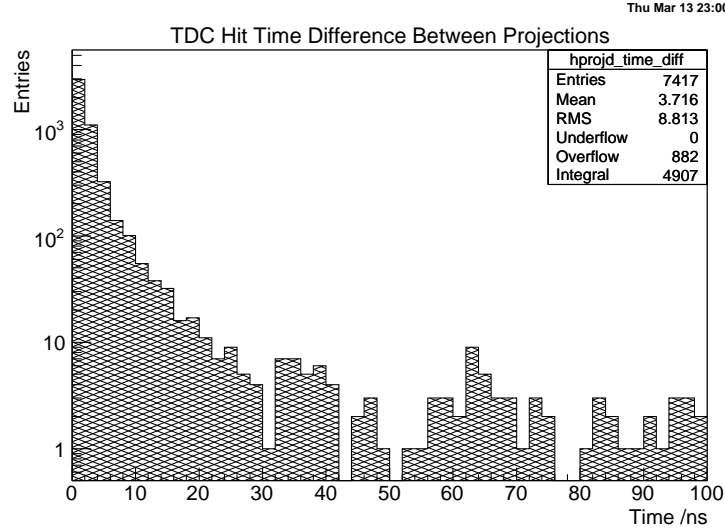
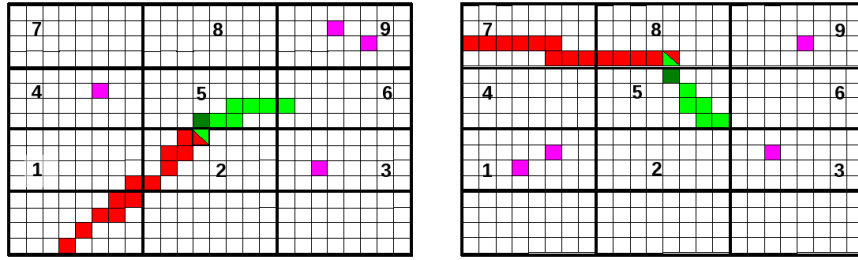


**Figure 7.1:** Time difference between views for all TDC hits (SciBooNE  $\nu$  data). The coincidence cut is set at 20 ns.

For this matching to work all that is required is the TDC time information from the TDC blocks where the track terminates. As a soft muon can technically go backwards in a SciBar event both ends of the track are considered when searching for the Michel coincidence. Theoretically, track timing could be used to determine the start and stop points of the track, however in practice this is not a reliable method when considering short tracks as mis-reconstruction of the track is possible.

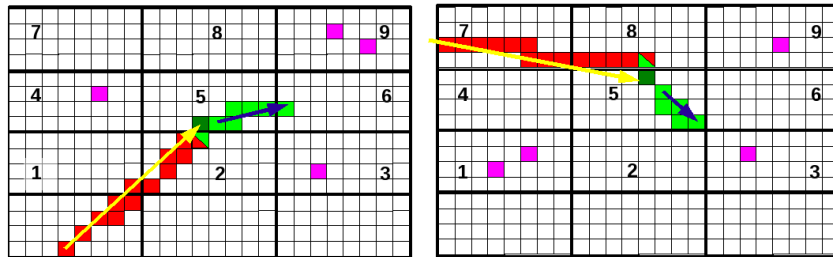
The MDC Method expands the search for a double coincidence into the 8 neighbouring TDC blocks surrounding the reconstructed track edge TDC in both views. This is to account for any errors resulting from track mis-reconstruction causing the track to be reconstructed into the incorrect TDC block.

Figure 7.2 illustrates a typical event where a muon (red hits) decays to a Michel electron (green hits). The magenta hits represent noise hits in the detector. Figure 7.3 shows the same event once track reconstruction has been applied. As can be



**Figure 7.2:** ADC hits in a ‘typical’ event, the horizontal view is shown on the left and the vertical view is shown on the right. Red hits are the muon, green hits are the Michel electron and magenta hits are random noise hits in the event.

seen the muon is mis-reconstructed into a neighbouring TDC block in both views. In the horizontal view the muon stops in TDC block 2 and is reconstructed into TDC block 5 whilst in the vertical view the muon stops in TDC block 8 and is reconstructed into TDC block 5. If a double coincidence were searched for only using the information from TDC blocks 5 in both views it would be unsuccessful.



**Figure 7.3:** The track reconstruction of the hits, showing mis-reconstruction of the muon track in both views. The muon stops in TDC block 2 in the horizontal view (left) and TDC block 8 in the vertical view (right). The muon track is mis-reconstructed into TDC block 5 in both views (yellow arrow). The blue arrow is the reconstructed Michel electron.

It is for this reason that the method is expanded to search all neighbouring TDC blocks in case of track mis-reconstruction. By comparing all combinations of TDC blocks between both views a mis-reconstructed track can still be successfully tagged as a muon.

Figures 7.4(a) and 7.4(b) show the TDC readout for all the TDC blocks shown in the typical event outlined in figure 7.2. By searching all combinations it can be found

that the match exists between TDC block 2 and TDC block 8 in the horizontal and vertical views respectively, shown in figure 7.4(c).

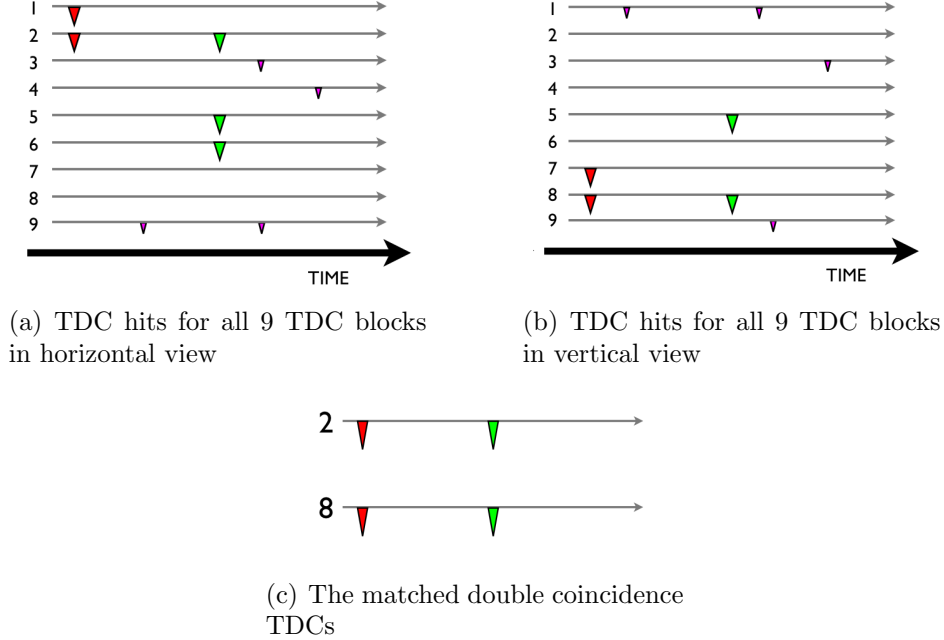


**Figure 7.4:** The TDC hits associated with the event schematic shown in figure 7.2. To find a double coincidence between two TDC blocks all combinations of TDC blocks are considered. Clearly TDC block 2 (horizontal) and TDC block 8 (vertical) have a double coincidence and so can successfully tag the event as containing a muon.

The SciBooNE software defines a hit using ADC information; therefore only TDCs with ADC hits can be considered when searching for the Michel time signature. It does not matter which hit is obtained in each TDC block as they all share the common TDC information. However to reduce the chance of matching noise hits between views an ADC cut is applied requiring the hit to have an energy deposit greater than 1 MeV.

Figure 7.5 shows the distribution of Energy deposited,  $E_{depo}$ , for all hits in the entire neutrino data set. Figure 7.5 shows that a 1 MeV cut removes the low energy noise hits from the data hits. Hits associated with tracks are calibrated using an attenuation factor which accounts for the position of the hit within the bar (see equation (7.1)).

$$E_{depo} = \Delta E e^{(x/A_f)} \quad (7.1)$$

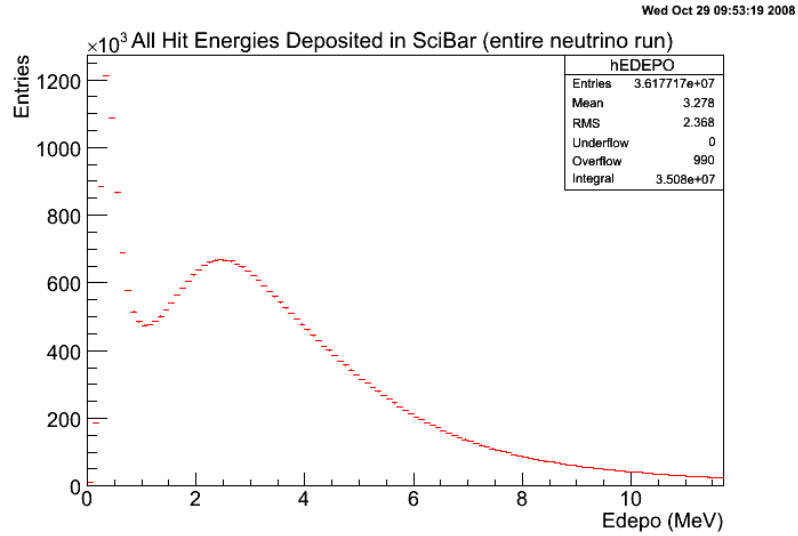


**Figure 7.5:** Energy deposited by all hits (SciBooNE  $\nu$  data). A 1 MeV cut is applied to remove noise hits.

$E_{depo}$  is the true energy of the hit,  $\Delta E$  is the reconstructed energy,  $x$  is the position of the hit, and  $A_f$  is the attenuation factor. In SciBar the attenuation factor was measured for each individual channel. It is typically of the order of 350 cm.

This position can only be known if the hit is associated with a track; therefore in the case of hits not associated with a track no attenuation factor is applied. A hit at the far end of a bar,  $x = 300$  cm, loses 57.6% of its energy. A hit unassociated with a track therefore can have a maximum energy  $\sim 230\%$  larger than that reconstructed. However, though the 1 MeV cut will remove these larger energy hits, the reason for the cut is to remove any noise hits from being considered by the method. Any loss in the efficiency of the tag due to the removal of data hits outweighs the loss in purity without the cut.

### 7.1.2 Method Limitations

When searching for a double coincidence you assume that a TDC in each view contains two time hits, one for the muon and one for the Michel electron. However this is not necessarily the case. The muon only stops in one channel and hence one view; in the other view the track is reconstructed to the last hit associated with the muon. If the last hit associated with the reconstructed track in the ‘non-stopping’

view is on the edge of a TDC block then it is possible for the first hit in that view due to the Michel electron to be in a different TDC block. This would mean no single TDC block in that view would contain two time hits associated with the muon and Michel electron and so a double coincidence would not be possible between the two views. In this instance the Michel tagging method would fail. To calculate the failure rate I model the TDC as follows:

- The migration of a Michel electron into the neighbouring cell has equal probability regardless of cell position, i.e. migration to a diagonal neighbour is as likely as an adjacent neighbour. This is a reasonable approximation given the alternating X-Y layers of scintillator bars in SciBar.

Figure 7.6 shows a schematic of a TDC block with the surrounding neighbours.

If in the ‘non-stopping’ view the last hit associated with the muon is in a corner cell (purple) then the first Michel hit can happen in five channels outside the TDC block or three channels within the TDC block. If the last hit occurs on an edge (light blue) then these cells have five neighbours within the TDC block and three neighbours outside the TDC block. If the last muon hit occurs in a central channel (dark blue) then all neighbours are within the TDC block.

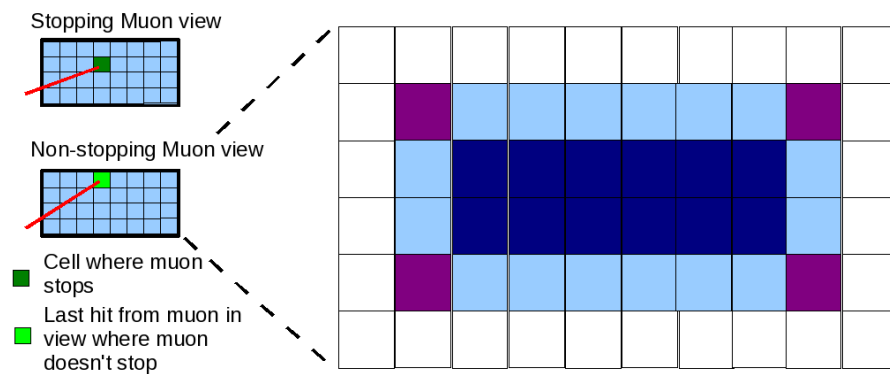


**Figure 7.6:** A schematic of a SciBar TDC block and its surrounding neighbours. The TDC block corners are highlighted in purple, the edges in light blue, the internal cells in dark blue. The white blocks belong to neighbouring TDC blocks. For the ‘non-stopping’ view the Michel electron has a probability of not leaving a time hit in the same TDC block as the final muon hit.

Table 7.1 shows the probability of the Michel electron recording a TDC hit in the TDC block. This gives an approximate upper limit for the success of the method

$\mu^-$ Hit Location	No. of Cells (per TDC Block)	$e^-$ in Cell Prob. (%)	$e^-$ in TDC Prob. (%)
Corner	4	37.5	4.6875
Edge	16	62.5	31.25
Contained	12	100	37.5
<b>Prob. <math>e^-</math> in TDC</b>			<b>73.4</b>

**Table 7.1:** The estimated probability that the Michel electron records a hit in the same TDC block as the muon in the non-stopping view.

of  $\sim 73\%$ . There are two other affects which reduce this number still further: muon capture and the TDC deadtime. Muon capture is when a muon is captured by an atom before it has a chance to decay. This accounts for approximately 8% of all muons [84]. The TDC deadtime is approximately 50 ns, with approximately 1% of decays occurring within this window. If a decay occurs in this time then no second TDC hit will be recorded and so the MDC method will be unsuccessful. Taking these additional effects into account the upper limit on the efficiency of this method is approximately 67%.

### 7.1.3 The Michel Temporal Tag (MTT)

In the case of a multiple track event it is possible to tag this event without using the above method. If, in a multiple track event, the tracks are separated by  $>50$  ns then we assume that the second track is the reconstructed Michel electron and the earlier track is then tagged as a muon. Additionally, we require these tracks to be separated by less than 24 cm; this distance corresponds to the diagonal width of a TDC block. A maximum separation cut is applied to reduce the background of multiple tracks from separate vertices being related. The diagonal TDC width is chosen to account for the fact that the muon can decay after the ADC gate has closed for a TDC block. In this instance a Michel electron would not leave any ADC information until it has exited the TDC block where it was created.

---

## 7.2 Muon Tagging Performance Studies

Monte-Carlo samples were prepared, all originating from the centre of SciBar, to look at the efficiency of the Michel tagging method. Four MC samples were studied:

- Isotropic muon ( $\mu^-$ ) sample
- Isotropic proton sample
- Isotropic pion ( $\pi^+$ ) sample
- Isotropic anti-pion ( $\pi^-$ ) sample

A data set of cosmic rays stopping within SciBar were also compared with a Monte-Carlo simulation of stopping cosmic rays.

The aim of the studies is to look at the tagging efficiency in the case of the Monte-Carlo samples in both signal ( $\mu^-$  and  $\pi^+$  MC) and backgrounds (p and  $\pi^-$ ). The stopped cosmic studies allow the comparison of a data-set of cosmic muons with a Monte-Carlo of muons and anti-muons to see if any Data/MC discrepancies exist.

### 7.2.1 Cuts and Filters

For all the studies the events are separated into one-track and two-track samples. It is possible for an event to have zero reconstructed tracks, either because the track is at high angle, or that the particle reinteracts before passing through sufficient layers in SciBar for a track to be reconstructed. Before the Michel tagging method is applied to each of these sub-sets a number of cuts are applied:

- Each event must contain at least one reconstructed track.
  - All tracks must be contained within the fiducial volume of SciBar.  $|x| = |y| < 130 \text{ cm}$  &  $2.62 \text{ cm} < z < 157.2 \text{ cm}$ .
  - The vertex separation of multi-track events  $< 24 \text{ cm}$  (the diagonal width of a TDC block)
-

## 7.2.2 Monte-Carlo Studies

### Isotropic Muon ( $\mu^-$ ) Distribution

A simulation of 5000 muons were shot from the centre of the SciBar detector isotropically each with a momentum of 200 MeV/c, soft enough to contain all the muons within the fiducial volume of SciBar. A GEANT4 event display showing 1000 of these events can be seen in figure 7.7.

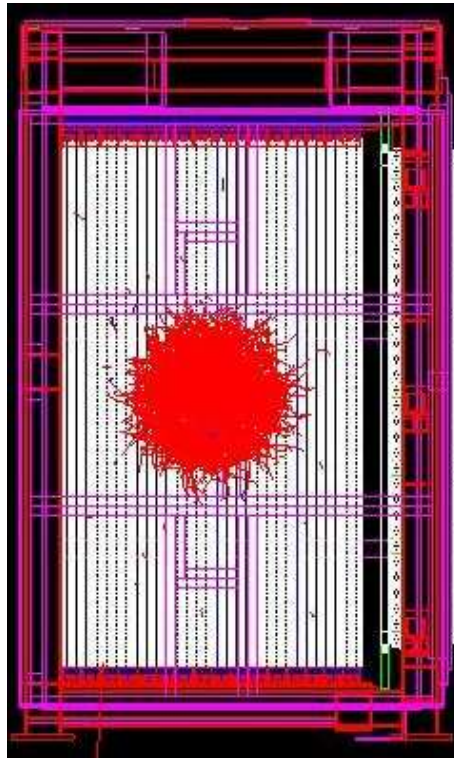


**Figure 7.7:** GEANT4 display of 1000 isotropically distributed muons within SciBar.

Table 7.2 shows the efficiencies of the method depending on the number of tracks in the event. The one-track and two-track efficiencies using the MDC method are 63.3% and 64.8%, respectively. The theoretical limitation for a pure  $\mu^-$  sample is 67% which compares well to the one-track and two-track efficiencies. The MTT method improves the two-track tagging efficiency to 84.2%.

An example of a one-track event that passes the MDC method is shown in figure 7.8. Figure 7.9 is an example of a two-track event that fails the MDC tagging method.

Tagging Method	No. Tracks	Events	Tagged	Efficiency (%)
MDC	1	3862	2444	63.28
MDC	2	301	195	64.78
MTT	2	301	272	84.21

**Table 7.2:** Tagging efficiencies for the isotropic muon distribution.

This is most likely due to the fact that the muon stops at the edge of the TDC block, resulting in one view missing a double coincidence, as outlined in section 7.1.2, and as such the method fails to tag the event as containing a muon. This event is tagged using the MTT method as the two tracks are separated in time. This failure mode for a one-track event is irreducible using the MDC method.

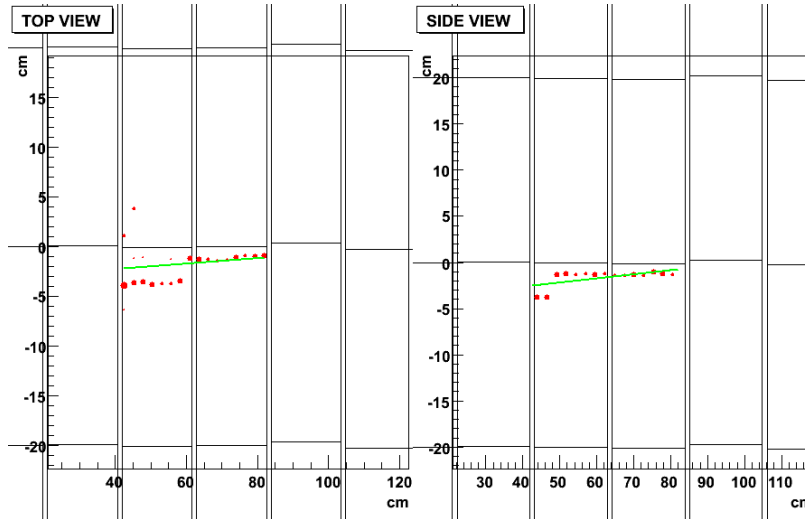


**Figure 7.8:** Event display of a reconstructed one-track event that passed the Michel tagging method. The red dots represent ADC hits in SciBar; the dot size is proportional to the energy deposited. The green line represents the reconstructed track.

By taking the time difference between the coincidences a muon lifetime can be calculated. Figure 7.10 shows the muon lifetime for the isotropic muon MC. The muon lifetime is calculated to be  $2.093 \pm 0.045 \mu\text{s}$ , in good agreement with the experimental lifetime of  $2.0263 \pm 0.0015 \mu\text{s}$  when accounting for muon capture [84], used by the MC.

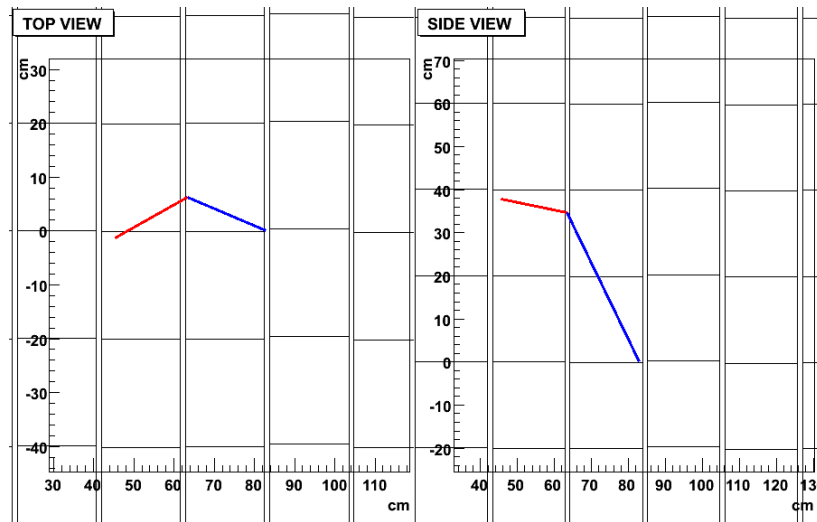


**Figure 7.9:** Event display of a reconstructed two-track event that failed the Michel tagging method. This is likely due to the muon stopping at the edge of a TDC block resulting in the ‘non-stopping’ view failure outlined in Method Limitations. The blue line represents the true muon track, the red line represents the true electron track.

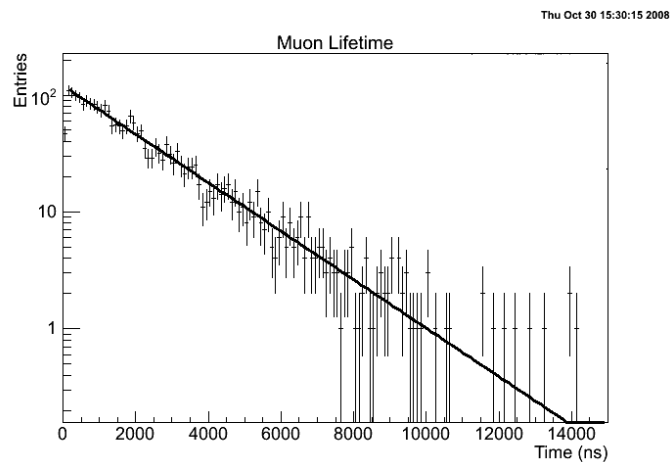


**Figure 7.10:** one-track sample reconstructed muon lifetime. A lifetime of  $2.093 \pm 0.045 \mu s$  is calculated, in good agreement with experiment when accounting for muon capture.

### Isotropic Proton Distribution

A simulation of 5000 protons were shot from the centre of the SciBar detector isotropically each with a momentum of 850 MeV/c, soft enough to contain all the protons within the fiducial volume of SciBar.

Table 7.3 shows the efficiencies of the method depending on the number of tracks in the event. Only 0.7% of one-track events and 1.6% of two-track events are mis-tagged as containing a Michel electron signature. An example of a mis-tagged proton event is shown in figure 7.11. In this event the proton interacts in the detector producing a pion which decays to an electron; this is likely to be the reason the event passes the muon tag.

Tagging Method	No. Tracks	Events	Tagged	Efficiency (%)
MDC	1	4219	29	0.69
MDC	2	122	2	1.64
MTT	2	122	2	1.64

**Table 7.3:** Tagging Efficiencies for the isotropic proton distribution.

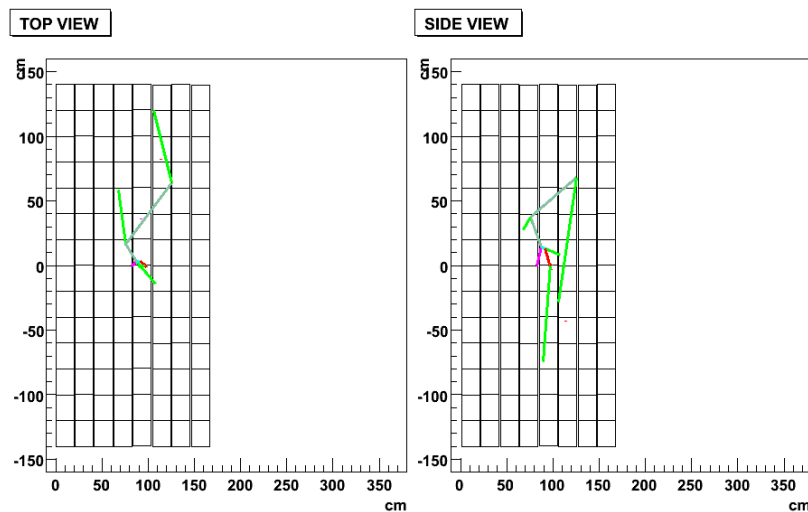


**Figure 7.11:** Event display of a reconstructed one-track proton event that passed the Michel tagging method. The proton (pink track), interacts in the detector creating a pion (light blue track) which decays to an electron (red track).

### Isotropic Pion ( $\pi^+$ ) Distribution

A simulation of 5000 pions ( $\pi^+$ ) were shot from the centre of the SciBar detector isotropically each with a momentum of 200 MeV/c, soft enough to contain all the pions within the fiducial volume of SciBar.

Tagging Method	No. Tracks	Events	Tagged	Efficiency (%)
MDC	1	3605	1813	50.29
MDC	2	417	217	52.04
MTT	2	417	311	60.91

**Table 7.4:** Tagging Efficiencies for the isotropic  $\pi^+$  distribution.

Table 7.4 shows the efficiencies of the method depending on the number of tracks in the event. 50.3% of one-track events and 52.6% of two-track events are tagged as containing a decay signature. When MTT is applied the two-track efficiency increases to 60.9%.

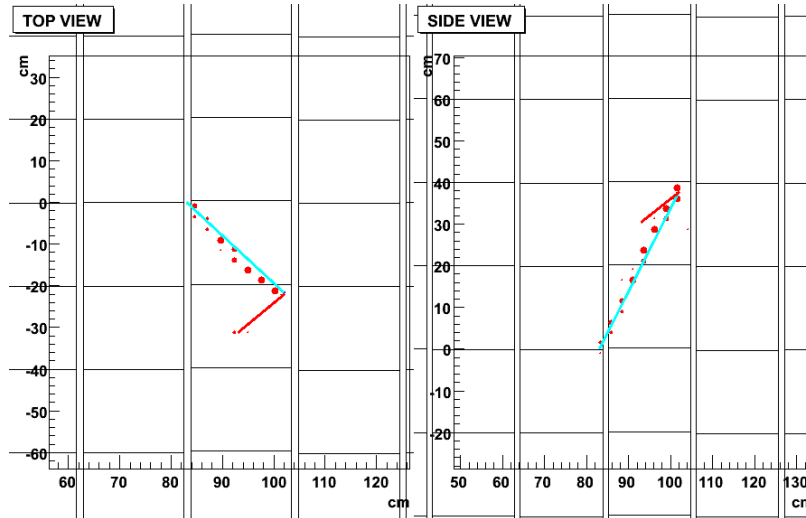


**Figure 7.12:** Event display of a reconstructed one-track  $\pi^+$  event that passed the Michel tagging method. The  $\pi^+$  (light blue track) decays to a  $\mu^+$  (not visible due to very short track) which decays to an electron (red track).

By taking the time difference between the coincidences a decay lifetime can be calculated. The  $\pi^+$  decay to  $\mu^+$  with a lifetime of  $2.603 \times 10^{-8}$  s [85]; this is approximately 100 times smaller than the muon lifetime.  $\mu^+$  don't undergo muon capture so the expected reconstructed lifetime should be higher than for the isotropic

$\mu^-$  sample. Figure 7.13 shows the decay lifetime for the isotropic pion MC is  $2.230 \pm 0.050 \mu\text{s}$ , this is in good agreement with the world average for muon decay excluding muon capture [85], used by the MC.

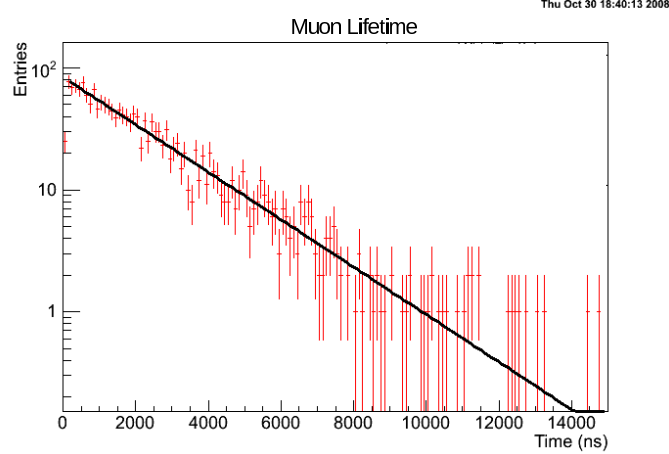


**Figure 7.13:** one-track sample reconstructed muon lifetime. A lifetime of  $2.230 \pm 0.050 \mu\text{s}$  is calculated.  $\pi^+$  decay to  $\mu^+$  which don't undergo capture, therefore the lifetime is higher than observed in the isotropic  $\mu^-$  sample.

### Isotropic Anti-Pion ( $\pi^-$ ) Distribution

A simulation of 5000 pions ( $\pi^-$ ) were shot from the centre of the SciBar detector isotropically each with a momentum of 250 MeV/c, soft enough to contain all the pions within the fiducial volume of SciBar.

Tagging Method	No. Tracks	Events	Tagged	Efficiency (%)
MDC	1	3492	191	5.47
MDC	2	257	18	7.00
MTT	2	257	9	3.50

**Table 7.5:** Tagging Efficiencies for the isotropic  $\pi^-$  distribution.

Table 7.5 shows the efficiencies of the method depending on the number of tracks in the event. 5.5% of one-track events and 7.0% of two-track events are tagged as containing a decay signature.  $\pi^-$  have a very high nuclear capture rate; as such few  $\pi^-$  decay within SciBar; this explains the low tagging efficiency. When MTT is applied the two-track efficiency decreases to 3.5%. This is likely due to the fact that most two track events contain a reconstructed pion and muon from the pion decay.

The pion lifetime is  $2.603 \times 10^{-8}$  s; therefore the tracks will be within the 50 ns window. Figure 7.14 shows a  $\pi^-$  decay in flight, producing a muon which decays to an electron.

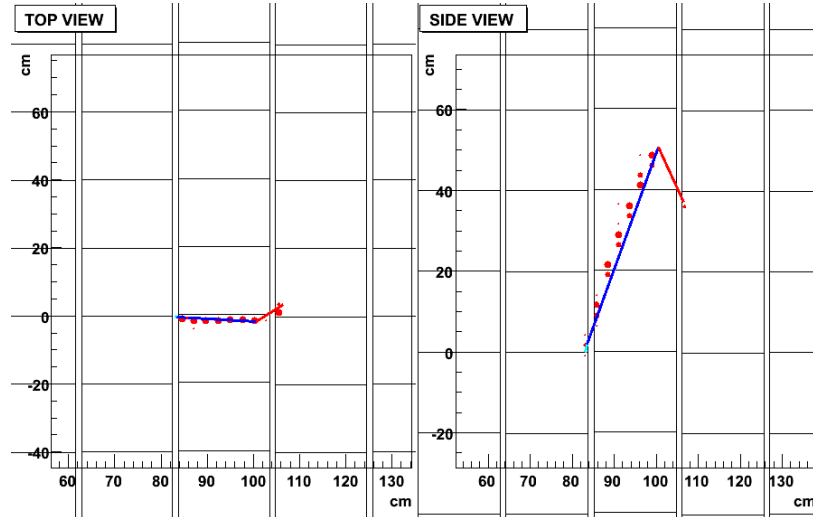


**Figure 7.14:** Event display of a reconstructed one-track  $\pi^-$  decay event that passed the Michel tagging method. The  $\pi^-$  (light blue track) decays in flight to a  $\mu^-$  (dark blue track), which decays to an electron (red track).

## Conclusions

The muon tagging methods tag muon candidate events with an efficiency of  $\sim 64\%$ , similar to what is expected given the detector geometry. Less than 2% of proton tracks are mis-tagged.

## 7.3 Two Single Coincidences Method (TSC)

An improvement can be made to the MDC method. Instead of looking for a double coincidence, two single coincidences can be matched to tag the muon. Each 3-D track has two 2-D projections which are matched together. As described in section 7.1.1, the MDC method searches the nine TDC blocks surrounding the track ends for two TDC hits, one associated with the muon and one associated with the Michel electron. However, as highlighted in section 7.1.2, the muon only stops in one of the

two views, the other view just shows the last hit from the muon in that view before it stops. Therefore there is no reason why the time hit associated with the Michel electron will be in the same TDC block as the muon in that view. To account for this fact an extension to the MDC method can be made. Figure 7.15 shows a schematic comparing the MDC method with the two single coincidences (TSC) method. The TSC method finds a coincidence associated with a muon, then subsequent hits in that TDC block are compared with hits in the opposing view to identify a time signature associated with the Michel electron.

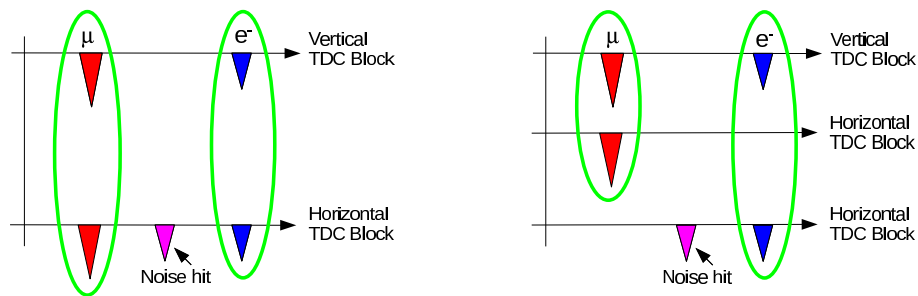


**Figure 7.15:** Schematic showing the TDC information required to successfully tag a muon using the MDC method (left) and the TSC method (right). In the TSC schematic the muon stops in a vertical TDC block, in the horizontal view two TDC blocks are needed to tag the muon and the Michel electron.

As in the MDC method, the TSC method uses the information from the nine TDC blocks in each view surrounding the track end. The TSC method also employs a 1 MeV cut to exclude noise hits from faking a coincidence.

The TSC method will be compared to the MDC method in the stopped cosmic ray study.

## 7.4 Stopped Cosmic Ray Data and Monte-Carlo Studies

Stopped cosmic data was taken during the April 2008 shutdown to switch the horn polarity of the Booster neutrino beam. The typical cosmic trigger used by SciBar during the data run used four vertical rows of TDC blocks to trigger on through passing cosmic rays. To trigger on a stopped cosmic event three of the four TDC rows

are required to have a coincidence with one of the outer TDC rows not triggering. A schematic comparing a through passing cosmic to a stopped cosmic can be seen in figure 7.16 (the blue rows represent the TDC rows used for cosmic triggering). An example of a stopped cosmic event in the data can be seen in figure 7.17.

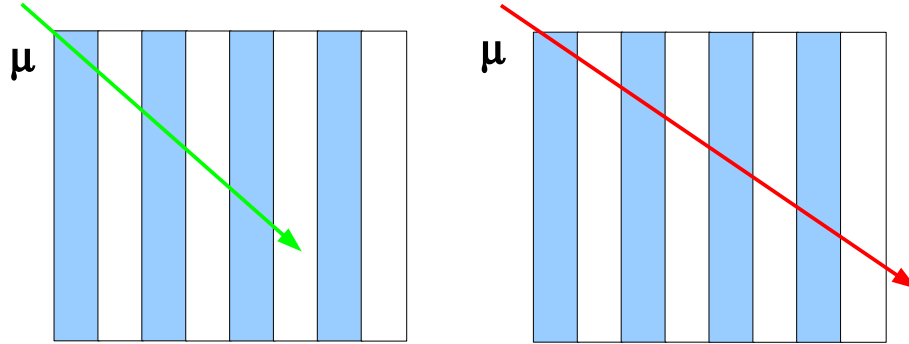


**Figure 7.16:** A schematic showing a stopped cosmic-ray (left) and a through passing cosmic-ray (right). The blue rows represent the 4 TDC rows used for cosmic triggering. To trigger a stopped cosmic event one of the outer TDC rows must not trigger.

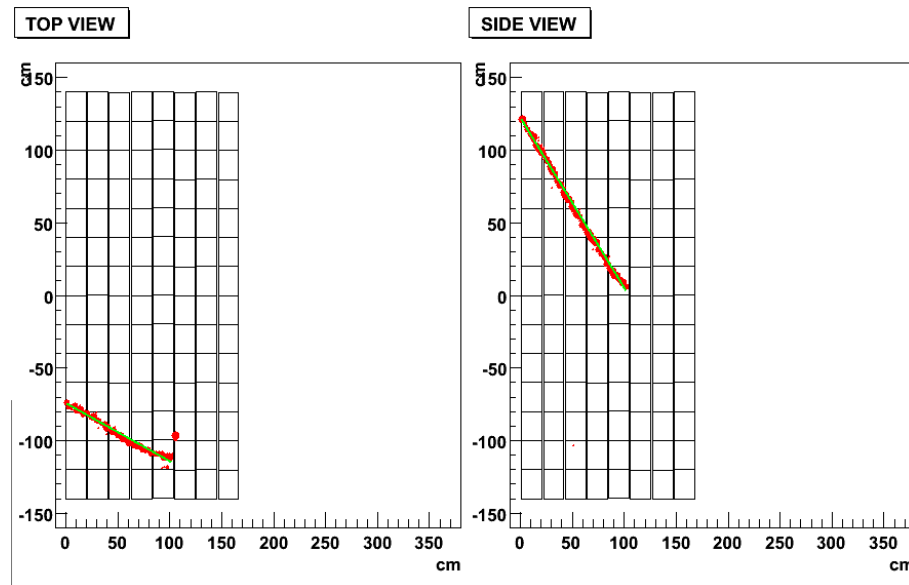


**Figure 7.17:** An event display of a cosmic ray stopping in the SciBar detector. The event was recorded during the special stopped cosmic data run.

It is possible for the stopped cosmic trigger to also trigger on high-angle, through-passing, tracks that only hit three TDC rows. A fiducial volume cut is applied to the data to remove these high angle events. For the stopped cosmic studies a number of changes were made to the fiducial volume filter. For a track to successfully pass the fiducial volume filter its lowest vertex in Y has to be contained within the fiducial

volume with the highest vertex in  $Y$  sitting outside the fiducial volume. The size of the fiducial volume was also reduced to reduce the number of through passing cosmics that are reconstructed as stopping within the fiducial volume. The adjusted fiducial volume for the end-point of the track was set as

- $|x| = |y| < 130$  cm and  $10.48$  cm  $< z < 149.34$  cm

with the start-point of the track being outside this fiducial volume. Only one-track data events are considered to remove possible contamination from multiple cosmic-ray events, and non-muon cosmic rays.

The stopped cosmic data was directly used to produce the stopped cosmic Monte-Carlo. For each event the track angles  $\theta$  and  $\phi$ , the muon momentum  $p_\mu$ , and the cosmic entry point were recorded to a root tree and used to reconstruct the event in Monte-Carlo. The  $\mu^+$  to  $\mu^-$  ratio for cosmic rays under 10 GeV/c is between 20-30% [85]. One  $\mu^+$  and one  $\mu^-$  MC file, using the input parameters taken from the data, are created. Reweighting of the  $\mu^+$  events is done to match the 20-30% discrepancy seen in cosmic data.

The data-set consists of 7010 stopped cosmic events within the fiducial volume. 13,708 stopped cosmic events are simulated in Monte-Carlo. The angular distribution for data and MC can be seen in figure 7.18. An asymmetry exists in the  $\tan \theta_{yz}$  angular distribution due to the geometry of the detector hall. SciBar is tight against the upstream wall of the detector hall, but not the downstream wall. Therefore the upstream edge has greater shielding to cosmics hence the lower rate.

5751 and 5895 one-track, and 760 and 683 two-track  $\mu^+$  and  $\mu^-$  MC events pass the fiducial volume cut, respectively. Table 7.6 show the tagging efficiency for data and MC for a TDC deadtime of 100 ns.

The TSC method tagging efficiency is higher than the MDC method in data and MC for both the one-track and two-track samples. The TSC and MTT method have similar tagging efficiencies for the two-track MC sample (Note: No two-track data sample was studied). The difference in the tagging efficiencies for the one-track

Tagging Method	No. Tracks	Tagging Efficiency (%)
<b>Data</b>		
MDC	1	64.9
TSC	1	71.4
<b><math>\mu^+</math> MC</b>		
MDC	1	75.8
TSC	1	81.5
MDC	2	64.6
TSC	2	71.1
MTT	2	70.7
<b><math>\mu^-</math> MC</b>		
MDC	1	72.7
TSC	1	78.1
MDC	2	65.1
TSC	2	73.2
MTT	2	66.9
<b>Combined <math>\mu^+</math> and <math>\mu^-</math> MC (1.2 : 1)</b>		
MDC	1	74.4
TSC	1	79.9
MDC	2	64.8
TSC	2	72.0
MTT	2	69.1
<b>Combined <math>\mu^+</math> and <math>\mu^-</math> MC (1.3 : 1)</b>		
MDC	1	74.5
TSC	1	80.0
MDC	2	64.8
TSC	2	71.9
MTT	2	69.1

**Table 7.6:** Tagging Efficiencies for the stopped cosmic study with a TDC deadtime of 100 ns. Not adjusting the ratio of  $\mu^+$ s to  $\mu^-$ s does not significantly affect the tagging efficiencies.

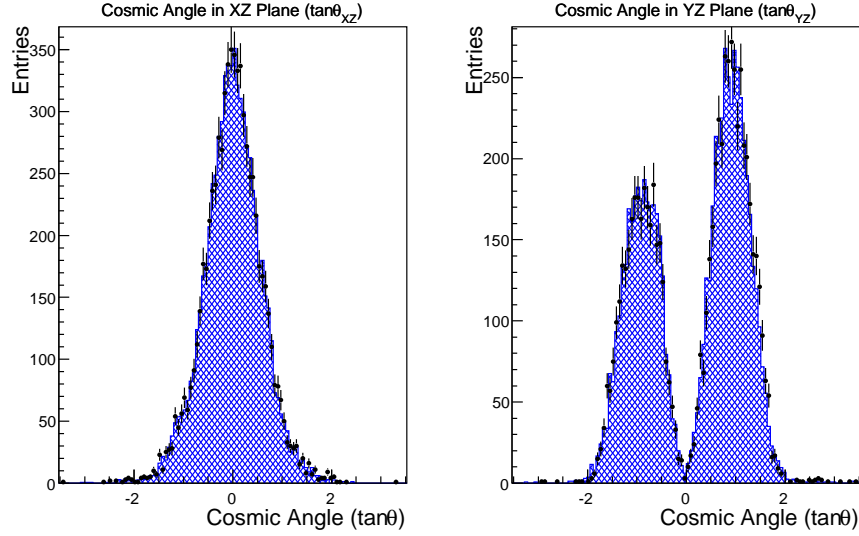


**Figure 7.18:** Stopped cosmic angular distributions in data and MC.  $\tan\theta_{xz}$ , (left) and  $\tan\theta_{yz}$  (right). The  $\tan\theta_{yz}$  is asymmetric due to the geometry of the detector hall. Positive  $\tan\theta_{yz}$  values correspond to cosmic rays entering SciBar from the downstream side of the detector hall. Negative  $\tan\theta_{yz}$  values correspond to cosmic rays entering SciBar from the upstream side of the detector hall.

$\mu^+$  and  $\mu^-$  samples, mainly due to muon capture, are not seen for the two track samples. This is because the two-track sample is made up of events where the muon has decayed, producing a Michel electron; therefore the tagging efficiency for the  $\mu^+$  and  $\mu^-$  samples should be the same.

There is a discrepancy between the one-track data and MC tagging efficiencies. In data the MDC method has a tagging efficiency of 64.9%, 10% less than in MC. For the TSC method has a tagging efficiency of 71.4% in data, around 8.5% lower than in MC. This discrepancy needs to be understood. There are two possible reasons for this difference:

- Incorrect MC TDC deadtime
- Mis-reconstruction of data events

#### Incorrect MC TDC Deadtime

To study the effect of different TDC deadtimes, the minimum temporal separation between coincidences was altered.

Data/MC	No. Tracks	TDC Deadtime			
		50 ns	100 ns	200 ns	300 ns
<b>MDC Method</b>					
Data	1	65.2	64.9	62.9	60.5
MC	1	75.7	74.4	71.0	67.8
<b>MC - Data</b>		<b>10.5</b>	<b>9.5</b>	<b>8.1</b>	<b>7.3</b>
<b>TSC Method</b>					
Data	1	72.0	71.4	68.7	65.9
MC	1	81.4	79.9	76.2	72.8
<b>MC - Data</b>		<b>9.4</b>	<b>8.5</b>	<b>7.5</b>	<b>6.9</b>

**Table 7.7:** Tagging Efficiencies for different TDC deadtimes. The  $\mu^+$  to  $\mu^-$  ratio is set to 1.2 : 1.

As can be seen from table 7.7 though the discrepancy is slightly reduced by increasing the TDC deadtime, it does not fully account for the discrepancy seen between data and MC.

### Track Mis-reconstruction

To trigger on a stopped cosmic event only three of the four TDC trigger planes register a hit. It is, therefore, possible for a high angle cosmic passing through the detector to fake a stopped cosmic event. Figure 7.19 is an example of a through-passing cosmic ray which passes the stopped cosmic trigger. In this event a track (green line) is mis-reconstructed inside the fiducial volume. In data this event would fail the Michel tagging methods outlined above. However, because the data is used to generate the MC, using the energy, entry position, and angle of the reconstructed track, this event in MC will be a contained muon which can be identified using the Michel tagging methods. We need to estimate what proportion of events in the data correspond to through-passing cosmics.

A through-passing event should have more hits recorded in SciBar than the equivalent event in MC. The number of hits, and data/MC asymmetry, are shown in figure 7.20. There is a clear asymmetry between the number of data hits and MC hits. The positive asymmetry is 908 events in a total data-set after the fiducial volume cut of 7010 events. This is equivalent to 12.9% of data events. This fully encompasses the data-MC tagging discrepancy. An eye scan of 200 events saw 20 through-passing events. The discrepancy can be fully explained due to track mis-reconstruction.

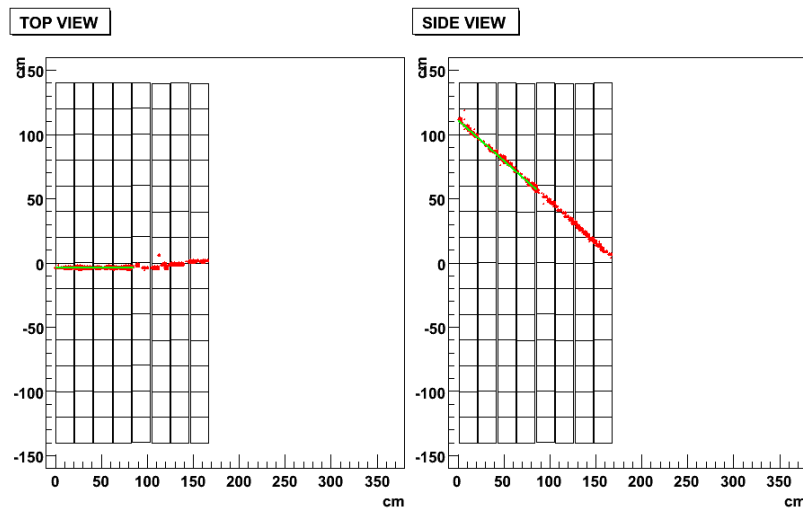


**Figure 7.19:** An event display of a through passing cosmic ray which is reconstructed within the fiducial volume.

## 7.5 Summary

The MDC method performs as expected given the method limitations outlined in section 7.1.2. From the stopped cosmic study it is clear that the data and MC agree well once the discrepancy due to through-passing cosmic rays is accounted for. The TSC method performs better than the MDC method for the one-track sample; as such this method will be used in the analysis.

In the two-track sample the TSC method performs similarly to the MTT method. In the analysis the two-track sample has 2 sub-sets, the  $\mu + p$  and  $\mu + e$  samples. In the case of the  $\mu^- + p$  sample the muon can not be identified using the MTT method, therefore the TSC method is employed to identify these events. For the  $\mu + e$  sample, it is easier to identify two-track events by comparing the time of each track, without the risk of mis-tagging an event due to a noise hit. Therefore the MTT method is preferred over the TSC method and will be used in the analysis to identify  $\mu + e$  events.

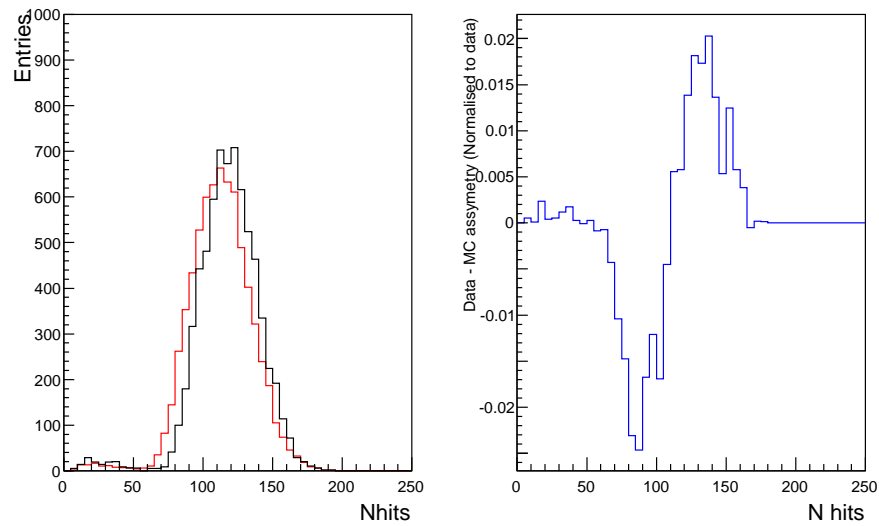


**Figure 7.20:** Left: The number of hits per event for the data (black line) and MC (red line) stopped cosmic samples. Right: The difference between the number of data and MC hits normalised to the total number of hits. Data events have a higher number of hits per event, due in part to through-passing cosmics. The MC is normalised to the number of data events.

---

# Chapter 8

## CCQE SciBar-Contained Event Selection

### 8.1 Analysis Overview

There are a number of signatures for a charged-current quasi-elastic event. The theoretical signature contains a muon and a proton produced at the interaction vertex. In practice it is not always possible to see the proton due to nuclear effects or limitations on event reconstruction due to detector geometries. Events can therefore be classified as one-track and two-track events. The major background to CCQE events are charged-current pion production events, where the pion is mis-identified as a proton. For one-track events where the pion is not reconstructed in SciBar this is an irreducible background, with both signal and background being a single muon track. This is not an irreducible background in the MiniBooNE detector for events where the pion is not absorbed. In this instance MiniBooNE is able to identify two decay electrons associated with the primary muon decay and secondary muon decay, produced by the pion. This is not possible in SciBar because of the detector geometry. As described in chapter 7, nine TDC blocks are used to search for the decay electron, it is therefore possible for one decay electron to produce a coincidence associated with both tracks. A schematic of this process can be seen in figure 8.1. Because of this, in multi-track events, it is also not possible to identify which track is associated with the muon using the coincidence information alone.

---

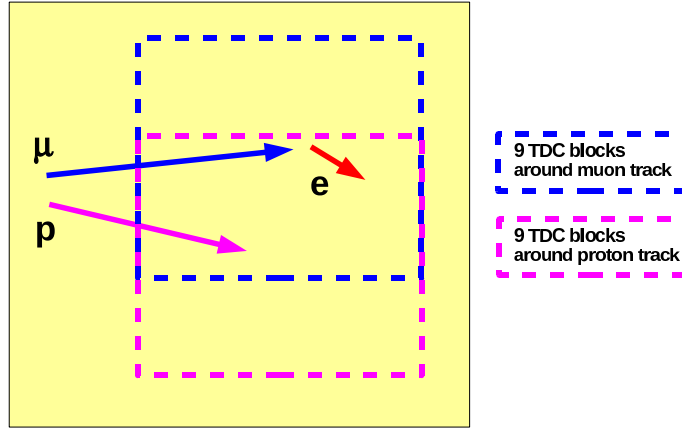


**Figure 8.1:** Schematic of the nine TDC blocks surrounding the muon track (blue dashed box) and the proton track (pink dashed box). One decay electron can be matched to both tracks, this is a fake signal for a CC- $\pi$  event. As such SciBooNE is unable to distinguish CCQE and CC- $\pi$  events using timing information alone.

If, in SciBooNE, the muon from the CCQE interaction decays in the detector it is possible for the decay electron to be reconstructed as a track. It is also possible for three-track events with a muon, proton, and decay electron to be reconstructed. The two-track ( $\mu + p$ ) signal and ( $\mu + \pi$ ) background samples can be distinguished using particle identification cuts. Pions and proton have different  $\frac{dE}{dx}$  signatures. This is because pions, like muons, typically have higher  $\beta$  values when emitted, as such they are minimum ionising particles (MIP) just after emission. This is not true of the proton.

Presented here is an analysis isolating the SciBar-contained fraction of charged-current quasi-elastic events during the neutrino beam run. Five samples, four CCQE and one background, are defined,

- CCQE: muon sample (1 track).
- CCQE: muon + decay (Michel) electron sample (2 tracks).
- CCQE: muon + proton sample (2 tracks).
- CCQE: muon + proton + Michel electron sample (3 tracks).
- Background: muon + pion sample (2 tracks).

The three-track  $\mu + p + \pi$  sample is not considered because all three tracks occur promptly; this is not a background to the three-track  $\mu + p + e$  CCQE sample as the reconstructed electron is produced after the muon and proton tracks. Additionally the  $\mu + p + \pi$  sample has one interaction vertex, which is not the case for the  $\mu + p + e$  sample. The one-track  $\mu$  and two-track  $\mu + e$  events are combined before applying the cross-section extraction architecture. Three-track events, with reconstructed muon, proton and Michel electron, are not considered in this analysis as the number of events is very small. The background sample, predominantly  $\text{CC-}\pi^+$  events, is considered as a way to constrain the background in the cross-section extraction architecture, this is further explained in chapter 9. Schematics of the four different event signatures can be seen in figure 8.2. Each sample is considered separately, with cuts used to enhance their respective purities.

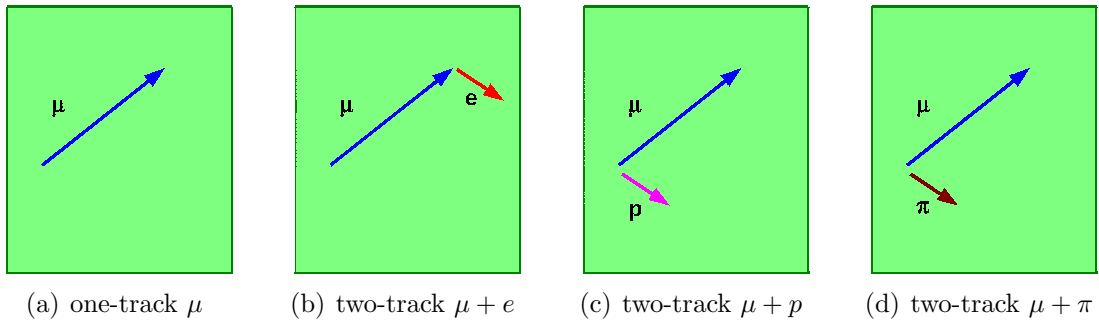


**Figure 8.2:** Typical event signatures for the four samples. (a-c) CCQE events, (d)  $\text{CC-}\pi$  event (dominant background).

Once all the samples have been selected, the goal of this analysis is to make an absolute cross-section measurement for CCQE neutrino-nucleon interactions.

## 8.2 Event Selection

The first step of event reconstruction in SciBar is to match reconstructed two-dimensional tracks in the horizontal and vertical view. Track reconstruction in each view is done using a cellular automaton algorithm [86]. For tracking, the hit threshold is set to 2 photo-electrons, corresponding to approximately 0.2 MeV. To

---

match two two-dimensional tracks, the timing difference between tracks must be less than 50 ns and the z-edges, the vertex positions in the beam direction, must be separated by less than 6.6 cm. Reconstructed tracks must penetrate at least three layers in each view; therefore the minimum reconstructed track length is 8 cm.

To select the SciBar-contained charged-current events a series of pre-cuts are applied to the data-set

1. Zero MRD tracks
2. 1<sup>st</sup> layer hits veto cut
3. All tracks contained in SciBar fiducial volume (FV)
4. Beam window cut

MC distributions are either normalised to the number of charged-current SciBar-MRD matched events or the number of protons on target. The charged-current SciBar-MRD matched sample is the standard charged-current data-set that all charged-current analyses use for normalisation. This allows comparisons of standard cuts used by multiple SciBooNE analyses. The number of charged-current inclusive SciBar-MRD matched events in data is 30,337 [46].

### **Zero MRD tracks**

SciBooNE has three data reductions. The first reduction data includes all events with any hit information. The second reduction data includes all events with reconstructed three dimensional tracks. The MRD-matched reduction data includes all events with a track in the SciBar detector matched to a track in the MRD. The second reduction data is used for this analysis. To isolate SciBar contained events, all events with a track in the MRD, whether associated with a SciBar track or not, are removed.

---

### 1<sup>st</sup> Layer Veto Cut

Neutrino interactions can occur upstream of the detector, either in the dirt or detector walls. These interactions can produce particles that propagate into the detector. To minimise the number of such events in SciBar, any events containing hits in the first layer of SciBar, whether associated with a track or not, are removed from the data-set.

### Fiducial Volume Cut

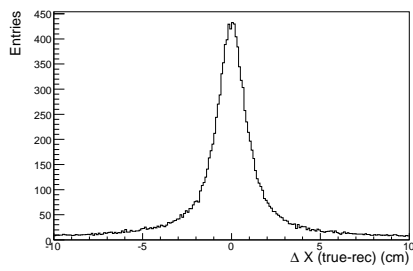
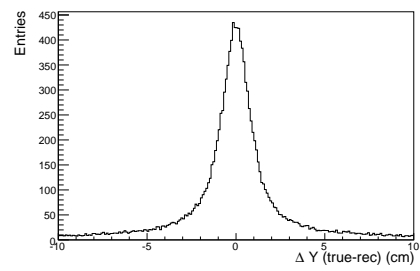
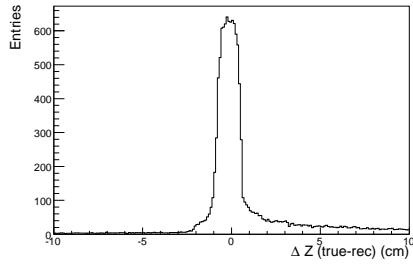
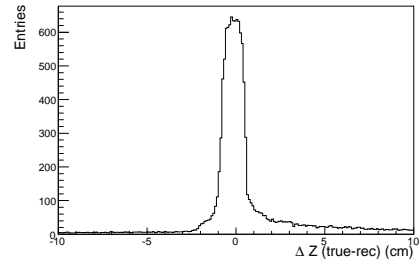
After requiring zero MRD tracks a fiducial volume cut is applied to the data. The SciBar fiducial volume used by all analyses is defined as:

$$\begin{aligned} -130 \text{ cm} < x < 130 \text{ cm} \text{ ,} \\ -130 \text{ cm} < y < 130 \text{ cm} \text{ ,} \\ 2.62 \text{ cm} < z < 157.2 \text{ cm (2nd-60th layer)} \end{aligned} \quad (8.1)$$

Therefore the SciBar fiducial volume and mass is:

$$260 \text{ cm} \times 260 \text{ cm} \times 154.58 \text{ cm} \times 1.021 \text{ g/cm}^3 = 10.6 \text{ tonnes} \quad (8.2)$$

Both the interaction vertex and track termination vertices are contained within the fiducial volume for the SciBar contained sample. The interaction vertex resolution can be determined by comparing the truth information in MC with the reconstructed vertex. Figure 8.3 shows the difference between the true vertex and reconstructed vertex for the SciBar-contained sample, estimated using the MC simulation. The vertex resolution is determined by fitting a Gaussian to each projection. For the  $x$  and  $y$  projections the vertex resolution is determined to be 1.3 cm, for the  $z$  projection the vertex resolution is 0.5 cm. Since the vertex resolution in the  $z$  projection is discretely determined and the true vertex is a uniform distribution, the expected resolution is  $1.3/\sqrt{12} \sim 0.4$  cm, in good agreement with what is measured. The  $z$  vertex can be reconstructed in two ways: Assuming the upstream track vertex is the interaction vertex, see figure 8.3(c), or using track timing information to determine the interaction vertex, see figure 8.3(d). Both reconstructions produce an asymmetry for positive values of  $\Delta z$ , this suggests that the data set is dominated by

(a)  $\Delta x$  (true - reco)(b)  $\Delta y$  (true - reco)(c)  $\Delta z$  (true - reco) assuming upstream vertex is interaction vertex(d)  $\Delta z$  (true - reco) using track timing information

**Figure 8.3:** Difference between the true vertex and reconstructed vertex estimated with the MC simulation for (a) The  $x$  projection, (b) the  $y$  projection, (c) the  $z$  projection assuming an upstream vertex and (d) the  $z$  projection using track timing information.

forward-going tracks, and that the asymmetry does not arise from mis-reconstructing the track direction. If an event contains back-to-back backward and forward going particles, it is possible for the tracking algorithm to reconstruct this event as a single track event where the interaction vertex is upstream of the reconstructed vertex. A schematic of this mis-reconstruction is shown in figure 8.4. This same asymmetry is also seen in the SciBar-MRD matched sample.

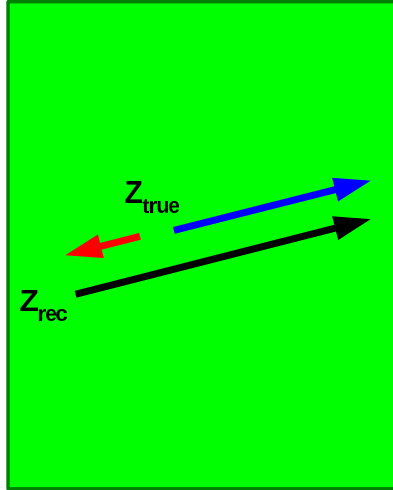
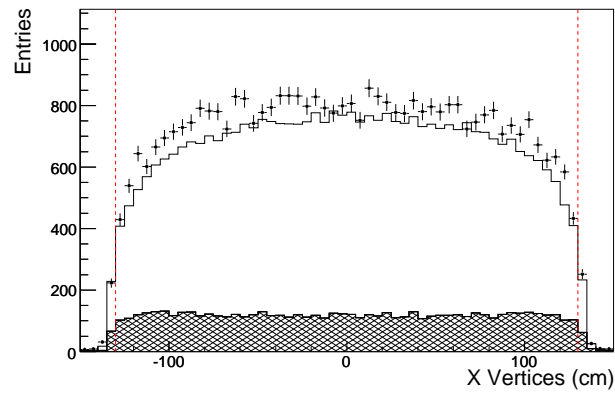


**Figure 8.4:** Back-to-back track events can be mis-reconstructed as single track events. This can result in the reconstructed interaction vertex being upstream of the true interaction vertex.

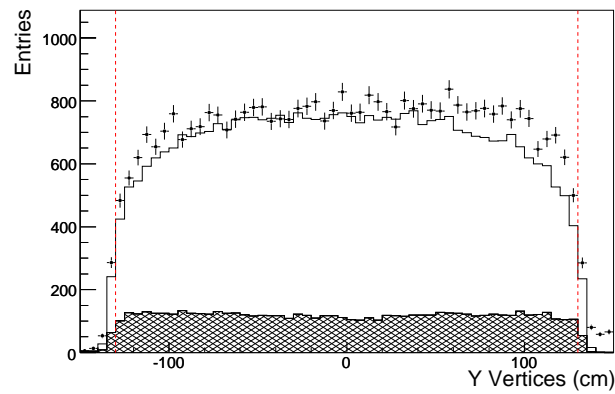
Figure 8.5 shows the interaction vertex distributions in the SciBar detector after applying the zero MRD tracks and 1<sup>st</sup> layer veto cuts. There is a uniform data excess in the  $x$ -projection due to cosmic rays. The cosmic ray excess in the  $y$ -projection is localised to positive values of  $y$ , i.e. vertices at the top of the detector. There is no cosmic ray excess in the upstream region of the  $z$  projection, this is due to the 1<sup>st</sup> layer veto cut. The data excess in the downstream region of the detector is due to cosmic rays. Requiring zero MRD tracks significantly reduces the cosmic ray background in the downstream regions of the detector. This is apparent in the small number of events in the penultimate layer of SciBar.

### Beam Timing Cut

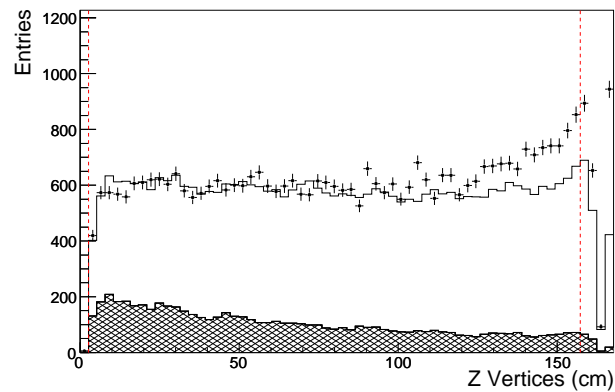
The SciBooNE beam window is  $2 \mu\text{s}$  long. The timing of each track is defined as the mean time of all hits associated with the track. For the one-track  $\mu$ , two-track



(a) X Vertex Distribution



(b) Y Vertex Distribution



(c) Z Vertex Distribution

**Figure 8.5:** The reconstructed vertex distributions in SciBar for all three projections after the zero MRD tracks and 1<sup>st</sup> layer veto cuts. The MC is separated into two SciBar generated events (white histogram), and dirt generated events (hatched histogram). The MC is normalised to the SciBar-MRD matched sample. Dashed lines indicated the fiducial volume limits.

$\mu+p$  and two-track  $\mu + \pi$  samples a tight beam-cut on this window is applied to all tracks. This is to remove all non-beam events from the data-set (mostly cosmic rays). For the two-track  $\mu+e$  sample, a simple beam timing cut can not be applied. This is because the muon has a lifetime of  $\sim 2 \mu\text{s}$ , therefore there is the possibility that the muon will decay outside the beam window producing the Michel electron. In this instance the beam timing cut is applied to the earlier, muon candidate, track only. Because of this difference in the beam timing cuts, the Michel temporal tag (MTT) method, outlined in section 7.1.3, is applied before the beam timing cut, to isolate  $\mu + e$  candidate events. Figure 8.6 shows the event timing distribution after the fiducial volume, veto and zero MRD track cuts. The cosmic background to each

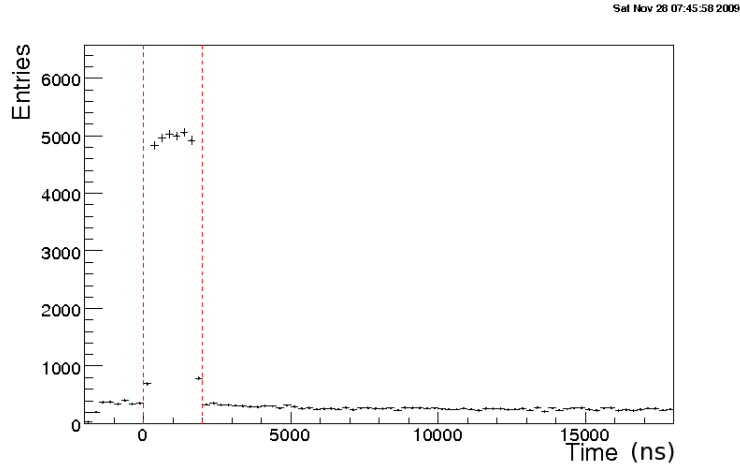


**Figure 8.6:** Event timing distribution of the SciBar-contained sample. Dashed lines indicated the  $2 \mu\text{s}$  beam window.

sample is estimated using the beam-off timing window, a  $2 \mu\text{s}$  window preceding the SciBooNE beam window.

### Summary of the SciBar Contained Sample

33,283 data events are selected for the SciBar-contained sample. The MC estimates a CCQE purity of 25%, with the dominant backgrounds from CC- $\pi$  production, NC elastic interactions and dirt events, A summary of the data and MC before and after applying the pre-cuts is shown in table 8.1.

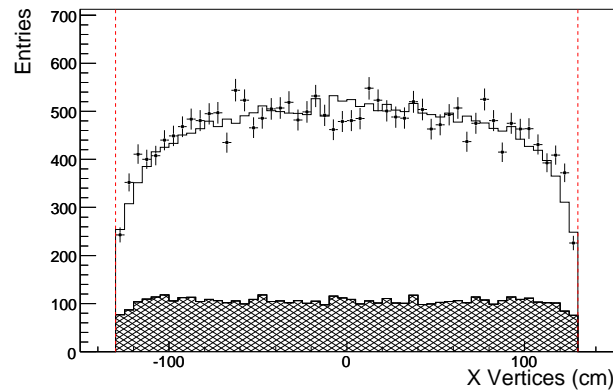
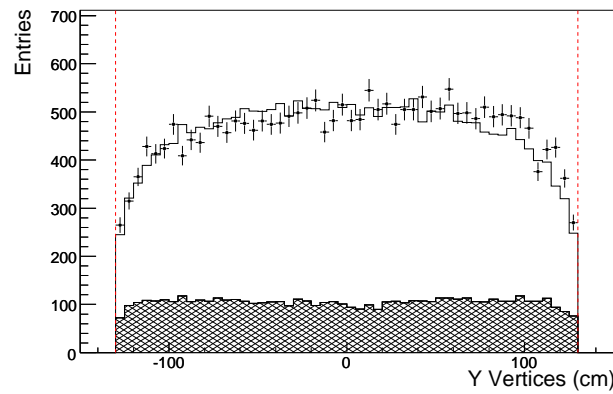
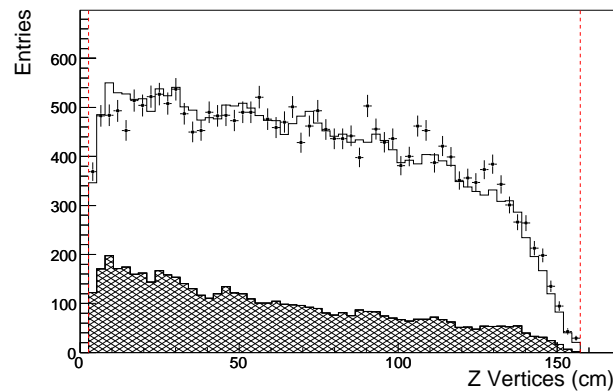
	Data	MC (%)					
		CCQE	CC- $\pi_{res}$	NC-El.	NC- $\pi_{res}$	Other	Dirt
<b>2<sup>nd</sup> Red.</b>	826,253	9.99	5.47	4.85	2.10	1.66	75.93
<b>After cuts</b>	33,283	25.28	17.96	24.25	10.77	3.32	18.42

**Table 8.1:** Data and MC summary before and after applying all the pre-cuts. The dirt background is greatly reduced by applying the first layer veto and fiducial volume cuts.

There is still a high dirt and NC elastic background after applying the pre-cuts; the majority of the dirt events come from neutron interactions within the detector. The dirt and NC elastic backgrounds are greatly reduced after applying muon tagging.

The interaction vertex distributions of the SciBar-contained sample for data and MC, after applying all pre-cuts, can be seen in figure 8.7. There is a good agreement between data and the normalised MC.

Figure 8.8 shows the MC  $p_\mu$  and  $\cos\theta_\mu$  distributions and selection efficiencies before (white histogram) and after (filled histogram) the SciBar-contained event selection. The SciBar contained-sample contains muons with momentum up to 600 MeV. The drop in the event selection efficiency seen in the  $\cos\theta_\mu$  distribution is due to the acceptance of the SciBar detector. Forward going muons penetrate the fiducial volume exclusion region and so are rejected. Figure 8.9 shows the true neutrino energy and momentum transfer before and after selection in the MC. The SciBar-contained sample contains neutrinos with energies up to 1 GeV. The median neutrino energy is around 400 MeV.

(a)  $x$  Vertex Distribution(b)  $y$  Vertex Distribution(c)  $z$  Vertex Distribution

**Figure 8.7:** The SciBar-contained reconstructed vertex distributions in SciBar for all three projections after applying all pre-cuts. The MC is separated into two event types; SciBar generated events (white histogram), and dirt generated events (hatched histogram). The MC is normalised to the SciBar-MRD matched sample. Dashed lines indicated the fiducial volume limits.

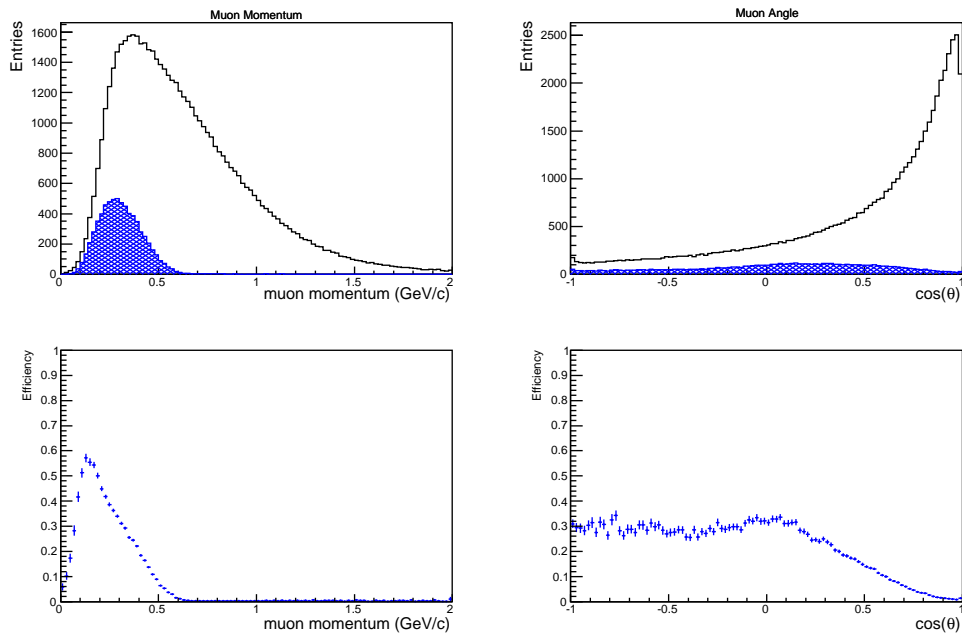


**Figure 8.8:** Muon momentum (top left) and angular (top right) distributions in MC before (white histogram) and after (hatched histogram) the SciBar-contained sample selection. The selection efficiencies are also shown (bottom left and right). The selected sample contains muons with momentum up to 600 MeV, with a median momentum of  $\sim 250$  MeV.

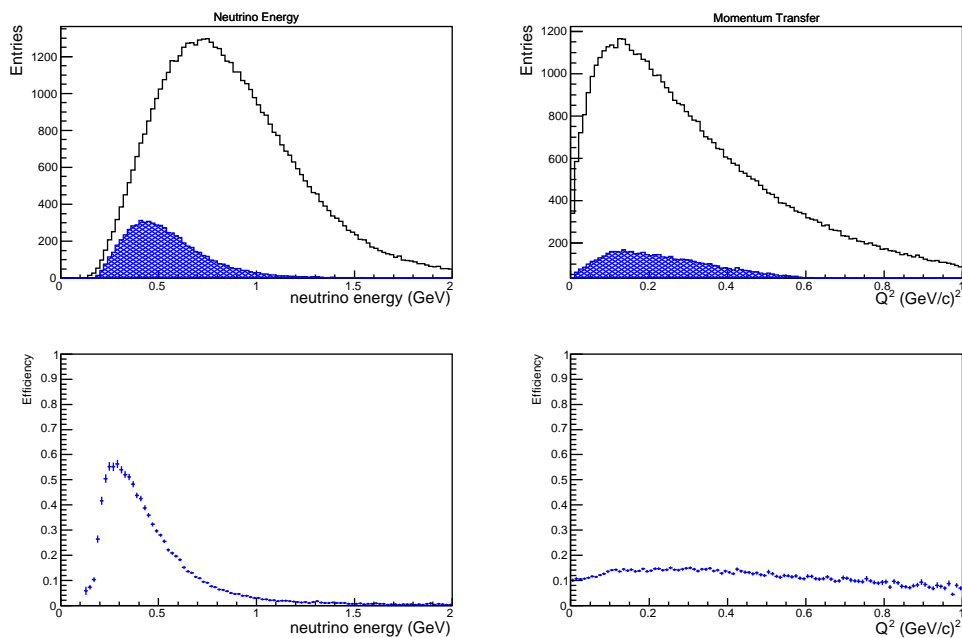


**Figure 8.9:** Neutrino energy (top left) and momentum transfer (top right) distributions in MC before (white histogram) and after (hatched histogram) the SciBar-contained sample selection. The selection efficiencies are also shown (bottom left and right). The selected sample contains neutrinos with energies up to 1 GeV, with a median energy of 400 MeV.

## Muon Tagging

After selecting the SciBar-contained sample, events are divided into one-track and two-track samples. The muon candidate events are then selected. For one-track events the ‘two single coincidences (TSC)’ muon tagging method, described in section 7.3, is applied. For two-track events the ‘Michel Temporal Tag (MTT)’, described in section 7.1.3, is applied to select the  $\mu+e$  candidate events<sup>1</sup>, and the TSC method is applied to select the  $\mu+p/\pi$  candidate events.

The TSC method is used to tag muon candidate events by searching for two single coincidences, one associated with the muon, the second associated with the Michel electron, between the horizontal (XZ) and vertical (YZ) views in SciBar. Figure 8.10 shows the reconstructed muon lifetime after muon tagging. The reconstructed muon lifetime is  $2.003 \pm 0.047^{stat} \mu\text{s}$ , in good agreement with experimental data [84].

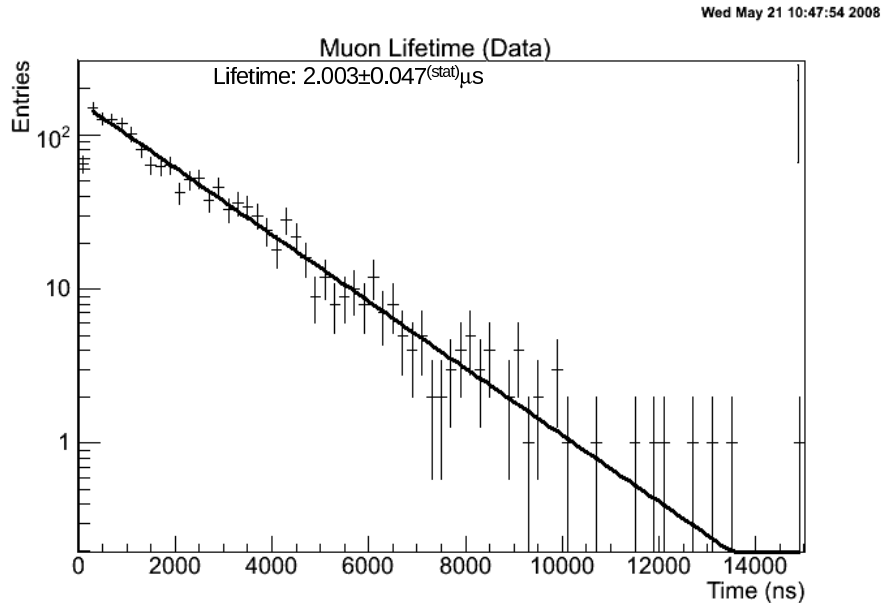


**Figure 8.10:** The reconstructed muon lifetime using the muon tagging timing information. The lifetime is measured to be  $2.003 \pm 0.047^{stat} \mu\text{s}$ , in good agreement with experimental data.

Figure 8.11(a) shows the difference between the reconstructed and true muon momentum, estimated using the MC simulation. The hatched histogram represents

<sup>1</sup>As explained in section 8.2, the two-track  $\mu+e$  candidate sample was isolated before applying the beam timing cut.

the CCQE events, the white histogram represents background events. The muon momentum resolution is approximately 42 MeV, estimated by fitting a Gaussian to the distribution. The momentum distribution is not symmetrical around zero; rather the reconstructed muon momentum is higher than the true momentum. This is due to other particles produced in the interaction interacting around the vertex. One track events are the dominant sample; in this case these hits get reconstructed as part of the muon track resulting in a larger reconstructed muon momentum than the true muon momentum. Figure 8.11(b) shows the difference between the reconstructed and true muon angle, estimated using the MC simulation. The hatched histogram represents the CCQE events, the white histogram represents the background events. The muon angle resolution is approximately 4 degrees, estimated by fitting a Gaussian to the distribution. The muon angle distribution is not symmetrical around zero; rather, the reconstructed muon angle is smaller than the true muon angle. This discrepancy comes from high angle events which are not reconstructed correctly due to the SciBooNE detector geometry.

Once the muon track has been identified the neutrino energy,  $E_\nu^{rec}$ , can be reconstructed using the muon kinematics

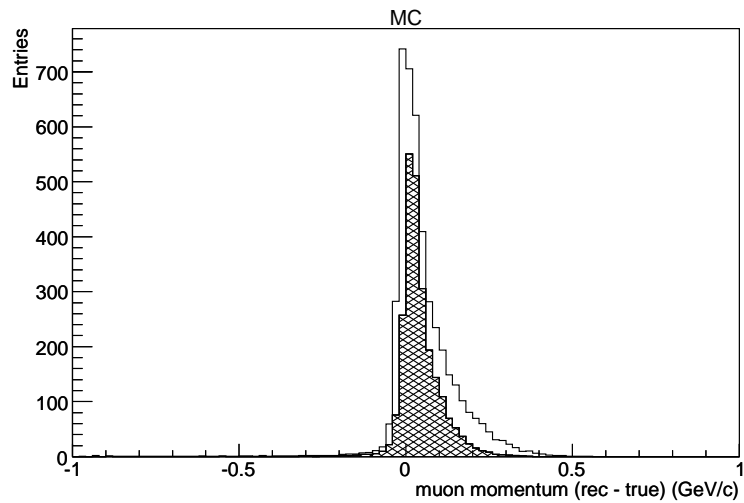
$$E_\nu^{rec} = \frac{1}{2} \frac{(m_p^2 - m_\mu^2) - (m_n - V)^2 + 2E_\mu(m_n - V)}{(m_n - V) - E_\mu + p_\mu \cos \theta_\mu}. \quad (8.3)$$

Where  $V$  is the nuclear potential set to 27 MeV,  $m_p$ ,  $m_n$  and  $m_\mu$  are the proton, neutron and muon mass, respectively.  $E_\mu$ ,  $p_\mu$  and  $\theta_\mu$  are the muon energy, momentum and angle, respectively. The momentum transfer,  $Q^2$ , can also be reconstructed from the muon kinematics

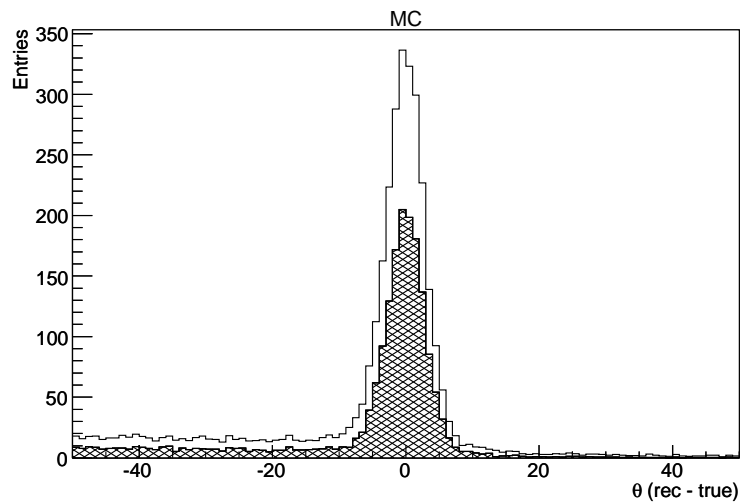
$$Q_{rec}^2 = 2E_\nu^{rec}(E_\mu - p_\mu \cos \theta_\mu) - m_\mu^2. \quad (8.4)$$

Derivations of  $E_\nu^{rec}$  and  $Q_{rec}^2$  can be found in appendix A.1.

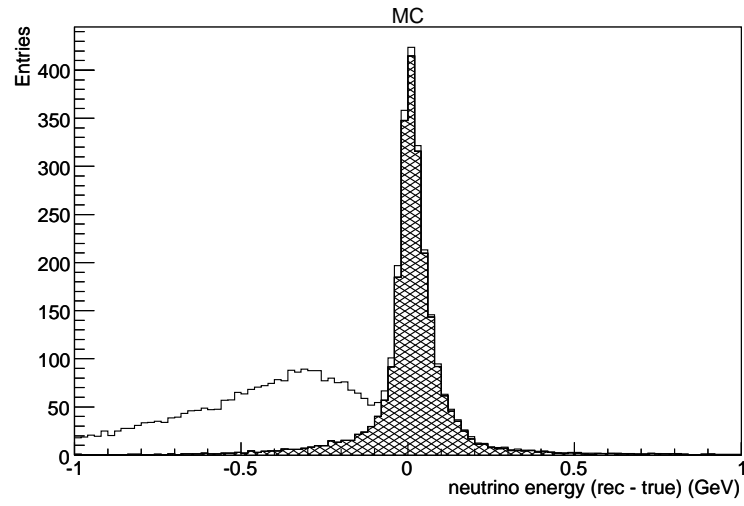
Figure 8.12(a) and figure 8.12(b) show the difference in the reconstructed and true neutrino energy and momentum transfer, estimated using the MC simulation, respectively. The hatched histogram represents the CCQE events, the white histogram represents the background events. The reconstructed neutrino energy is only valid for CCQE interactions, hence the asymmetry in the background distribution in figure 8.12(a).



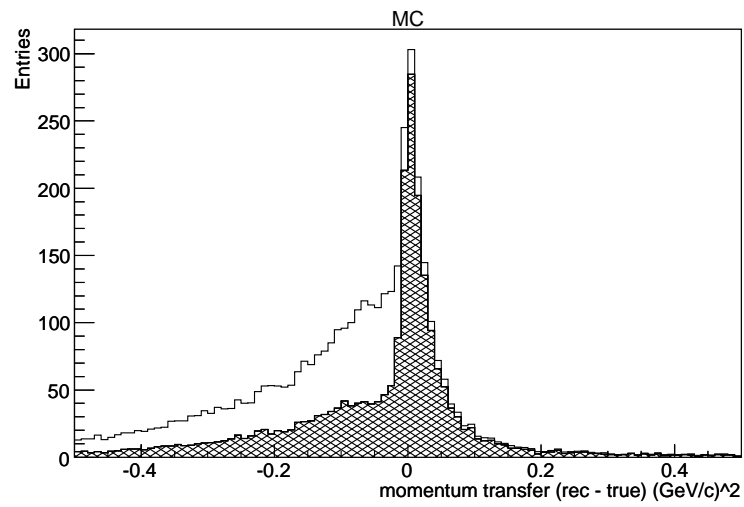
(a) Muon Momentum (rec - true)

(b)  $\cos\theta_\mu$  (rec - true)

**Figure 8.11:** Difference between, (a) the reconstructed and true muon momentum, (b) the reconstructed and true muon angle, with respect to the beam direction ( $z$  axis), estimated using the MC simulation. The hatched histogram shows the CCQE contribution, the white histogram shows the background contribution.



(a) Neutrino Energy



(b) Momentum Transfer

**Figure 8.12:** Difference between, (a) the reconstructed and true neutrino energy,  $E_{\nu}^{rec}$ , (b) the reconstructed and true momentum transfer,  $Q^2$ , estimated using the MC simulation. The hatched histogram shows the CCQE contribution, the white histogram shows the background contribution.

### 8.2.1 Event Classification

After muon tagging five particle identification cuts are used to isolate each sample. They are:

- Track separation (applied to all samples)
- Event topology: p/e separation ( $\mu+p$  sample)
- MuCL:  $dE/dx$  p/ $\pi$ (or  $\mu$ ) separation (applied to all samples)
- Vertex activity (applied to  $\mu$  and  $\mu+e$  samples)
- CCQE kinematic cut (applied to  $\mu+p$  sample)

A schematic of the event classification is shown in figure 8.13

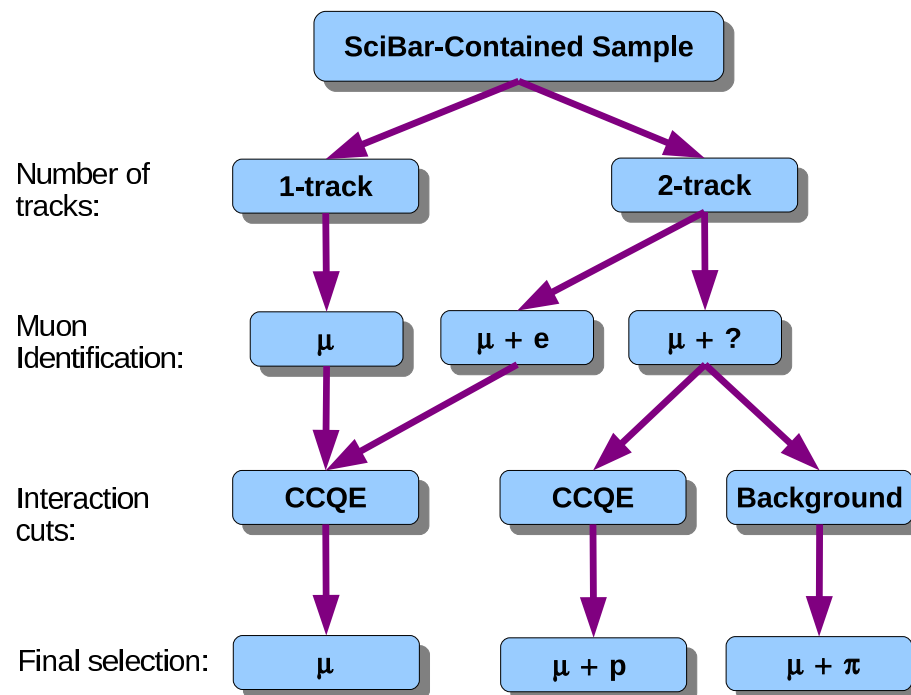
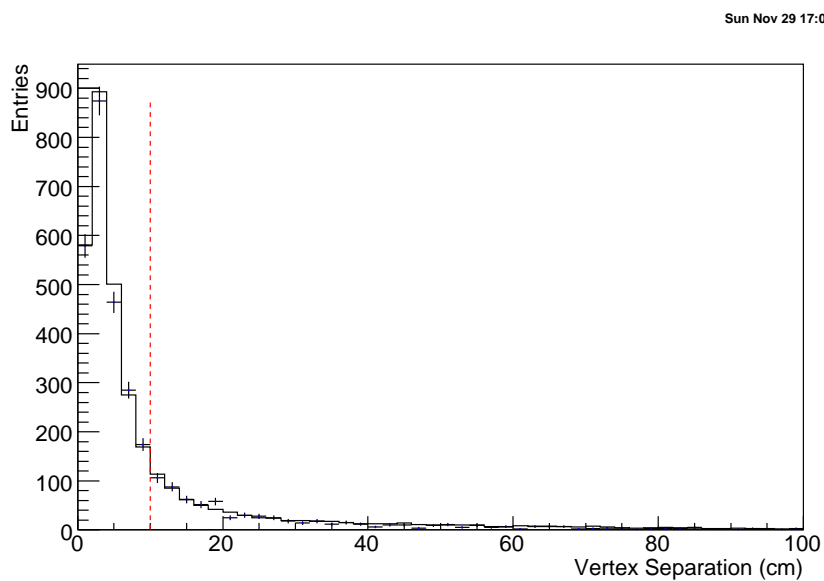


Figure 8.13: Schematic of the event classification.

### Track Separation

To select multi-track events a track separation cut is applied. If two tracks are considered to be from the same event a separation between vertices of less than 10 cm is required. Figure 8.14 shows the track separations for all two-track events in the SciBooNE data-set. To account for the possibility that a track direction is mis-reconstructed, all track vertices are considered with the cut applied to the smallest vertex separation.



**Figure 8.14:** The vertex separation for the two-track sample for data (data points) and MC (histogram). The dashed line represents the vertex separation cut. The MC is normalised to the SciBar-MRD matched sample.

### p/e Separation using Event Topology

The muons in the  $\mu+e$  and  $\mu+p$  samples are identified using the MTT and TSC methods, respectively. However, there is an intrinsic background of  $\mu+e$  events in the  $\mu+p$  sample. This background comes from two sources, prompt muon decay and event mis-reconstruction. For prompt muon decay, the resultant Michel electron would be within the 50 ns cut used by the MTT method. The number of  $\mu+e$

candidates in this 50 ns window can be calculated

$$N = N_0 (1 - e^{-t/\tau}) \quad (8.5)$$

$$N = 100\% \times (1 - e^{-50.0/2026.3}) = 2.44\%$$

This is a small contamination to the data-set. Event mis-reconstruction is the more significant effect. All 32 channels in a TDC block have the same TDC information. To determine the mean time for a track the average time for each hit in that track is taken. In SciBar the TDCs have multi-hit capability, however for the track timing reconstruction only the first TDC hit in a TDC block is used. Therefore if a Michel electron is produced in a TDC block, after 50 ns, and tracks back through the TDC blocks hit by the muon, the time given to this track would be the same as the muon track. The number of events of this type is dependent on Michel electron direction and the ADC gate width. The ADC windows for all channels in a TDC block are opened after the first hit in the TDC block with a typical ADC gate width of  $1.2 \mu\text{s}$ . Therefore  $\sim 45\%$  of events with a Michel electron tracking in the muon TDC blocks will not be identified. An example of this type of event can be seen in figure 8.15. The  $dE/dx$  distribution for an electron and proton track are very similar, and so

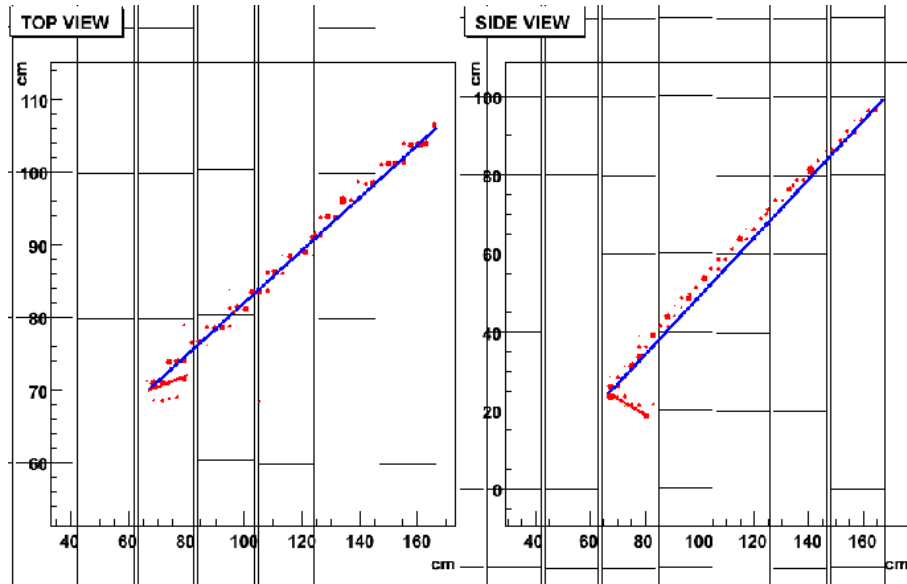


**Figure 8.15:** Event display showing the Michel electron track in the same TDC block as the muon track in the top view (left). The Michel electron time will be mis-reconstructed to be identical to the muon time.

cannot be used to separate these events. Instead an event topology cut is applied.

Figure 8.16 shows the six theoretical event signatures for  $\mu+p$  and  $\mu+e$  events. The difference between topologies two and three (and five and six) is the direction of the Michel electron which can be emitted isotropically because the muon decays at rest. The track direction is determined using the timing information from the hits associated with the tracks start and end vertices. If the start vertices of both tracks are separated by more than 10 cm the event is removed from the  $\mu+p$  sample. If the event can not be categorised by any of the six event topologies the event is also rejected.

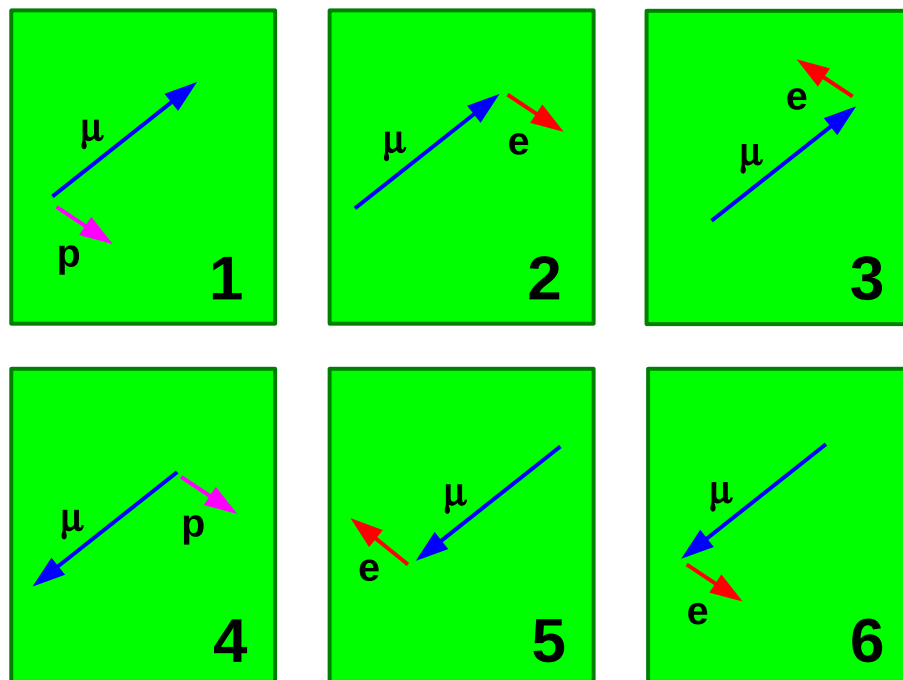


**Figure 8.16:** There are six possible event topologies for  $\mu+p$  and  $\mu+e$  events. Numbers 1 and 4 are  $\mu+p$  topologies, numbers 2,3,5 and 6 are  $\mu+e$  topologies.

### Muon Confidence Level

SciBar has the capability to separate protons from pions using  $dE/dx$  information. A muon confidence level (MuCL) is constructed to separate minimum ionising particles (MIPs), such as muons and pions, from non-MIPs such as protons. The MuCL method was originally developed for SciBar by the K2K collaboration [52]. The method to calculate the MuCL for a track in SciBooNE was developed by K. Hiraiide [46]. To construct the MuCL for a track, the confidence level that a particle

is identified as a MIP is calculated on a plane-by-plane basis. The confidence level at each plane is defined as the fraction of events in the expected  $dE/dx$  distribution for muons above the observed value,  $(dE/dx)_{obs}$ . The expected  $dE/dx$  distribution for muons is obtained using cosmic-ray muon data as shown in figure 8.17(a). The confidence level for each plane is obtained using the cumulative  $dE/dx$  distribution function for cosmic muons and is shown in figure 8.17(b).

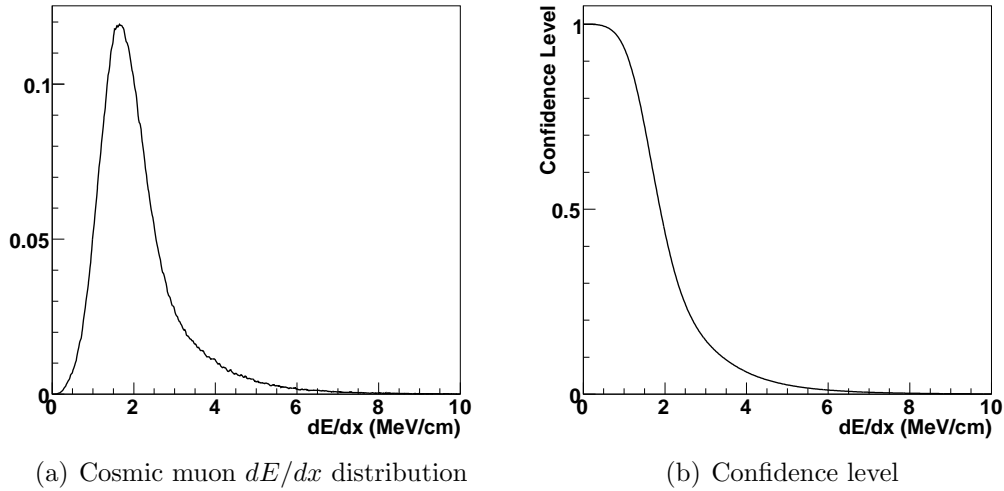


**Figure 8.17:** (a) Expected  $dE/dx$  distribution for a cosmic ray muon. (b) The confidence level as a function of  $dE/dx$  observed in a scintillator plane.

To calculate the total MuCL value for a track, the confidence levels for each plane penetrated by the track are combined. Assuming the confidence for each plane is independent, the MuCL is defined as:

$$\text{MuCL} = P \times \sum_{i=0}^{n-1} \frac{(-\ln P)^i}{i!} \quad (8.6)$$

where  $n$  is the number of planes penetrated by the track and  $i$  is the  $i^{\text{th}}$  plane.  $P = \prod_{i=1}^n CL_i$ , where  $CL_i$  is the confidence level for the  $i^{\text{th}}$  plane. The MuCL value is affected by a number of inefficiencies. These include noise hits in the detector and deposited energy from other particles. To avoid the effect of the cross-talk from the MA-PMTs and inefficiency from the scintillator planes, planes with less than 6 photo-electrons are excluded from the MuCL calculation. If there are overlapping

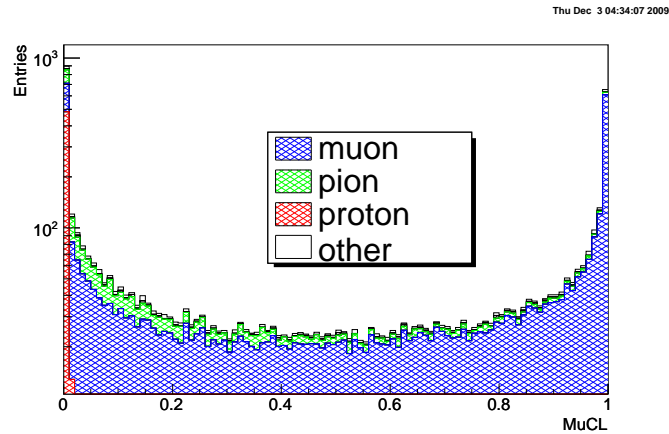
---

tracks in one view, all hits in the overlapping view are excluded. Pions and muons are only MIP like particles when they have a high  $\beta$  value. As they come to rest they can no longer be considered to be MIPs. To prevent large (small) outliers from skewing the MuCL value for a track, and to account for particles coming to rest in the detector, the confidence levels for each plane are sorted in terms of size, with the largest 10% and smallest 50% excluded from the calculation.

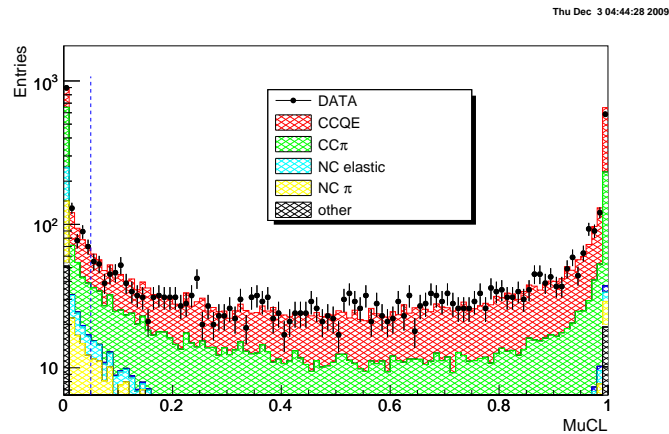
The one-track and two-track  $\mu + e$  samples are combined before applying the MuCL cut; this is defined as the muon sample. Figure 8.18(a) shows the expected MuCL distribution for different particle types, estimated using the MC simulation for the muon candidate track in the muon sample. Figure 8.18(b) shows the MuCL distribution for data and MC in the one-track sample. Muon candidate tracks with a MuCL value greater than 0.05 are retained.

For the two-track  $\mu + p$  sample a MuCL cut is applied to both tracks; the track with the larger MuCL value is tagged as the muon candidate track. Figure 8.19 shows the MuCL distribution for different particle types, estimated using the MC simulation for the proton candidate track in the  $\mu + p$  sample. Figure 8.20 show the MuCL distributions for the muon candidate and proton candidate tracks. Two cut values are applied; events with a MuCL value less than 0.05 for the proton candidate track and MuCL value greater than 0.9 for the muon candidate track are retained as the  $\mu + p$  sample. Events rejected by these cuts make up background sample, which is dominated by  $\mu + \pi$  events.

---



(a)



(b)

**Figure 8.18:** (a) The MuCL distribution for different particle types for the one-track sample, estimated using the MC simulation. (b) The MuCL distribution for data and MC, the MC is separated into interaction types. Events with  $\text{MuCL} > 0.05$  are retained.

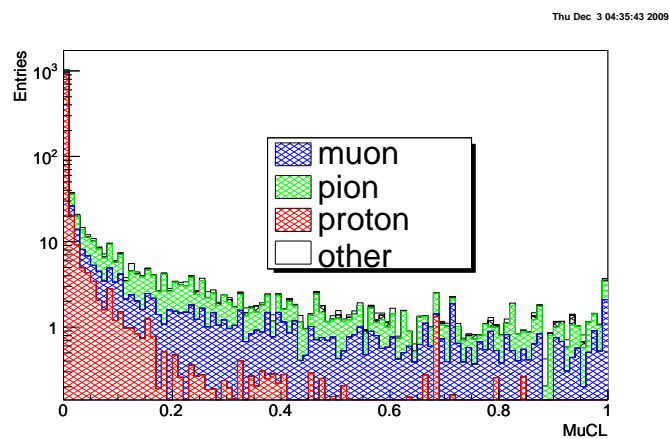
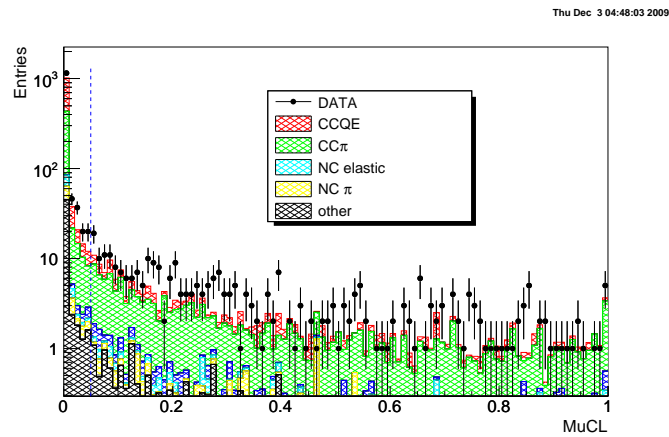
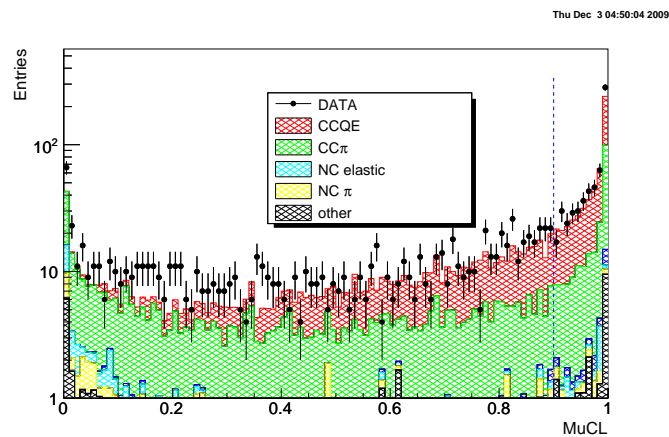


**Figure 8.19:** The MuCL distribution for different particle types for the proton candidate track in the two-track sample, estimated using the MC simulation.



(a) proton candidate MuCL



(b) muon candidate MuCL

**Figure 8.20:** (a) The data and MC MuCL distributions for proton candidate tracks; the MC is separated into interaction types. Events with  $\text{MuCL} < 0.05$  are retained. (b) The data and MC MuCL distributions for muon candidate tracks; the MC is separated into interaction types. Events with  $\text{MuCL} > 0.9$  are retained.

### Vertex Activity

To further enhance the CCQE purity a vertex activity cut is applied. In a CCQE event the proton is often not reconstructed because of its low energy. For the CC- $\pi$  background, two particles are produced at the vertex, a pion and a proton, sharing the energy transferred from the interaction. It is therefore possible to remove some of the background events by retaining events with a large energy deposit in a scintillator bar close to the vertex, associated with the proton. A  $12.5 \times 12.5$  cm<sup>2</sup> box, corresponding to a  $5 \times 5$  channel array, is defined around the interaction vertex in both views. The largest energy deposit in a scintillator bar is then determined. Figure 8.21 shows the vertex activity for the muon sample. A cut at 6 MeV is applied to remove low energy deposits associated with background events.

Wed Apr 7 16:49:43 2010

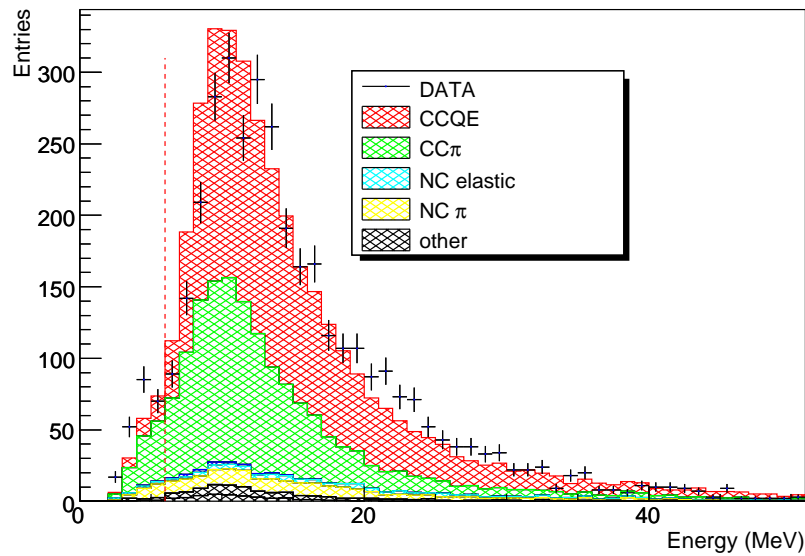


**Figure 8.21:** The vertex activity for the muon sample. CCQE events are shown in red, CC- $\pi$  events are shown in green. NC- $\pi$  events are shown in yellow. The red dashed line represents the optimised cut value. The MC is POT normalised.

### CCQE Kinematic Cut

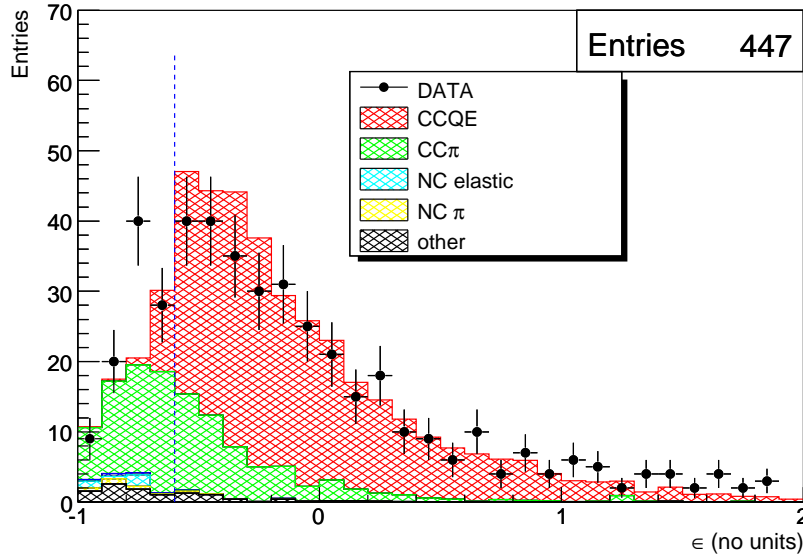
The two-track CCQE sample is further optimised using a CCQE kinematic cut. The muon kinematics are used to reconstruct the neutrino energy. This assumes an elastic interaction. In the case of CC- $\pi$  events and other inelastic backgrounds the

reconstructed neutrino energy is smaller than the true neutrino energy, this can be seen in figure 8.12(a). For two-track events in SciBar it is possible to reconstruct the neutrino energy using the deposited energy from the proton and muon. By comparing the reconstructed neutrino energy with the energy deposited in the detector CCQE and background events can be separated. A parameter,  $\epsilon$ , can be defined as:

$$\epsilon = \frac{E_{\nu}^{rec} - T_{\mu}^{depo} - m_{\mu} - T_p^{depo}}{T_p^{depo}} \quad (8.7)$$

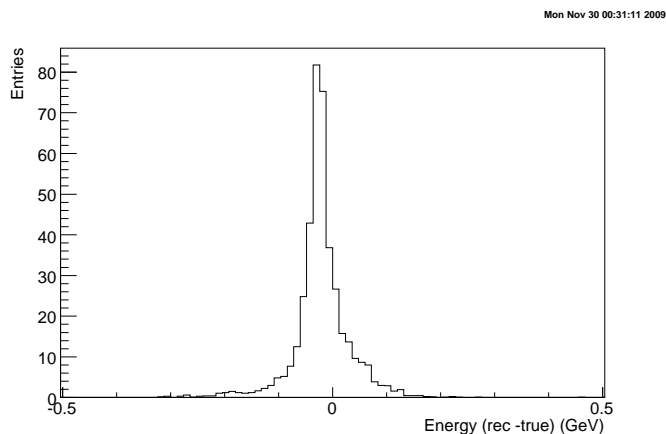
Where  $E_{\nu}^{rec}$  is the reconstructed neutrino energy using muon kinematics,  $T_{\mu}^{depo}$  is the muon kinetic energy calculated from the deposited energy associated with the muon,  $T_p^{depo}$  is the proton kinetic energy calculated from the deposited energy associated with the proton, and  $m_{\mu}$  is the muon mass.  $T_p^{depo}$  is used to normalise the difference between the reconstructed and deposited energies for events with different neutrino energies. Figure 8.22 shows the  $\epsilon$  distribution for the  $\mu + p$  sample, with the MC normalised to the protons on target. The difference in the true proton kinetic energy

Wed Apr 7 17:01:59 2010



**Figure 8.22:** The  $\epsilon$  distribution in data and MC. Events with  $\epsilon > -0.6$  are retained. The MC is POT normalised.

and the reconstructed proton kinetic energy estimated using the MC simulation is shown in figure 8.23. The proton resolution is 32 MeV with a mean of 20 MeV, estimated by fitting a Gaussian to the distribution. Variations in the  $\epsilon$  distribution

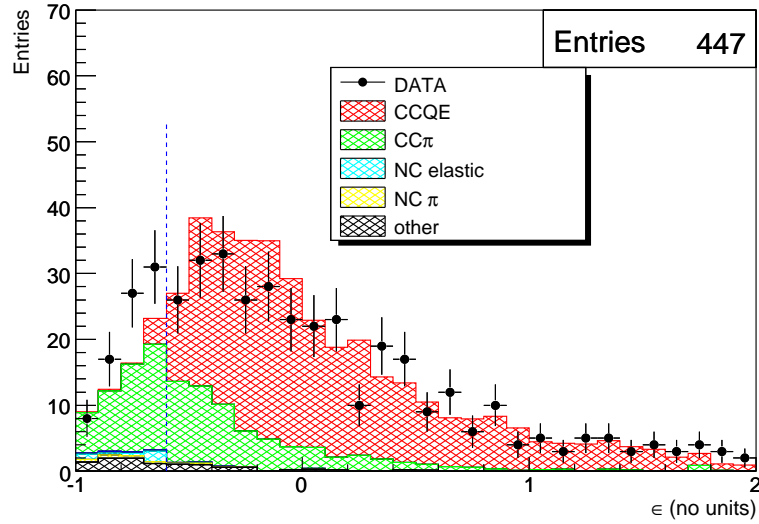


**Figure 8.23:** The difference between the true proton kinetic energy,  $T_p^{true}$ , and the reconstructed proton kinetic energy,  $T_p^{rec}$ , estimated using the MC simulation. A Gaussian is fitted to the distribution to estimate the resolution.

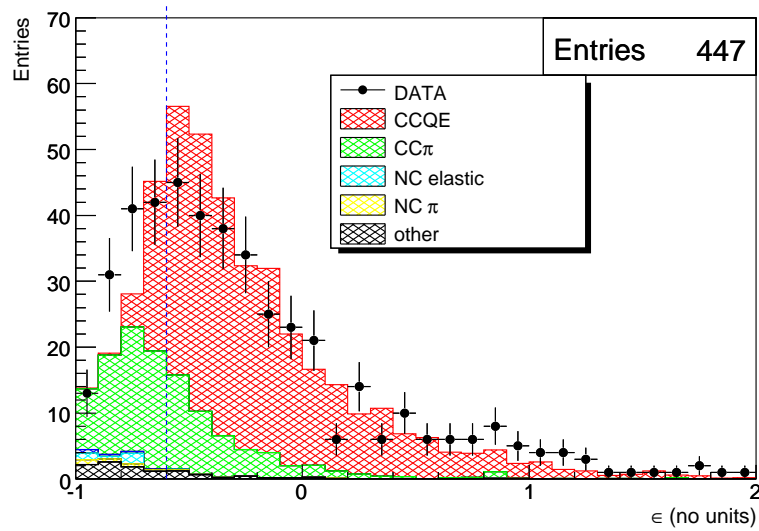
	Before Cut	$T_p$	$T_p - T_p^{res}$	$T_p + T_p^{res}$
data	447	349	363	319
CCQE	71.1%	83.4%	81.3%	84.7%
Bkgd	28.9%	16.6%	18.7%	15.3%

**Table 8.2:** Effect of  $T_p$  resolution on the CCQE kinematic cut. The purity of CCQE events is unaffected by the resolution. The number of events in data varies by +14 and -30 for an decrease and increase in  $T_p$  by  $T_p^{res}$ , respectively. For a sample of 349 events the statistical uncertainty, is  $\sqrt{439} = 18.6$ . The variations are within the uncertainty.

Wed Apr 7 16:56:56 2010

(a)  $T_p - T_p^{res}$ 

Wed Apr 7 16:56:29 2010

(b)  $T_p + T_p^{res}$ 

**Figure 8.24:** The  $\epsilon$  distributions when the proton kinetic energy,  $T_p$ , is, (a) increased and (b) decreased, by the proton kinetic energy resolution,  $T_p^{res}$ .

can be constructed using the proton kinetic energy resolution and can be seen in figure 8.24.

The proton kinetic energy resolution is sufficient to separate CCQE and background events. A cut on  $\epsilon > -0.6$  is applied.

### 8.2.2 Event Selection Summary

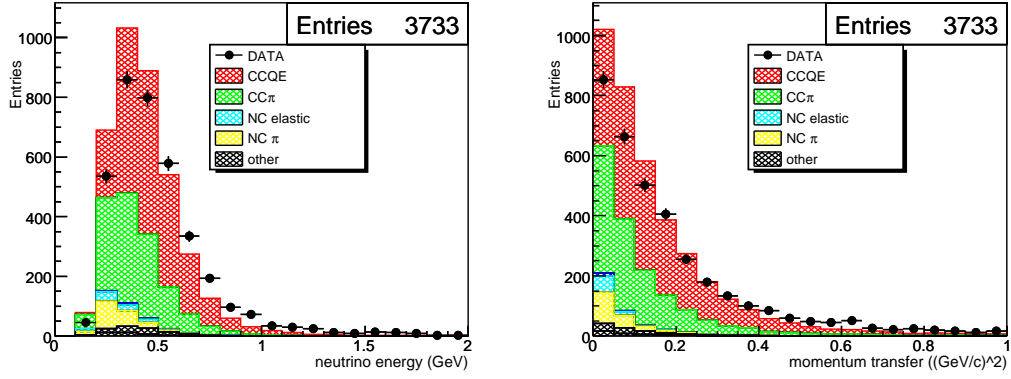
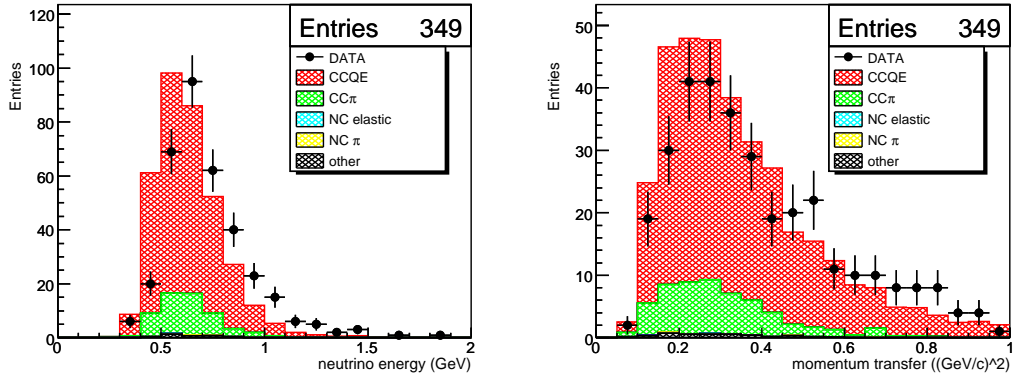
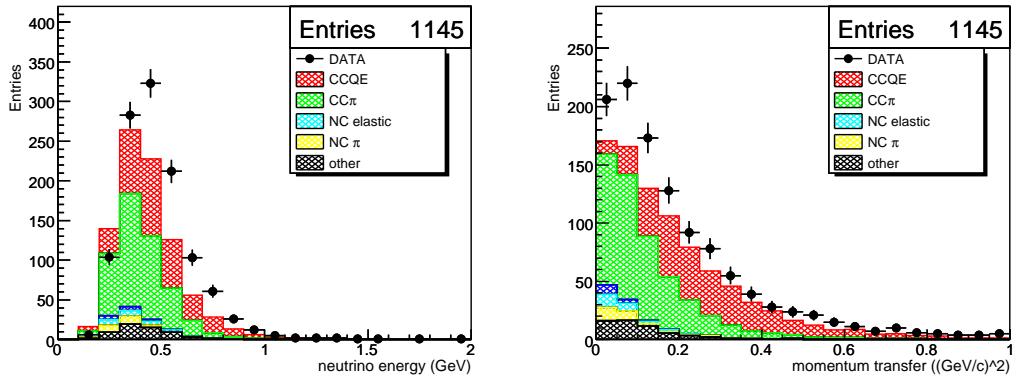
A breakdown of the samples can be seen in table 8.3. The largest sample is the muon sample with 3733 events and an estimated CCQE purity of 56.0%. The two-track  $\mu + p$  sample has 349 events with an estimated CCQE purity of 83.4%. The  $\mu + \pi$  sample that will be used to constrain background events in the fit has 1145 events with a CC- $\pi$  purity of 47.1%. Figure 8.25 shows the reconstructed neutrino energy

Sample	Data	Est. Cosmic Background	MC (%)			
			CCQE	CC- $\pi_{res}$	Other	Dirt
$\mu, \mu + e$	3733	38	56.0	33.6	9.0	1.4
$\mu + p$	349	0	83.4	15.2	1.4	0.0
$\mu + \pi$	1145	0	38.9	47.1	13.5	0.5

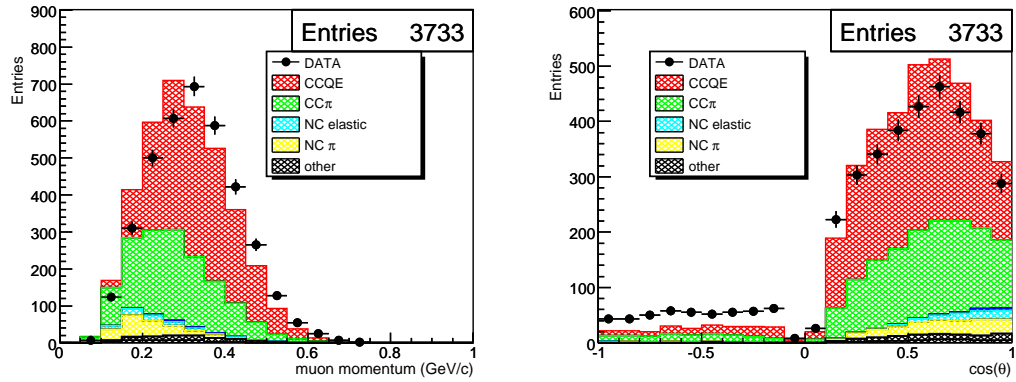
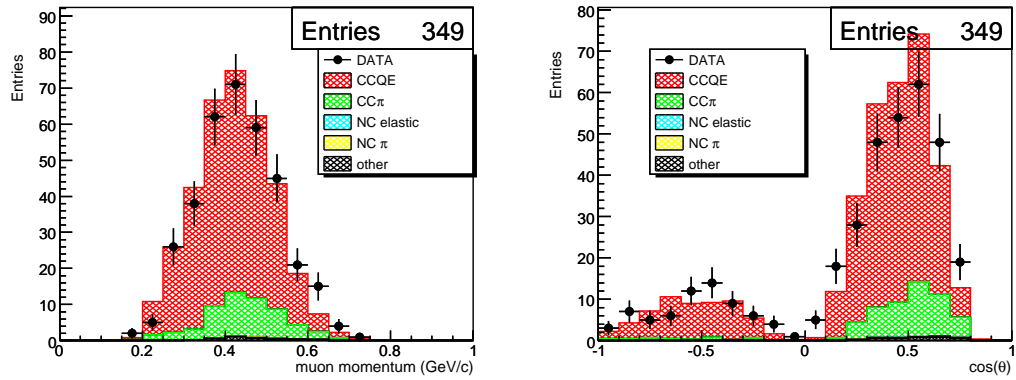
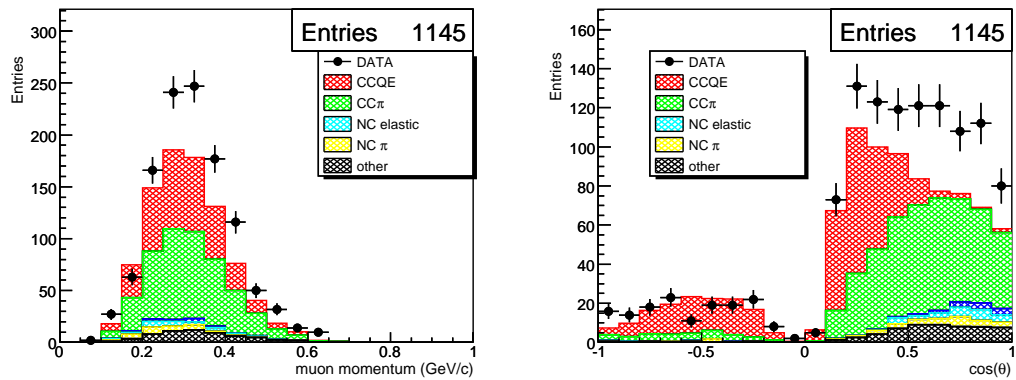
**Table 8.3:** A summary of the two SciBar-contained CCQE samples and one SciBar-contained background sample after all cuts are applied.

and momentum transfer for the  $\mu$ ,  $\mu + p$ , and  $\mu + \pi$  samples. Figure 8.26 shows the muon momentum and cosine of the muon angle for the  $\mu$ ,  $\mu + p$ , and  $\mu + \pi$  samples.

In general there is poor agreement between the data and MC distributions for all three samples, with a data deficit in the muon sample and a data excess in the  $\mu + \pi$  sample. The  $\cos\theta_\mu$  distributions in figure 8.26 agree well, shape-wise for the two two-track samples, especially for backwards tracks (negative  $\cos\theta_\mu$ ). This is not the case for the one-track sample, where an excess of 453 data events is seen for backwards tracks; compared with the 235 events predicted by the MC simulation.

(a) Combined  $\mu$  &  $\mu + e$  samples(b)  $\mu + p$  sample(c)  $\mu + \pi$  sample

**Figure 8.25:** The  $E_{\nu}^{rec}$  (left) and  $Q_{rec}^2$  (right) data and MC distributions for (a)  $\mu$  sample, (b)  $\mu + p$  sample, (c)  $\mu + \pi$  sample. The MC is POT normalised.

(a) Combined  $\mu$  &  $\mu + e$  samples(b)  $\mu + p$  sample(c)  $\mu + \pi$  sample

**Figure 8.26:** The  $p_\mu$  (left) and  $\cos\theta_\mu$  (right) data and MC distributions for (a)  $\mu$  sample, (b)  $\mu + p$  sample, (c)  $\mu + \pi$  sample. The MC is POT normalised.

## 8.3 Backwards Track Anomaly

Figure 8.26 shows an excess in backwards tracks in the one-track sample; this excess is not seen in either of the two-track samples where there is a good data/MC agreement. 453 events are seen in data, the MC simulation predicts 235 events. This excess is due to either discrepancies in the detector simulation or from physics not modelled in the NEUT MC. If the TDC-to-TDC timing discrepancies is larger in data than MC, short tracks in the data could be reconstructed in the incorrect direction more often than in the MC. Equally, high angle tracks which are only partially reconstructed as short tracks could also be mis-reconstructed in the same manner. Figure 8.27 shows the track length and track angle distributions for the backwards track data and MC. There is no asymmetry in the data/MC track angle ratio; the asymmetry in the data/MC track length ratio is for medium length tracks. Given the small data-set neither distribution point towards the TDC-to-TDC timing discrepancies being the cause of the data excess.

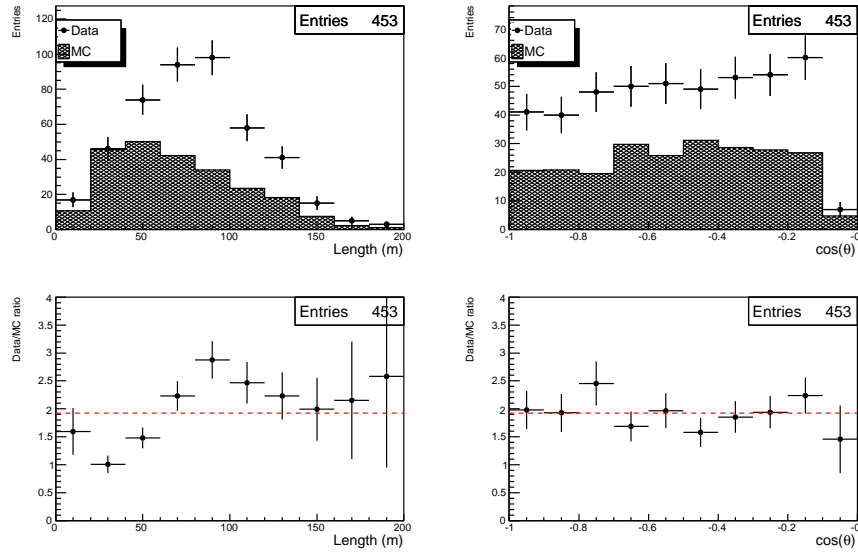


**Figure 8.27:** Backwards one-track data (data points) and MC (hatched histogram) distributions. (Top left) track length, (bottom left) data/MC track length ratio, (top right) track  $\cos(\theta)$ , (bottom right) data/MC track  $\cos(\theta)$  ratio. The MC is normalised to POT. 453 events are seen in data, 236 events are expected according to MC.

Another possibility for the excess could arise from inaccurate modelling of the detector noise in the MC simulation. The track direction is determined using the

timing information for each hit. However, although the SciBar TDCs have multi-hit capability, only the first timing hit in each TDC block is used to determine the hit time. It is possible for a noise hit to occur before the muon penetrates the TDC, resulting in an incorrect track time. This could result in a forward-going track being reconstructed as a backward-going track. If the number and size of noise hits in data is larger than in MC, this would result in the discrepancy seen in figure 8.26(a). Figure 8.28 shows the time difference between the first hit associated with the track and the muon coincidence determined using the TSC method, described in section 7.3. If the track is forward-going then the muon coincidence will

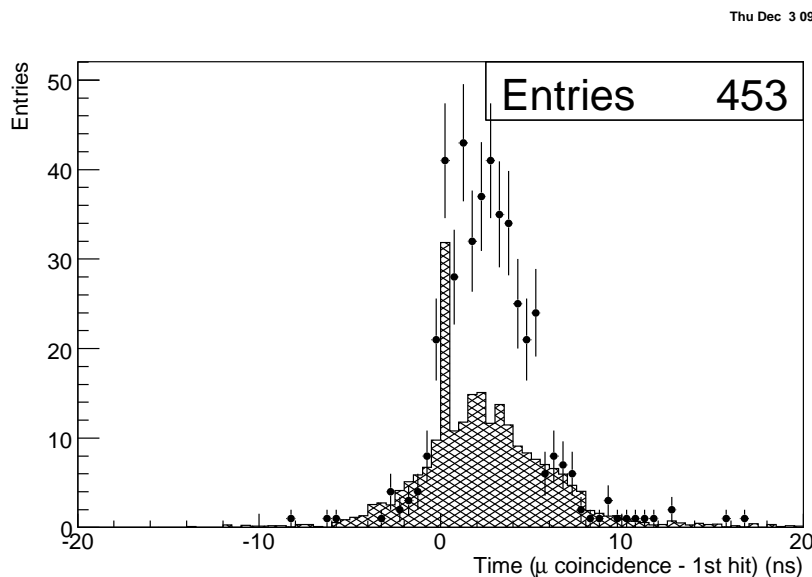


**Figure 8.28:** Difference in the muon coincidence time and the 1<sup>st</sup> track hit time for data (data points) and MC (hatched histogram). The excess of data is predominantly for positive time differences suggesting that the excess is not due to track direction mis-reconstruction.

occur before or at the same time as the 1<sup>st</sup> hit associated with the track, it is clear from figure 8.28 that the majority of events have a timing signature suggestive of them being truly backwards-going.

The results of the backwards track study, including an eye scan of 100 events in data and MC, proved inconclusive. The excess could be due to physics not modelled in the MC; however reconstruction effects have not been ruled out. Because of this anomaly, a fit including and excluding backwards tracks will be calculated.

---

# Chapter 9

## CCQE Cross Section Measurement

### 9.1 Cross-Section Extraction

#### 9.1.1 Cross-Section Extraction Overview

The largest uncertainty for most neutrino cross-section experiments is the neutrino beam flux. Because the Booster neutrino beam flux is well understood, it is possible to calculate the absolute cross-section for CCQE interactions in SciBooNE. Presented here is the absolute cross-section for the SciBar-contained sample. Although this sample is small in comparison to the SciBar-MRD matched sample, this is a good test of the tools that will be used to extract the cross-section for the combined sample.

In this analysis, the data and MC are described by two variables,  $p_\mu$  and  $\theta_\mu$ . A maximum likelihood fit based on Poisson statistics is performed to determine the absolute cross-section. A series of systematic studies are performed to determine the systematic error on the cross-section.

#### 9.1.2 Poisson Maximum Likelihood

To extract the cross-section, MC distributions are fitted to data distributions using a Poisson maximum likelihood. For  $N$  bins, where  $n_i$  is the number of observed

---

events in the  $i^{\text{th}}$  bin and  $\mu_i$  is the MC prediction for the number of events in the  $i^{\text{th}}$  bin, which depends on parameters  $\vec{\theta}$ , the likelihood ratio,  $\lambda(\vec{\theta})$ , is

$$\lambda(\vec{\theta}) = \frac{f(\vec{n}, \vec{\mu}(\vec{\theta}))}{f(\vec{n}, \vec{n})}, \quad (9.1)$$

where  $f(\vec{n}, \vec{\mu}(\vec{\theta})) = \prod_i^N P(n_i, \mu_i(\vec{\theta}))$  is the Poisson probability of observing  $n_i$  events when  $\mu_i$  are expected, and  $f(\vec{n}, \vec{n}) = \prod_i^N P(n_i, n_i)$  is the Poisson probability of observing  $n_i$  events when  $n_i$  events are expected. To maximise  $\lambda$  is equivalent to minimising  $-2 \ln \lambda$  [85], therefore we can define  $F_{poisson}$  as

$$\begin{aligned} F_{poisson} &= -2 \ln \lambda \\ &= 2 \sum_i \left[ \mu_i(\vec{\theta}) - n_i + n_i \ln \frac{n_i}{\mu_i(\vec{\theta})} \right]. \end{aligned} \quad (9.2)$$

A derivation of equation 9.2 can be found in appendix A.2.

$F_{poisson}$  is expected to be distributed as a  $\chi^2$  with degrees of freedom equal to the number of bins minus the number of constraints. The form of  $F_{poisson}$  is only true when  $n_i$  and  $\mu_i$  are non-zero. Since we are counting events, neither  $n_i$  or  $\mu_i$  are negative. If  $n_i = 0$  and  $\mu_i > 0$  then

$$F_{poisson}^i = 2\mu_i \quad (9.3)$$

If  $n_i > 0$  and  $\mu_i = 0$  then

$$F_{poisson}^i = \text{undefined}. \quad (9.4)$$

The expected number of events,  $\mu_i$ , comes from the MC, with the observed number of events,  $n_i$ , coming from the data. We generate approximately ten times more MC. This reduces the possibility of equation 9.4.

We use  $p_\mu$  vs.  $\theta_\mu$  distributions to describe the data and MC. Therefore equation 9.2 can be rewritten as

$$F_{poisson} = 2 \sum_s \sum_i \left[ N_{i,s}^{exp} - N_{i,s}^{obs} + N_{i,s}^{obs} \ln \frac{N_{i,s}^{obs}}{N_{i,s}^{exp}} \right] \quad (9.5)$$

Where  $N_{i,s}^{exp}$  and  $N_{i,s}^{obs}$  are the number of expected events and observed events, respectively, in the  $i^{\text{th}}$  bin of the  $p_\mu$  vs.  $\theta_\mu$  distribution for sample  $s$ . We can introduce fitting parameters into the  $N_{i,s}^{exp}$  distributions that are allowed to fluctuate in the fit to maximise the likelihood ratio.  $N_{i,s}^{exp}$  can be rewritten in terms of signal and background contributions. By introducing fitting parameters,  $F_N$ ,  $a_k$  and  $a_{bkgd}$ ,  $N_{i,s}^{exp}$  can be re-expressed as

$$N_{i,s}^{exp} = F_N \left[ \sum_k a_k N_{i,s}^{ccqe} + a_{bkgd} N_{i,s}^{bkgd} \right] \quad (9.6)$$

$F_N$  adjusts the overall data/MC normalisation,  $a_{bkgd}$  adjusts the contribution from background events, and  $a_k$  adjusts the contribution from CCQE events in the  $k^{\text{th}}$  neutrino energy bin. By binning  $N_{i,s}^{CCQE}$  in true neutrino energy bins, the CCQE cross-section as a function of true neutrino energy can be extracted. The new CCQE cross-section,  $\sigma_k^{DATA}$ , can then be written as

$$\sigma_k^{data} = F_N \cdot a_k \cdot \sigma_k^{MC} \quad (9.7)$$

Where  $\sigma_k^{MC}$  is the cross-section used by the NEUT MC.

This is the proposed approach for the combined analysis, including the SciBar-MRD matched and SciBar-contained samples. To extract the cross-section from the SciBar-contained sample only one neutrino energy bin, from 0-2 GeV, is used, due to the low statistics of the sample<sup>1</sup>. Therefore equation 9.6 simplifies to

$$N_{i,s}^{exp} = \left[ a_{ccqe} N_{i,s}^{ccqe} + a_{bkgd} N_{i,s}^{bkgd} \right] \quad (9.8)$$

And equation 9.7 becomes

$$\sigma_{ccqe}^{data} = a_{ccqe} \cdot \sigma_{ccqe}^{MC} \quad (9.9)$$

Figure 9.1 shows the  $p_\mu$  vs.  $\theta_\mu$  distributions for the data and MC samples.  $p_\mu$  is binned in twenty bins from 0 to 2 GeV/c,  $\theta_\mu$  is binned in ten bins from 0 to 180 degrees.

---

<sup>1</sup>The SciBar-MRD matched sample is approximately ten times larger than the SciBar-contained sample

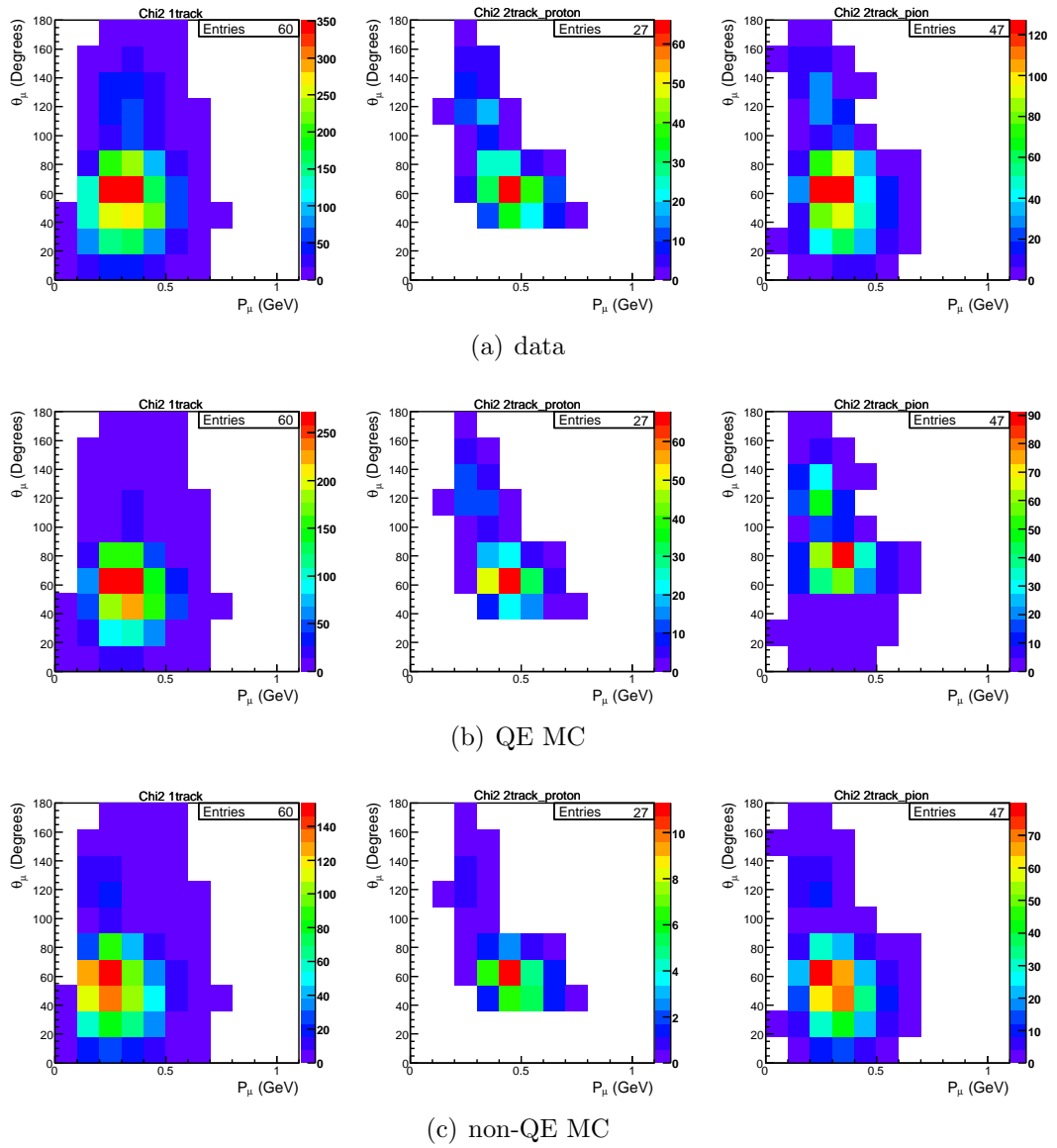


**Figure 9.1:**  $P_\mu$  vs.  $\theta_\mu$  distributions for (a) data events, (b) CCQE events in MC, (c) background events in MC. The  $\mu$ ,  $\mu + p$ , and  $\mu + \pi$  distributions are shown from left to right, respectively.

---

## 9.2 Systematic Uncertainties

The systematics can be separated into four categories

- Detector response
- Neutrino beam
- Nuclear effects
- Neutrino interaction models

Variations within the uncertainties of these systematics are made, with the resultant change to the CCQE cross-section taken as the systematic uncertainty to the measurement.

### 9.2.1 Detector Effects

The uncertainties in the MA-PMT cross-talk, the single photo-electron resolution of the MA-PMT, the scintillator quenching effect, the hit-threshold for track reconstruction and the TDC deadtime are considered.

#### MA-PMT Cross-Talk

The cross-talk was measured to be  $3.15 \pm 0.4\%$  [46]. A new MC event set with variations to the cross-talk was prepared to evaluate the systematic error.

#### Single Photo-Electron Resolution

The single photo-electron resolution of the MA-PMT is set to 50% in the MC simulation. The absolute error was determined, using cosmic ray data, to be 20% [46]. A new MC event set with variations to the single photo-electron resolution was prepared to evaluate the systematic error.

---

### Scintillator Quenching

Birk's constant for the SciBar scintillator bars was measured to be 0.0208 cm/MeV with an error of 0.0023 cm/MeV [52]. A new MC event set with variations to Birk's constant was prepared to evaluate the systematic error.

### Hit Threshold

The hit threshold for track reconstruction is set to 2 photo-electrons. The channel-to-channel variation in the photo-electron to energy conversion factor for SciBar channels was measured, using cosmic ray data, to be approximately 20% [46]. A new MC event set with variations to the hit threshold was prepared to evaluate the systematic error.

### TDC Deadtime

The TDC deadtime is set to 55 ns in the MC simulation, with the error estimated to be  $\pm 20$  ns. A new MC event set with variations to the TDC deadtime was prepared to evaluate the systematic error.

## 9.2.2 Neutrino Beam

The uncertainties in the meson production cross-sections in proton-beryllium interactions, hadronic interactions in the target and horn, the horn magnetic field model, and the delivery of the primary proton beam to the target and beam optics, as described in section 5.1, are considered.

The change in the neutrino beam spectrum due to these uncertainties is evaluated by drawing random parameter vectors and weighting each event by a factor corresponding to the parent meson yield with the given momentum and angle. To evaluate the error, the extracted cross-section is calculated for each beam systematic parameter vector.

### 9.2.3 Nuclear Effects

Uncertainties in the pion absorption and pion inelastic scattering cross-sections in the momentum range of pions produced from  $\Delta$  decays is approximately 30% [87].

### 9.2.4 Neutrino Interaction Models

The axial vector mass for resonant pion production,  $M_A^{1\pi}$ , is set to 1.21 GeV/ $c^2$  in the NEUT simulation. The error on this value is estimated to be approximately  $\pm 0.1$  GeV/ $c^2$  for the SciBooNE neutrino energy range, based on recent measurements [69, 70]. Past experimental results are systematically lower than the recent measurements [88], therefore only a decrease in  $M_A^{1\pi}$  to 1.11 GeV/ $c^2$  is considered. The current method to extract the systematic error involves a reweighting scheme using the NUANCE MC. Figure 9.2 shows the  $E_\nu^{rec}$  distributions for the SciBar-contained sample for the NUANCE and NEUT MC. Currently this systematic is not considered due to the disagreement in these distributions.

## 9.3 Results

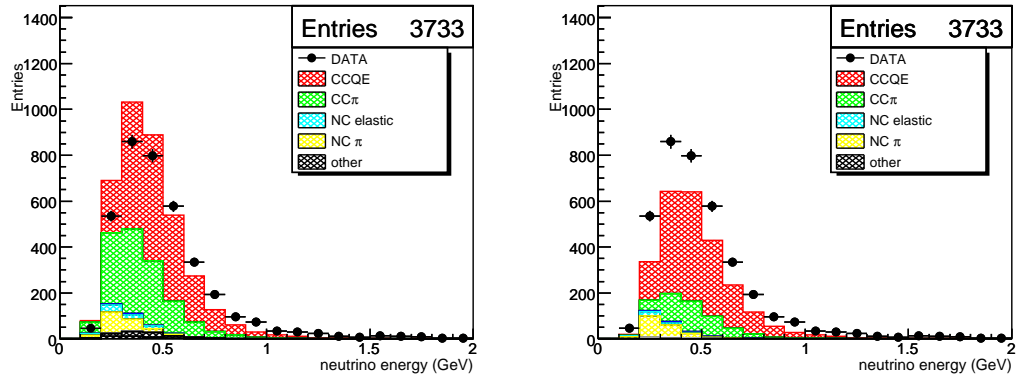
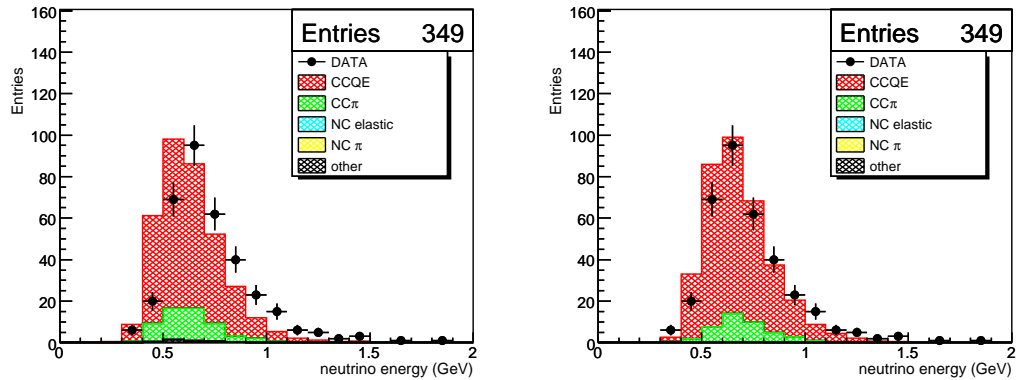
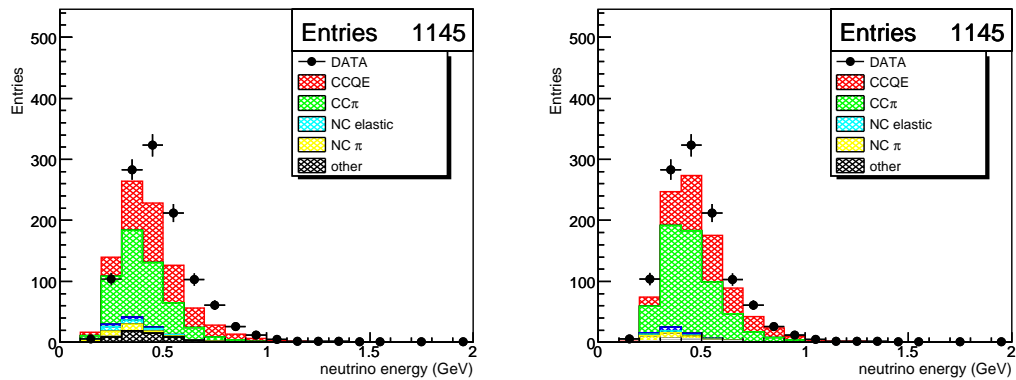
The MINUIT package [89] in ROOT is used to minimise equation 9.5. The fit is carried out including and excluding the backwards track sample. The results of the fit can be seen in table 9.1.

Fit Parameters	Excl. Backward Tracks		Incl. Backward Tracks	
	Value	Error	Value	Error
$a_{ccqe}$	0.944	0.033	1.061	0.031
$a_{bkgd}$	1.035	0.038	1.011	0.036

**Table 9.1:** The best fit values and errors for the fit parameters  $a_{ccqe}$  and  $a_{bkgd}$ .

By applying equation 9.9 the CCQE cross-section, excluding backwards tracks, is calculated to be

$$\sigma_{\nu_\mu}^{ccqe} = 9.39 \pm 0.31(\text{stat}) \times 10^{-39} \text{cm}^2/\text{neutron}, \quad (9.10)$$

(a) Combined  $\mu$  &  $\mu + e$  samples(b)  $\mu + p$  sample(c)  $\mu + \pi$  sample

**Figure 9.2:**  $E_{\nu}^{rec}$  distributions in for NEUT (left) and NUANCE (right) MC for (a)  $\mu$  sample, (b)  $\mu + p$  sample, (c)  $\mu + \pi$  sample.

and including backwards tracks as

$$\sigma_{\nu\mu}^{\text{ccqe}} = 1.055 \pm 0.030(\text{stat}) \times 10^{-38} \text{cm}^2/\text{neutron}. \quad (9.11)$$

The default NEUT MC cross-section is  $9.944 \times 10^{-39} \text{cm}^2/\text{neutron}$ . The statistical error on the cross-section is calculated from the errors on the fitting parameters, summarised in table 9.1, calculated as

$$\delta\sigma = \sqrt{\sum_i \left( \frac{\partial\sigma}{\partial a_i} \cdot \delta a_i \right)^2 + 2 \sum_{i<j} \rho_{ij} \left( \frac{\partial\sigma}{\partial a_i} \right) \left( \frac{\partial\sigma}{\partial a_j} \right) \delta a_i \delta a_j}, \quad (9.12)$$

where  $\sigma$  is the extracted cross-section,  $\delta a_i$  is the fit parameter error, and  $\rho_{ij}$  is the correlation coefficient matrix, which is obtained from fitting to be

	$a_{\text{ccqe}}$	$a_{\text{bkgd}}$	
$a_{\text{ccqe}}$	1.00	-0.65	(9.13)
$a_{\text{bkgd}}$	-0.65	1.00	

excluding backwards tracks, and

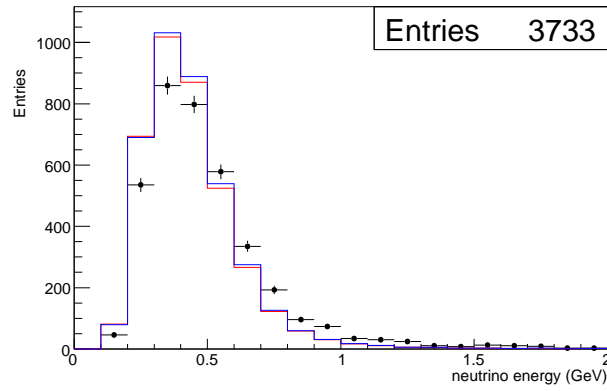
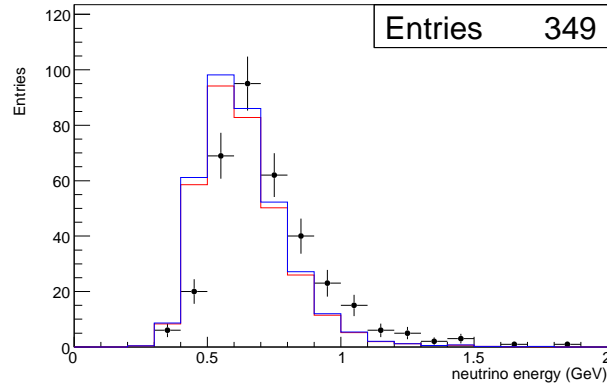
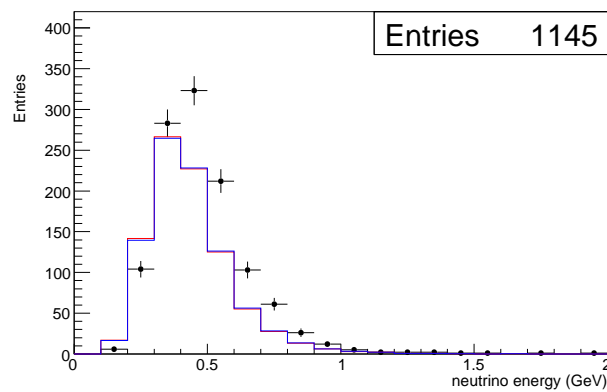
	$a_{\text{ccqe}}$	$a_{\text{bkgd}}$	
$a_{\text{ccqe}}$	1.00	-0.63	(9.14)
$a_{\text{bkgd}}$	-0.63	1.00	

including backwards tracks. Equation 9.9 is only a function of one fitting parameter,  $a_{\text{ccqe}}$ , so equation 9.12 simplifies to

$$\delta\sigma = \sqrt{\left( \frac{\partial\sigma}{\partial a_{\text{ccqe}}} \cdot \delta a_{\text{ccqe}} \right)^2} = \sigma_{\text{ccqe}}^{\text{MC}} \delta a_{\text{ccqe}}. \quad (9.15)$$

The  $\chi_{\text{excl}}^2$  before the fit was 315.4/76 d.o.f.; after the fit the  $\chi_{\text{excl}}^2$  is 312.4/76 d.o.f. The  $\chi_{\text{incl}}^2$  before the fit was 743.7/133 d.o.f.; after the fit the  $\chi_{\text{incl}}^2$  is 735.6/133 d.o.f. There is little reduction in the  $\chi^2$  for either fit; the large  $\chi^2$  suggests introducing only two fitting parameters is insufficient to reproduce the data. Figure 9.3 shows the reconstructed neutrino energy distributions for the three samples with the MC before (blue) and after (red) the fit. Clearly the fit fails to match the MC to the data.

The reason the fit fails is that the three sample distributions have very different data/MC ratios. The fit is unable to reconcile these different data/MC distributions using only two global fit parameters.

(a)  $\mu$  &  $\mu + e$  samples(b)  $\mu + p$  sample(c)  $\mu + \pi$  sample

**Figure 9.3:**  $E_{\nu}^{rec}$  distributions excluding backwards tracks before (blue) and after (red) the fit for (a)  $\mu$  sample, (b)  $\mu + p$  sample and (c)  $\mu + \pi$  sample.

### 9.3.1 Introducing Additional Fit Parameters

To improve the fit for the SciBar-contained sample requires the introduction of additional fit parameters, local to each sample. Equation 9.8 can be rewritten in terms of each individual sample as:

$$N_{i,\mu}^{exp} = \left[ a_{ccqe} N_{i,\mu}^{ccqe} + a_{bkgd} N_{i,\mu}^{bkgd} \right] \quad (9.16)$$

$$N_{i,\mu p}^{exp} = R_{2trk/1trk} \cdot R_{p/\pi} \cdot \left[ a_{ccqe} N_{i,\mu p}^{ccqe} + a_{bkgd} N_{i,\mu p}^{bkgd} \right] \quad (9.17)$$

$$N_{i,\mu\pi}^{exp} = R_{2trk/1trk} \cdot \left[ a_{ccqe} N_{i,\mu\pi}^{ccqe} + a_{bkgd} N_{i,\mu\pi}^{bkgd} \right] \quad (9.18)$$

where  $N_{i,\mu}^{exp}$ ,  $N_{i,\mu p}^{exp}$  and  $N_{i,\mu\pi}^{exp}$  are the expected number of events for the  $\mu$ ,  $\mu + p$ , and  $\mu + \pi$  samples. Two new fit parameters,  $R_{2trk/1trk}$  and  $R_{p/\pi}$ , describe the possible migrations of events between samples due to systematic uncertainties. The results of the fit can be seen in table 9.2. The correlation coefficient matrix excluding

Fit Parameters	Excl. Backward Tracks		Incl. Backward Tracks	
	Value	Error	Value	Error
$a_{ccqe}$	1.009	0.033	1.089	0.032
$a_{bkgd}$	0.795	0.039	0.853	0.037
$R_{p/\pi}$	0.636	0.048	0.683	0.046
$R_{2trk/1trk}$	1.543	0.063	1.366	0.049

**Table 9.2:** The best fit values and errors for the fit parameters:  $a_{ccqe}$ ,  $a_{bkgd}$ ,  $R_{p/\pi}$  and  $R_{2trk/1trk}$ .

backwards tracks is

	$a_{ccqe}$	$a_{bkgd}$	$R_{p/\pi}$	$R_{2trk/1trk}$
$a_{ccqe}$	1.000	-0.593	-0.387	0.146
$a_{bkgd}$	-0.593	1.000	0.428	-0.574
$R_{p/\pi}$	-0.387	0.428	1.000	-0.533
$R_{2trk/1trk}$	0.146	-0.574	-0.533	1.000

(9.19)

and including backwards tracks

	$a_{ccqe}$	$a_{bkgd}$	$R_{p/\pi}$	$R_{2trk/1trk}$
$a_{ccqe}$	1.000	-0.558	-0.334	0.002
$a_{bkgd}$	-0.558	1.000	0.371	-0.462
$R_{p/\pi}$	-0.334	0.371	1.000	-0.492
$R_{2trk/1trk}$	0.002	-0.462	-0.492	1.000

(9.20)

The  $\chi_{excl}^2$  before the fit was 315.4/76 d.o.f.; after the fit the  $\chi_{excl}^2$  is 203.8/76 d.o.f. The  $\chi_{incl}^2$  before the fit was 743.7/133 d.o.f.; after the fit the  $\chi_{incl}^2$  is 659.8/133

d.o.f. Some reduction in the  $\chi^2$  is achieved through the addition of extra fit parameters; however the  $\chi^2$  is still large, suggesting that more fit parameters are needed to describe the data.  $\chi_{incl}^2$  is approximately twice as large as  $\chi_{excl}^2$  after the fit. This is expected given the excess of backwards tracks in the one-track sample. Figure 9.4 show the reconstructed neutrino energy and momentum transfer for the three samples. The fitted MC better describes the distributions for all three samples in figure 9.4 than in figure 9.3. There are significant shape disagreements between data and MC for all three samples. Because all the fit parameters are applied to the entire distribution these disagreements can't be reconciled without introducing fit parameters that are a function of the true neutrino energy,  $E_\nu^{true}$ . Separating out the dominant background (CC- $\pi$  events) from the background  $P_\mu$  vs.  $\theta_\mu$  distributions could also improve the fit.

The neutrino beam and detector systematics have been calculated. To calculate the error for each beam systematic one hundred random beam systematic parameter vectors are drawn. The cross-section is calculated for each draw and compared with the fit value to calculate the error,  $\sigma_\pm^{rms}$

$$\sigma_\pm^{rms} = \sqrt{\frac{\sum_i (\sigma_i - \sigma_{cv})^2}{N_\pm}} \quad (9.21)$$

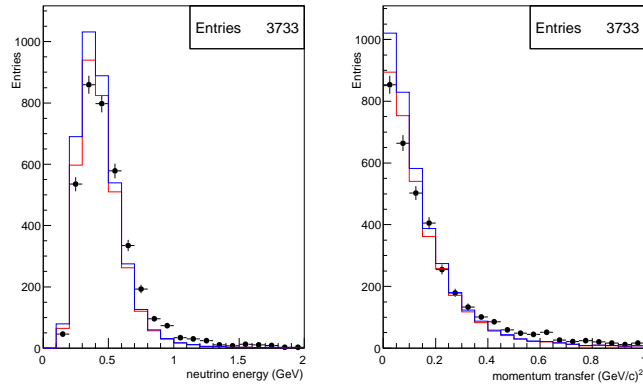
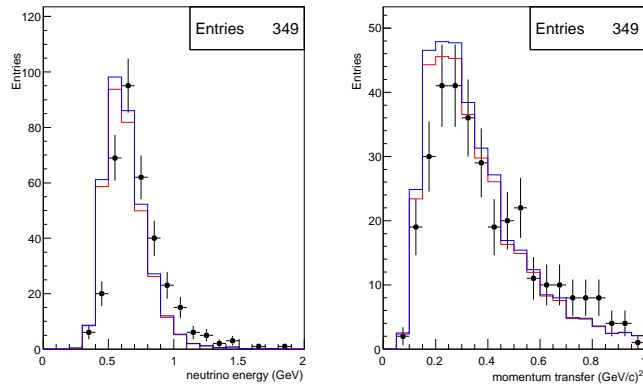
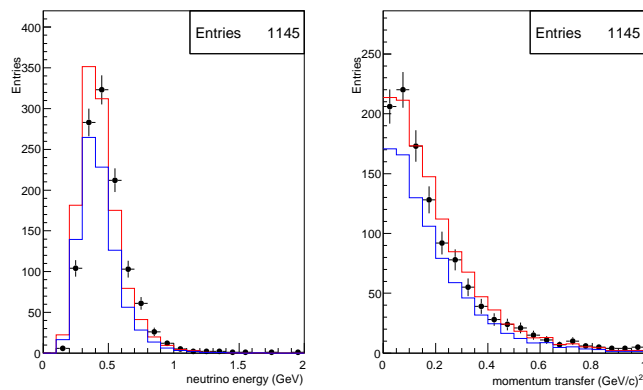
where  $\sigma_i$  is the cross-section for each draw,  $\sigma_{cv}$  is the cross-section extracted from the fit and  $N_\pm$  is the number of draws with cross-sections above, or below,  $\sigma_{cv}$ . A full MC data-set is produced for each detector systematic variation ( $\pm 1\sigma$ ); therefore the detector systematic errors are:

$$\sigma_-^{rms} = \sigma_{cv} - \sigma_- \quad (9.22)$$

$$\sigma_+^{rms} = \sigma_+ - \sigma_{cv} \quad (9.23)$$

Table 9.3 shows the contributions to the the systematic error from the neutrino beam. The dominant source of error comes from the  $\pi^+$  production uncertainty.

Table 9.4 shows the contributions to the error from the detector systematics. The dominant sources of error come from the hit threshold, cross-talk and scintillator quenching uncertainties.

(a)  $\mu$  &  $\mu + e$  samples(b)  $\mu + p$  sample(c)  $\mu + \pi$  sample

**Figure 9.4:**  $E_{\nu}^{rec}$  (left) and  $Q^2$  (right) distributions excluding backwards tracks before (blue) and after (red) the fit for (a)  $\mu$  sample, (b)  $\mu + p$  sample and (c)  $\mu + \pi$  sample.

Beam Error	Excl. Backward Tracks Error (%)		Incl. Backward Tracks Error (%)	
$\pi^+$ production	6.29	-13.35	6.78	-14.41
$\pi^-$ production	0.57	-1.00	0.60	-1.11
$K^+$ production	1.39	-1.29	1.57	-1.46
$K_S^0$ production	0.41	-0.45	0.46	-0.47
Other	5.11	-6.27	5.68	-7.00
Total	8.25	-14.85	9.01	-16.13

**Table 9.3:** The neutrino beam systematic errors.

Detector Error	Excl. Backward Tracks Error (%)		Incl. Backward Tracks Error (%)	
Cross-talk	3.64	-	2.61	-
1 p.e. Resolution	2.64	-0.68	3.25	-1.06
Scint. Quenching	1.28	-0.87	1.34	-1.91
Hit Threshold	3.21	-1.06	3.48	-1.12
TDC Deadtime	-	-0.13	-	-0.17
Total	5.67	-1.54	5.59	-2.46

**Table 9.4:** The detector systematic errors.

The cross-talk and TDC deadtime  $\pm 1\sigma$  variations pull in the same direction for both fits. Table 9.5 shows the fit parameters for the cross-talk systematic. The

Fit Parameter	Excl. Backwards Tracks		Incl. Backwards Tracks	
	+1 $\sigma$	-1 $\sigma$	+1 $\sigma$	-1 $\sigma$
$a_{ccqe}$	1.034	1.036	1.117	1.111
$a_{bkqd}$	0.791	0.768	0.847	0.839
$R_{p/\pi}$	0.680	0.597	0.734	0.653
$R_{2trk/1trk}$	1.502	1.626	1.313	1.407

**Table 9.5:** The cross-talk fit parameter values.

values of  $a_{ccqe}$  and  $a_{bkqd}$  are very similar for the  $\pm 1\sigma$  variations, however compared with the central values in table 9.2 it can be seen that systematic variations affect the migration factors,  $R_{2trk/1trk}$  and  $R_{p/\pi}$ . Increasing the cross-talk decreases the two-track to one-track migration factor,  $R_{2trk/1trk}$ , and increases the proton-pion migration factor. The decrease in  $R_{2trk/1trk}$  decreases the background  $\mu + \pi$  sample and although  $R_{p/\pi}$  increases, the product of  $R_{p/\pi}$  and  $R_{2trk/1trk}$  decreases. Therefore an increase in the cross-talk reduces the two-track to one-track ratio. The cross-talk causes the hit energy in a bar to dissipate into neighbouring channels. Therefore an

increase in the cross-talk will make it harder to distinguish two-track events from one-track events, resulting in a reduction in the number of two-track events. The cross-talk  $\pm 1\sigma$  variations will also affect the MuCL, vertex activity and CCQE cuts it is entirely plausible that these fluctuations in the cuts will result in an increase in CCQE events for both variations.

The CCQE cross-section, excluding backwards tracks, is calculated to be

$$\sigma_{\nu_{\mu}}^{\text{ccqe}} = 1.004 \pm 0.031(\text{stat})_{-0.150}^{+0.101}(\text{sys}) \times 10^{-38} \text{cm}^2/\text{neutron}, \quad (9.24)$$

and including backwards tracks as

$$\sigma_{\nu_{\mu}}^{\text{ccqe}} = 1.083 \pm 0.030(\text{stat})_{-0.177}^{+0.115}(\text{sys}) \times 10^{-38} \text{cm}^2/\text{neutron}. \quad (9.25)$$

The default NEUT MC cross-section is  $9.944 \times 10^{-39} \text{cm}^2/\text{neutron}$ .

Currently no systematic errors due nuclear effects or neutrino interaction models have been considered.

---

# Chapter 10

## Conclusions

### 10.1 Summary

Neutrino-nucleus charged-current quasi-elastic scattering is the signal interaction used by many neutrino oscillation experiments. For muon disappearance studies the signal mode is  $\nu_\mu n \rightarrow \mu p$ . Modern oscillation experiments, such as T2K, produce neutrino beams with peak beam energies of order a few-GeV; it is therefore vitally important to have accurate measurements of the charged-current quasi-elastic cross-section for future neutrino oscillation experiments. Neutrino-nucleus cross-sections in the few-GeV region are not well understood, with the main uncertainties coming from understanding of the neutrino beam flux and the final state interactions within nuclei.

SciBooNE is a sub-GeV neutrino-nucleus cross-section experiment based at Fermilab, Batavia, USA, with the goal to measure neutrino cross-sections with precision of order 5%. SciBooNE took data from June 2007 until August 2008, in total  $0.99 \times 10^{20}$  and  $1.53 \times 10^{20}$  protons on target were collected in neutrino and anti-neutrino mode, respectively.

The goal of this thesis was to extract the absolute CCQE cross-section for the SciBar-contained sample using the SciBooNE neutrino data. To isolate a SciBar-contained CCQE sample a muon tagging method was developed using the TDC timing information in SciBar.

---

An excess of backwards tracks in the one-track sample was observed which is not seen in the two-track samples. Studies of the excess proved inconclusive, but did not rule out physics not modelled in the MC.

The data and MC were described by two-dimensional  $p_\mu$  vs.  $\theta_\mu$  distributions. A Poisson maximum likelihood function is used to extract the absolute cross-section, introducing fit parameters to vary the MC distributions to best fit the data distributions. The SciBar-MRD matched analysis uses fitting parameters applied to CCQE events and background events; this approach proved insufficient to describe the data for the SciBar-contained sample. By including two migration factors,  $R_{2trk/1trk}$  and  $R_{p/\pi}$ , describing the two-track to one-track sample migration and proton-to-pion sample migration, respectively, cross-sections were successfully extracted. The cross-sections were extracted for samples including and excluding backwards tracks and were found to be;

$$\begin{aligned} \text{excl. : } \sigma_{\nu_\mu}^{\text{ccqe}} &= 1.004 \pm 0.031(\text{stat})_{-0.150}^{+0.101}(\text{sys}) \times 10^{-38} \text{cm}^2/\text{neutron}, \\ \text{incl. : } \sigma_{\nu_\mu}^{\text{ccqe}} &= 1.083 \pm 0.030(\text{stat})_{-0.177}^{+0.115}(\text{sys}) \times 10^{-38} \text{cm}^2/\text{neutron}. \end{aligned}$$

Only the neutrino beam and detector systematics are included in this result; these are the dominant sources of systematic error for this measurement. The  $\chi^2$  for the fits were  $\chi_{\text{excl}}^2 = 203.8/76$  d.o.f. and  $\chi_{\text{incl}}^2 = 659.8/133$  d.o.f. The large  $\chi^2$  after fitting shows that there are insufficient fit parameters to describe the data. For the inclusive sample the larger  $\chi^2$  comes from the backwards one-track excess.

Figure 10.1(a) shows the CCQE cross-section measurement made by the MiniBooNE collaboration for neutrino energies up to 2 GeV. The SciBar-contained extracted cross-section in equation 10.1 is in agreement with the MiniBooNE measurement. Figure 10.1(b) shows recent MiniBooNE, LSND and NOMAD CCQE cross-section measurements for neutrino energies up to 100 GeV. A clear disparity between the high energy and low energy cross-sections can be seen when described using the Relativistic Fermi Gas model.

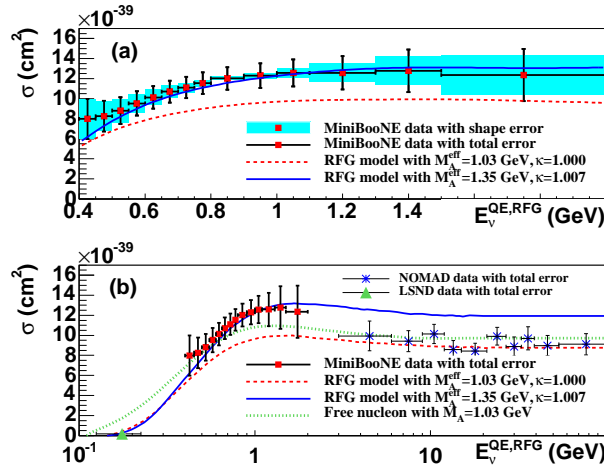


**Figure 10.1:** Flux-unfolded MiniBooNE  $\nu_\mu$  CCQE cross section per neutron as a function of neutrino energy. In (a) shape errors are shown as shaded boxes along with the total errors as bars. In (b) a larger energy range is shown along with results from the LSND [90] and NOMAD [91] experiments. Also shown are predictions from the NUANCE simulation for the Relativistic Fermi Gas model with two different parameter variations and for scattering from free nucleons with the world average  $M_A$  value. The SciBar-contained CCQE cross-section is in agreement with the MiniBooNE measurement. Plot is courtesy of T. Katori [92].

## 10.2 Future Prospects

The major goal for the analysis is to combine the SciBar-contained and SciBar-MRD matched samples and extract an absolute CCQE cross-section. The SciBar-MRD sample has been analysed by J. Alcaraz; figure 10.2 shows the absolute cross-section with flux systematic errors for the SciBar-MRD matched sample [93]. The SciBar-MRD matched CCQE cross-section extraction only uses fit parameters applied to the quasi-elastic and background events. For the SciBar-contained sample this approach was unable to reconcile the data/MC discrepancies seen in the three samples. The fit was improved by including two migration factors,  $R_{2trk/1trk}$  and  $R_{p/\pi}$ , into the fit. To improve the fit further additional migration factors will be introduced to model the momentum scaling, the resonant pion production and backwards one-track events. Additionally the sample will be divided into two neutrino energy bins as the SciBar-contained sample is sensitive to neutrino energies below 600 MeV. Calculating the systematics not included in the study will also be completed. These include pion and proton interactions in the nucleus. Variations in the axial mass,  $M_A^{1\pi}$ , and the Fermi momentum,  $p_F$ , will also be considered. The neutrino beam

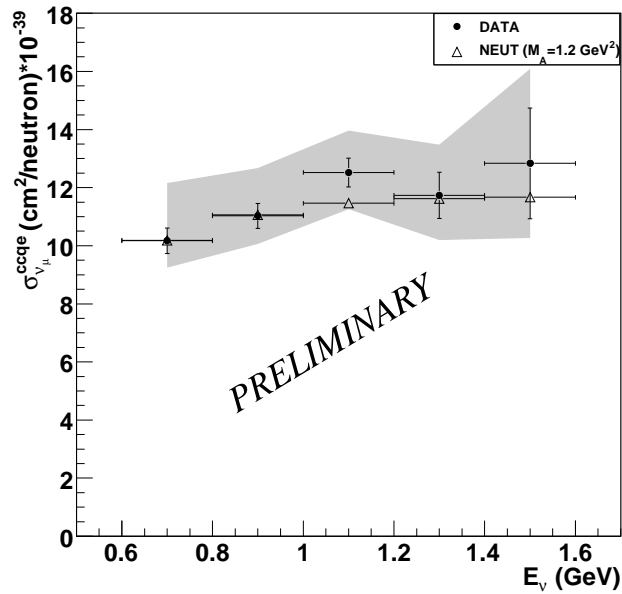


**Figure 10.2:** The extracted cross-section for the SciBar-MRD matched sample. An  $M_A$  value of 1.21 GeV/ $c^2$  is used in the NEUT MC. The flux error is shown by the shaded region.

flux errors have been reduced using a spline fit instead of the Sanford-Wang and Feynman scaling parametrisation. These reduced errors will also be considered.

# Appendix A

## Calculations

### A.1 Neutrino Kinematics

#### A.1.1 Neutrino Energy Calculation

The neutrino energy is reconstructed from the muon kinematics assuming a charged-current quasi-elastic interaction. In a CCQE event,  $\nu n \rightarrow \mu^- p$ , a neutrino strikes a target neutron producing a proton and muon in the final state. A schematic of the interaction is shown in figure A.1.

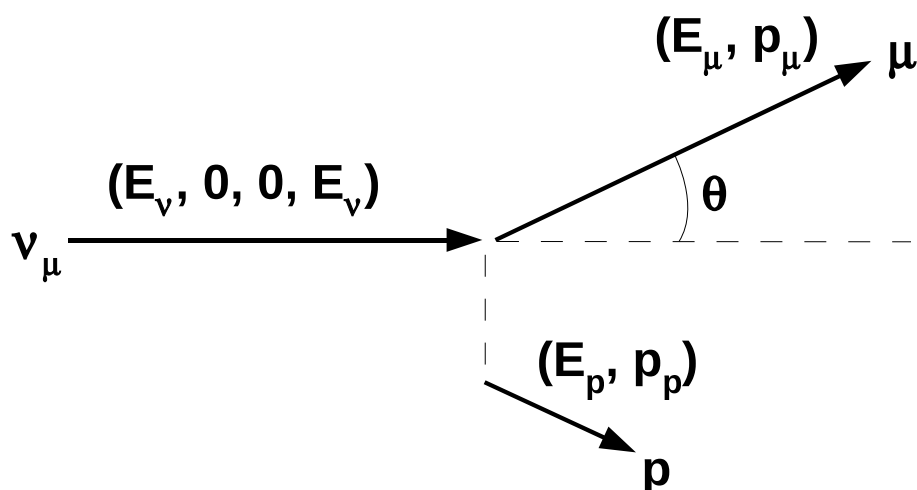


Figure A.1: A CCQE interaction.

SciBooNE sits in an on-axis beam, therefore:

$$\vec{p}_\nu = (0, 0, E_\nu) \quad (\text{A.1})$$

Conservation of momentum implies

$$p_{\mu x} + p_{px} = 0 \quad (\text{A.2})$$

$$p_{\mu y} + p_{py} = 0 \quad (\text{A.3})$$

$$p_{\mu z} + p_{pz} = E_\nu \quad (\text{A.4})$$

Conservation of energy implies

$$E_\mu + E_p = E_\nu + m_n - V \quad (\text{A.5})$$

Therefore applying equation A.5 we can derive the neutrino energy as a function of the muon kinematics as follows:

$$\begin{aligned} E_\nu + m_n - V &= E_p + E_\mu \\ E_\nu - E_\mu + (m_n - V) &= E_p \\ [(E_\nu - E_\mu) + (m_n - V)]^2 &= E_p^2 = m_p^2 + p_p^2 \\ [(E_\nu - E_\mu) + (m_n - V)]^2 &= m_p^2 + p_{px}^2 + p_{py}^2 + p_{pz}^2 \end{aligned} \quad (\text{A.6})$$

Substituting in equations A.2-A.4

$$\begin{aligned} [(E_\nu - E_\mu) + (m_n - V)]^2 &= m_p^2 + p_{\mu x}^2 + p_{\mu y}^2 + (E_\nu - p_{\mu z})^2 \\ [(E_\nu - E_\mu) + (m_n - V)]^2 &= m_p^2 + p_{\mu x}^2 + p_{\mu y}^2 + p_{\mu z}^2 + E_\nu^2 - 2E_\nu p_{\mu z} \end{aligned}$$

Noting that

$$E_\mu^2 - m_\mu^2 = p_\mu^2 = p_{\mu x}^2 + p_{\mu y}^2 + p_{\mu z}^2$$

Gives

$$[(E_\nu - E_\mu) + (m_n - V)]^2 = (m_p^2 - m_\mu^2) + E_\mu^2 + E_\nu^2 - 2E_\nu p_{\mu z}$$

$$E_\nu^2 + E_\mu^2 - 2E_\nu E_\mu + (m_n - V)^2 + 2(E_\nu - E_\mu)(m_n - V) = (m_p^2 - m_\mu^2) + E_\mu^2 + E_\nu^2 - 2E_\nu p_{\mu z}$$

Canceling terms, substituting  $p_{\mu z} = p_\mu \cos \theta_\mu$ , and rearranging gives the result

$$E_\nu = \frac{1}{2} \frac{(m_p^2 - m_\mu^2) - (m_n - V)^2 + 2E_\mu(m_n - V)}{(m_n - V) - E_\mu + p_\mu \cos \theta_\mu} \quad (\text{A.7})$$

### A.1.2 $Q^2$ Calculation

The momentum transfer,  $Q^2$ , is defined as the 4-momentum transfer from the incident neutrino to the proton

$$\begin{aligned}
 Q^2 &= -q^2 = -E_{transfer}^2 + p_{transfer}^2 \\
 &= -(E_p - (m_n - V))^2 + p_p^2 \\
 &= p_p^2 - E_p^2 - (m_n - V)^2 + 2E_p(m_n - V)
 \end{aligned}$$

Substituting in  $p_p^2 - E_p^2 = -m_p^2$  and equation A.5 for  $E_p$  gives

$$\begin{aligned}
 &= -m_p^2 - (m_n - V)^2 + 2(E_\nu - E_\mu + (m_n - V))(m_n - V) \\
 &= -m_p^2 + (m_n - V)^2 + 2E_\nu(m_n - V) - 2E_\mu(m_n - V)
 \end{aligned} \tag{A.8}$$

Rearranging equation A.7 gives

$$\begin{aligned}
 2E_\nu(m_n - V) - 2E_\nu E_\mu + 2E_\nu p_\mu \cos \theta_\mu &= m_p^2 - m_\mu^2 - (m_n - V)^2 \\
 &\quad + 2E_\mu(m_n - V) \\
 -2E_\nu E_\mu + 2E_\nu p_\mu \cos \theta_\mu + m_\mu^2 &= m_p^2 - (m_n - V)^2 + 2E_\mu(m_n - V) \\
 &\quad - 2E_\nu(m_n - V) \\
 2E_\nu E_\mu - 2E_\nu p_\mu \cos \theta_\mu - m_\mu^2 &= -m_p^2 + (m_n - V)^2 - 2E_\mu(m_n - V) \\
 &\quad + 2E_\nu(m_n - V)
 \end{aligned} \tag{A.9}$$

The right-hand side of equation A.9 is the same as the right-hand side of equation A.8, therefore substituting equation A.9 into equation A.8 gives

$$\begin{aligned}
 Q^2 &= 2E_\nu E_\mu - 2E_\nu p_\mu \cos \theta_\mu - m_\mu^2 \\
 Q^2 &= 2E_\nu(E_\mu - p_\mu \cos \theta_\mu) - m_\mu^2
 \end{aligned} \tag{A.10}$$

## A.2 Poisson Maximum Likelihood Derivation

From equation 9.2

$$\begin{aligned}
F_{poisson} &= -2 \ln \lambda \\
&= -2 \ln \frac{f(n_i, \mu_i(\vec{\theta}))}{f(n_i, n_i)} \\
&= -2 \ln \frac{\prod P(n_i, \mu_i(\vec{\theta}))}{\prod P(n_i, n_i)} \\
&= -2 \left[ \ln \prod P(n_i, \mu_i(\vec{\theta})) - \ln \prod P(n_i, n_i) \right] \\
&= -2 \sum \left[ \ln P(n_i, \mu_i(\vec{\theta})) - \ln P(n_i, n_i) \right] \\
&= -2 \sum \left[ \ln \frac{\mu_i^{n_i} e^{-\mu_i}}{n_i!} - \ln \frac{n_i^{n_i} e^{-n_i}}{n_i!} \right] \\
&= -2 \sum [n_i \ln \mu_i - \mu_i - \ln n_i! - n_i \ln n_i + n_i + \ln n_i!] \\
&= 2 \sum [n_i (\ln n_i - \ln \mu_i) + \mu_i - n_i] \\
F_{poisson} &= 2 \sum \left[ \mu_i(\vec{\theta}) - n_i + n_i \ln \frac{n_i}{\mu_i(\vec{\theta})} \right] \tag{A.11}
\end{aligned}$$

---

## References

- [1] SciBooNE Collaboration, A. A. Aguilar-Arevalo *et al.*, “Bringing the SciBar detector to the booster neutrino beam,” [arXiv:hep-ex/0601022](#).
  - [2] K. Nitta *et al.*, “The K2K SciBar detector,” *Nucl. Instrum. Meth.* **A535** (2004) 147–151, [arXiv:hep-ex/0406023](#).
  - [3] J. Chadwick *Verh. d. deutschen phys. Ges.* **16** (1914) 383.
  - [4] N. Bohr *Convegno di Fisica Nucleare (R. Accad. d’Italia, Roma)* (1932) 119.
  - [5] W. Pauli. Letter to L. Meitner and her colleagues (letter open to the participants of the conference in Tübingen), 1930.
  - [6] J. Chadwick *Proc. R. Soc. London (A)* **136** (1932) 692.
  - [7] F. Reines and C. L. Cowan, “Detection of the free neutrino,” *Phys. Rev.* **92** (1953) 830–831.
  - [8] F. Reines and C. L. Cowan, “The neutrino,” *Nature* **178** (1956) 446–449.
  - [9] R. Davis, Jr., “Attempt to detect the antineutrinos from a nuclear reactor by the  $\text{Cl}^{37}(\bar{\nu}, e^{-})\text{A}^{37}$  reaction,” *Phys. Rev.* **97** (1955) 766–769.
  - [10] G. Danby *et al.*, “Observation of High-Energy Neutrino Reactions and the Existence of Two Kinds of Neutrinos,” *Phys. Rev. Lett.* **9** (1962) 36–44.
  - [11] M. L. Perl *et al.*, “Evidence for anomalous lepton production in  $e^{+}e^{-}$  annihilation,” *Phys. Rev. Lett.* **35** (1975) 1489–1492.
-

- 
- [12] **DONUT** Collaboration, K. Kodama *et al.*, “Observation of tau-neutrino interactions,” *Phys. Lett.* **B504** (2001) 218–224, [arXiv:hep-ex/0012035](#).
- [13] **ALEPH** Collaboration, “Precision electroweak measurements on the  $Z$  resonance,” *Phys. Rept.* **427** (2006) 257, [arXiv:hep-ex/0509008](#).
- [14] I. Taylor, “Development of T2K 280 m Near Detector Software for Muon and Photon Reconstruction,” Imperial College Thesis, 2009.
- [15] **Particle Data Group** Collaboration, C. Amsler *et al.*, “Review of particle physics,” *Phys. Lett.* **B667** (2008) 1.
- [16] A. D. Sakharov, “Violation of CP Invariance, c Asymmetry, and Baryon Asymmetry of the Universe,” *Pisma Zh. Eksp. Teor. Fiz.* **5** (1967) 32–35.
- [17] Z. Maki, M. Nakagawa, and S. Sakata, “Remarks on the unified model of elementary particles,” *Prog. Theor. Phys.* **28** (1962) 870.
- [18] B. Pontecorvo, “Neutrino experiments and the question of leptonic-charge conservation,” *Sov. Phys. JETP* **26** (1968) 984–988.
- [19] J. Davis, Raymond, D. S. Harmer, and K. C. Hoffman, “Search for neutrinos from the sun,” *Phys. Rev. Lett.* **20** (1968) 1205–1209.
- [20] **KAMIOKANDE-II** Collaboration, K. S. Hirata *et al.*, “Results from one thousand days of real-time, directional solar-neutrino data,” *Phys. Rev. Lett.* **65** (1990) 1297–1300.
- [21] **SNO** Collaboration, Q. R. Ahmad *et al.*, “Direct evidence for neutrino flavor transformation from neutral-current interactions in the Sudbury Neutrino Observatory,” *Phys. Rev. Lett.* **89** (2002) 011301, [arXiv:nucl-ex/0204008](#).
- [22] **LSND** Collaboration, C. Athanassopoulos *et al.*, “Evidence for anti- $\nu/\mu \rightarrow \bar{\nu}$  anti- $\nu/e$  oscillation from the LSND experiment at the Los Alamos Meson Physics Facility,” *Phys. Rev. Lett.* **77** (1996) 3082–3085, [arXiv:nucl-ex/9605003](#).
-

- 
- [23] **The MiniBooNE** Collaboration, A. A. Aguilar-Arevalo *et al.*, “A Search for electron neutrino appearance at the  $\Delta m^2 \sim 1\text{eV}^2$  scale,” *Phys. Rev. Lett.* **98** (2007) 231801, [arXiv:0704.1500](#) [hep-ex].
- [24] **Super-Kamiokande** Collaboration, Y. Ashie *et al.*, “Evidence for an oscillatory signature in atmospheric neutrino oscillation,” *Phys. Rev. Lett.* **93** (2004) 101801, [arXiv:hep-ex/0404034](#).
- [25] **SNO** Collaboration, B. Aharmim *et al.*, “Electron energy spectra, fluxes, and day-night asymmetries of B-8 solar neutrinos from the 391-day salt phase SNO data set,” *Phys. Rev.* **C72** (2005) 055502, [arXiv:nucl-ex/0502021](#).
- [26] H. Murayama. Available at <http://hitoshi.berkeley.edu/neutrino>, 2008.
- [27] K. Hiraide *Master's thesis, Kyoto University* (2005) .
- [28] S. J. Barish *et al.*, “Study of Neutrino Interactions in Hydrogen and Deuterium. 1. Description of the Experiment and Study of the Reaction Neutrino  $d \rightarrow \mu^- p p(s)$ ,” *Phys. Rev.* **D16** (1977) 3103.
- [29] S. Bonetti *et al.*, “Study of Quasielastic Reactions of Neutrino and anti-neutrino in Gargamelle,” *Nuovo Cim.* **A38** (1977) 260–270.
- [30] **Gargamelle Neutrino Propane** Collaboration, S. Ciampolillo *et al.*, “Total cross-section for neutrino charged current interactions at 3-GeV and 9-GeV,” *Phys. Lett.* **B84** (1979) 281.
- [31] N. Armenise *et al.*, “Charged current elastic anti-neutrino interactions in propane,” *Nucl. Phys.* **B152** (1979) 365–375.
- [32] S. V. Belikov *et al.*, “Quasielastic neutrino and anti-neutrinos scattering: Total cross-sections, axial vector form-factor,” *Z. Phys.* **A320** (1985) 625.
- [33] G. M. Radecky *et al.*, “Study of single pion production by weak charged currents in low-energy neutrino  $d$  interactions,” *Phys. Rev.* **D25** (1982) 1161–1173.
-

- 
- [34] T. Kitagaki *et al.*, “Charged current exclusive pion production in neutrino deuterium interactions,” *Phys. Rev.* **D34** (1986) 2554–2565.
- [35] P. S. Auchincloss *et al.*, “Measurement of the inclusive charged current cross-section for neutrino and anti-neutrino scattering on isoscalar nucleons,” *Z. Phys.* **C48** (1990) 411–432.
- [36] J. P. Berge *et al.*, “Total neutrino and anti-neutrino charged current cross-section measurements in 100-GeV, 160-GeV and 200-GeV narrow band beams,” *Z. Phys.* **C35** (1987) 443.
- [37] V. B. Anikeev *et al.*, “Total cross-section measurements for muon-neutrino, anti- muon-neutrino interactions in 3-GeV - 30-GeV energy range with IHEP-JINR neutrino detector,” *Z. Phys.* **C70** (1996) 39–46.
- [38] A. I. Mukhin *et al.*, “Energy dependence of total cross-sections for neutrino and anti-neutrino interactions at energies below 35-GeV,” *Sov. J. Nucl. Phys.* **30** (1979) 528.
- [39] D. MacFarlane *et al.*, “Nucleon Structure Functions from High-Energy Neutrino Interactions with Iron and QCD Results,” *Z. Phys.* **C26** (1984) 1.
- [40] N. J. Baker *et al.*, “Total cross-sections for muon-neutrino n and muon-neutrino p charged current interactions in the 7-ft bubble chamber,” *Phys. Rev.* **D25** (1982) 617–623.
- [41] **K2K** Collaboration, M. H. Ahn *et al.*, “Measurement of Neutrino Oscillation by the K2K Experiment,” *Phys. Rev.* **D74** (2006) 072003, [arXiv:hep-ex/0606032](https://arxiv.org/abs/hep-ex/0606032).
- [42] C. H. Llewellyn Smith, “Neutrino Reactions at Accelerator Energies,” *Phys. Rept.* **3** (1972) 261.
- [43] **MiniBooNE** Collaboration, A. Bazarko, “MiniBooNE: Status of the booster neutrino experiment,” *Nucl. Phys. Proc. Suppl.* **91** (2001) 210–215, [arXiv:hep-ex/0009056](https://arxiv.org/abs/hep-ex/0009056).
-

- 
- [44] **BooNE** Collaboration, I. Stancu *et al.*, “Technical design report for the 8 gev beam,” tech. rep., FNAL, 2001.  
<http://www-boone.fnal.gov/publicpages/>.
- [45] **BooNE** Collaboration, I. Stancu *et al.*, “Technical design report for the miniboone neutrino beam,” tech. rep., FNAL, 2001.  
<http://www-boone.fnal.gov/publicpages/>.
- [46] K. Hiraide, “A Study of Charged Current Single Charged Pion Productions on Carbon in a Few-GeV Neutrino Beam,” FERMILAB-THESIS-2009-02.
- [47] **The T2K** Collaboration, Y. Itow *et al.*, “The JHF-Kamioka neutrino project,” [arXiv:hep-ex/0106019](https://arxiv.org/abs/hep-ex/0106019).
- [48] **SciBooNE** Collaboration, K. Hiraide, “The SciBar detector at FNAL booster neutrino experiment,” *Nucl. Phys. Proc. Suppl.* **159** (2006) 85–90.
- [49] **SciBooNE** Collaboration, K. Hiraide *et al.*, “Search for Charged Current Coherent Pion Production on Carbon in a Few-GeV Neutrino Beam,” *Phys. Rev.* **D78** (2008) 112004, [arXiv:0811.0369](https://arxiv.org/abs/0811.0369) [hep-ex].
- [50] **BooNE** Collaboration, I. Stancu *et al.*, “The miniboone detector technical design report,” tech. rep., FNAL, 2001.  
<http://www-boone.fnal.gov/publicpages/>.
- [51] J. Birks, *Theory and Practice of Scintillation Counting*. Pergamon Press, 1964.
- [52] M. Hasegawa, “Measurement of neutrino oscillation parameters with neutrino–nucleus interaction studies in the K2K experiment,” *Ph.D. thesis, Kyoto University* (2006) .
- [53] T. Morita *Master’s thesis, Kyoto University* (2004) .
- [54] T. Sasaki *Master’s thesis, Kyoto University* (2004) .
- [55] M. Yoshida *et al.*, “Development of the readout system for the K2K SciBar detector,” *IEEE Trans. Nucl. Sci.* **51** (2004) 3043–3046.
-

- 
- [56] Y. Arai *et al.*, “Development of a new TDC LSI and a VME module,” *IEEE Trans. Nucl. Sci.* **49** (2002) 1164–1169.
- [57] **CHORUS** Collaboration, E. Eskut *et al.*, “The CHORUS experiment to search for  $\nu_\mu \rightarrow \nu_\tau$  oscillation,” *Nucl. Instrum. Meth.* **A401** (1997) 7–44.
- [58] S. Buontempo *et al.*, “Performance of the CHORUS lead-scintillating fiber calorimeter,” *Nucl. Phys. Proc. Suppl.* **54B** (1997) 198–203.
- [59] S. Buontempo *et al.*, “Construction and test of calorimeter modules for the CHORUS experiment,” *Nucl. Instrum. Meth.* **A349** (1994) 70–80.
- [60] J. A. Crittenden *et al.*, “Inclusive Hadronic Production Cross-Sections Measured in Proton - Nucleus Collisions at  $s^{*}(1/2) = 27.4\text{-GeV}$ ,” *Phys. Rev.* **D34** (1986) 2584.
- [61] J. Walding, “The muon range detector at SciBooNE,” *AIP Conf. Proc.* **967** (2007) 289–291.
- [62] **MiniBooNE** Collaboration, A. A. Aguilar-Arevalo *et al.*, “The Neutrino Flux prediction at MiniBooNE,” [arXiv:0806.1449](https://arxiv.org/abs/0806.1449) [[hep-ex](https://arxiv.org/abs/0806.1449)].
- [63] **GEANT4** Collaboration, S. Agostinelli *et al.*, “GEANT4: A simulation toolkit,” *Nucl. Instrum. Meth.* **A506** (2003) 250–303.
- [64] M. G. Catanesi *et al.*, “Measurement of the production cross-section of positive pions in the collision of 8.9 GeV/c protons on beryllium,” *Eur. Phys. J.* **C52** (2007) 29–53, [arXiv:hep-ex/0702024](https://arxiv.org/abs/hep-ex/0702024).
- [65] **E910** Collaboration, I. Chemakin *et al.*, “Pion Production by Protons on a Thin Beryllium Target at 6.4, 12.3, and 17.5 GeV/c Incident Proton Momenta,” *Phys. Rev.* **C77** (2008) 015209, [arXiv:0707.2375](https://arxiv.org/abs/0707.2375) [[nucl-ex](https://arxiv.org/abs/0707.2375)].
- [66] J. R. Sanford and C. L. Wang *BNL Note No. 11299* (1967) .
- [67] Y. Hayato, “NEUT,” *Nucl. Phys. Proc. Suppl.* **112** (2002) 171–176.
- [68] G. Mitsuka, “NEUT,” *AIP Conf. Proc.* **981** (2008) 262–264.
-

- 
- [69] **K2K** Collaboration, R. Gran *et al.*, “Measurement of the quasi-elastic axial vector mass in neutrino oxygen interactions,” *Phys. Rev.* **D74** (2006) 052002, [arXiv:hep-ex/0603034](#).
- [70] **MiniBooNE** Collaboration, A. A. Aguilar-Arevalo *et al.*, “Measurement of muon neutrino quasi-elastic scattering on carbon,” *Phys. Rev. Lett.* **100** (2008) 032301, [arXiv:0706.0926 \[hep-ex\]](#).
- [71] C. H. Albright, C. Quigg, R. E. Shrock, and J. Smith, “Neutrino - Proton Elastic Scattering: Implications for Weak Interaction Models,” *Phys. Rev.* **D14** (1976) 1780.
- [72] L. A. Ahrens *et al.*, “Precise determination of  $\sin^2\theta_w$  from measurements of the differential cross-sections for muon-neutrino  $p \rightarrow$  muon-neutrino  $p$  and anti-muon-neutrino  $p \rightarrow$  anti-muon-neutrino  $p$ ,” *Phys. Rev. Lett.* **56** (1986) 1107.
- [73] R. A. Smith and E. J. Moniz, “Neutrino reactions on nuclear targets,” *Nucl. Phys.* **B43** (1972) 605.
- [74] D. Rein and L. M. Sehgal, “Neutrino Excitation of Baryon Resonances and Single Pion Production,” *Ann. Phys.* **133** (1981) 79.
- [75] D. Rein, “Angular distribution in neutrino induced single pion production processes,” *Z. Phys.* **C35** (1987) 43–64.
- [76] D. Rein and L. M. Sehgal, “Coherent  $\pi^0$  Production in Neutrino Reactions,” *Nucl. Phys.* **B223** (1983) 29.
- [77] D. Rein and L. M. Sehgal, “PCAC and the Deficit of Forward Muons in  $\pi^+$  Production by Neutrinos,” *Phys. Lett.* **B657** (2007) 207–209, [arXiv:hep-ph/0606185](#).
- [78] E. A. Paschos, A. Kartavtsev, and G. J. Gounaris, “Coherent pion production by neutrinos on nuclei,” *Phys. Rev.* **D74** (2006) 054007, [arXiv:hep-ph/0512139](#).
-

- 
- [79] C. W. De Jager, H. De Vries, and C. De Vries, “Nuclear charge and magnetization density distribution parameters from elastic electron scattering,” *Atom. Data Nucl. Data Tabl.* **14** (1974) 479–508.
- [80] L. L. Salcedo, E. Oset, M. J. Vicente-Vacas, and C. Garcia-Recio, “Computer simulation of inclusive pion nuclear reactions,” *Nucl. Phys.* **A484** (1988) 557.
- [81] G. Rowe, M. Salomon, and R. H. Landau, “An energy dependent phase shift analysis of pion - nucleon scattering below 400-MeV,” *Phys. Rev.* **C18** (1978) 584–589.
- [82] H. W. Bertini, “Nonelastic interactions of nucleons and pi mesons with complex nuclei at energies below 3 gev,” *Phys. Rev.* **C6** (1972) 631–659.
- [83] A. Heikkinen, N. Stepanov, and J. P. Wellisch, “Bertini intra-nuclear cascade implementation in Geant4,” [arXiv:nucl-th/0306008](https://arxiv.org/abs/nucl-th/0306008).
- [84] T. Suzuki, D. F. Measday, and J. P. Roalsvig, “Total Nuclear Capture Rates for Negative Muons,” *Phys. Rev.* **C35** (1987) 2212.
- [85] **Particle Data Group** Collaboration, C. Amsler *et al.*, “Review of particle physics,” *Phys. Lett.* **B667** (2008) 1.
- [86] H. Maesaka, “Evidence for muon neutrino oscillation in an accelerator-based experiment,” *Ph.D. thesis, Kyoto University* (2005) .
- [87] D. Ashery *et al.*, “True absorption and scattering of pions on nuclei,” *Phys. Rev.* **C23** (1981) 2173–2185.
- [88] V. Bernard, L. Elouadrhiri, and U. G. Meissner, “Axial structure of the nucleon,” *J. Phys.* **G28** (2002) R1–R35, [arXiv:hep-ph/0107088](https://arxiv.org/abs/hep-ph/0107088).
- [89] F. James and M. Roos, “Minuit: A System for Function Minimization and Analysis of the Parameter Errors and Correlations,” *Comput. Phys. Commun.* **10** (1975) 343–367.
-

- 
- [90] **LSND** Collaboration, L. B. Auerbach *et al.*, “Measurements of charged current reactions of  $\nu/\mu$  on C- 12,” *Phys. Rev.* **C66** (2002) 015501, [arXiv:nucl-ex/0203011](#).
- [91] **NOMAD** Collaboration, V. Lyubushkin *et al.*, “A study of quasi-elastic muon neutrino and antineutrino scattering in the NOMAD experiment,” *Eur. Phys. J.* **C63** (2009) 355–381, [arXiv:0812.4543 \[hep-ex\]](#).
- [92] **MiniBooNE** Collaboration, A. A. Aguilar-Arevalo *et al.*, “First Measurement of the Muon Neutrino Charged Current Quasielastic Double Differential Cross Section,” [arXiv:1002.2680 \[hep-ex\]](#).
- [93] **SciBooNE** Collaboration, J. L. Alcaraz-Aunion and J. Walding, “Measurement of the muon-neutrino charged-current quasi-elastic cross-section in the SciBooNE experiment,” *AIP Conf. Proc.* **1189** (2009) 145–150, [arXiv:0909.5647 \[hep-ex\]](#).
-